

CONTROLLED CRYSTALLIZATION OF INORGANIC
PEROVSKITE SEMICONDUCTOR THIN FILMS VIA
SOLUTION PROCESSING METHODS

TAMIRU KEBEDE SHICHO

JUNE13/2024



JIMMA UNIVERSITY



JIMMA UNIVERSITY, SCHOOL OF GRADUATE STUDIES

CONTROLLED CRYSTALLIZATION OF INORGANIC
PEROVSKITE SEMICONDUCTOR THIN FILMS VIA SOLUTION
PROCESSING METHODS

A PhD DISSERTATION SUBMITTED TO THE SCHOOL OF GRADUATE
STUDIES, JIMMA INSTITUTE OF TECHNOLOGY, JIMMA UNIVERSITY,
ETHIOPIA

FOR THE FULFILMENT OF THE REQUIREMENTS FOR THE DEGREE
OF DOCTOR OF PHILOSOPHY (PhD) IN MATERIAL SCIENCE AND
ENGINEERING

TAMIRU KEBEDE SHICHO

PRINCIPAL ADVISOR: JUNG YONG KIM (PROF. PHD)

CO-ADVISORS : MULUALEM ABEBE (PHD)

DHAKSHNAMOORTHY MANI (PHD)

JUNE 13/2024

JIMMA UNIVERSITY

JIMMA INSTITUTE OF TECHNOLOGY, FACULTY OF MATERIALS
SCIENCE AND ENGINEERING

DECLARATION

I, the undersigned, declare this Ph. D. dissertation, entitled “Controlled Crystallization of inorganic perovskite semiconductor thin films via solution processing methods” is my work and has not been submitted for the award of any academic degree or similar qualification at any other institution or university. Furthermore, I confirm that all the sources I have used or quoted have been appropriately indicated and acknowledged.

Name: Tamiru Kebede Shicho

Signature:



Date: 13/6/2024

SCHOOL OF POSTGRADUATE STUDIES

FACULTY OF MATERIALS SCIENCE AND ENGINEERING

APPROVAL OF DISSERTATION FOR DEFENSE

We hereby certify that we have supervised, read, and evaluated this dissertation titled **“Controlled Crystallization of Inorganic Perovskite Semiconductor Thin Films via Solution Processing Methods”** by **Tamiru Kebede Shicho**. It was prepared under the supervision of **Jung Yong Kim (Ph.D., Professor)**, **Mulualem Abebe (Ph.D., Assoc. Prof.)**, and **Dhakshnamoorthy Mani (Ph.D., Asst. Prof.)**. We recommend submission of the dissertation for the oral defense.

Prof. JUNG YONG KIM (PHD)
Director For Advanced Materials
Science and Engineering Center
of Excellence



13/6/2024

Principal Supervisor

Signature

Date

13/6/2024

Co-Advisor

Signature

Date

13/6/2024

Co-Advisor

Signature

Date

13/6/2024

Department Head

Signature

Date

JIMMA UNIVERSITY

SCHOOL OF POSTGRADUATE STUDIES

COLLEGE OF MATERIALS SCIENCE AND ENGINEERING

BOARD FOR THE DISSERTATION EXAMINERS' APPROVAL SHEET

We, the undersigned, members of the Board of Examiners of the Viva Voce/oral defense by Tamiru Kebede Shicho have read and evaluated his/her dissertation entitled “**Controlled Crystallization of Inorganic Perovskite Semiconductor Thin Films Via Solution Processing Method**” and examined the candidate. This is, therefore, to certify that the doctoral dissertation has been accepted in the fulfillment of the requirement of the doctoral degree in materials science and engineering.

_____	_____	<u>13/6/2024</u>
Chair Person	Signature	Date
Prof. Paulos Tadesse		<u>13/6/2024</u>
External Examiner	Signature	Date
Prof. Menberu Mengesha		<u>13/6/2024</u>
Internal Examiner	Signature	Date
Prof. JUNG YONG KIM (PHD) Director For Advanced Materials Science and Engineering Center of Excellence		<u>13/6/2024</u>
Principal Supervisor	Signature	Date

Dedication

This work is dedicated to my lovely wife and my daughter who are facing different challenges during my PhD study. Their encouragement in my education is unlimited.

Acknowledgment

First and foremost, I am expressing my deepest gratitude, unlimited great thanks, and special affection to **Almighty God**, unless his help in every direction my effort was nothing to finalizing this work. I am expressing my deepest gratitude and special affection to my main advisor (Supervisor) Professor **Jung Yong Kim**, for his constant and unlimited assistance, scientific direction, proper guidance, critical editing of the whole manuscript, friendly encouragement, and great help from the beginning to end of this total dissertation work. I am expressing my deepest gratitude to my co-advisor, Dr Muluaem Abebe for his assistance and direction of computational work one part critical of this dissertation work. I am expressing my deepest gratitude to my co-advisor Dr. Dhakshnamoorthy Mani for his assistance and direction, giving comments on time, and making preconditions to my experimental work in India. I am expressing my deepest gratitude to Professor Sabu Thomas, for his help when conducting experimental work in India. I would like to thank Dr. Aparna Thankappan, for her valuable timely comments. I am grateful to Bonga University and Jimma University for full sponsorship of and guidance of the regular PhD. program in finalizing PhD work. Also, I have great thanks to my lovely wife Tsehayinesh Eshetu & my daughter Absalat Tamiru, and all my family and friends for positive encouragement from the beginning to end of this work.

List of Abbreviation and symbols

MHP	Metal halide perovskite
NCS	Nanocrystals
DIO	1, 8-diiodooctane
ODT	1, 8-octane-dithiol
CN	1-chloronaphthalene
CB	Chlorobenzene
MA	Methyl ammonium
FA	Formamidinium
CASTEP	Cambridge Serial Total Energy Package
PSCs	Perovskite solar cell
OSC	Organic solar cell
PCE	Power conversion efficiency
BHJ	Bulk heterojunction
NFA	non-fullerene-acceptor
EA	Ethyl acetate
DMSO	Dimethyl sulfoxide
DMF	dimethyl formamide
AgBr	Silver bromide
CsPbI ₃	Cesium lead triiodide
CsPbI ₂ Br	Cesium lead iodide bromide
CuInGaSe	Copper indium gallium selenide
HTL	Hole-transport layer
ETL	Electron transport layer

Table of contents

Contents	Pages
Dedication.....	ii
Acknowledgment.....	iii
List of Abbreviation and symbols.....	iv
Table of contents.....	v
List of Tables.....	viii
List of Figure.....	ix
Abstract.....	xi
Chapter One.....	1
1. General Introduction.....	1
1.1 Background of the Study.....	1
1.2 Statement of the Problems.....	4
1.3 Objectives.....	5
1.3.1 General Objectives.....	5
1.3.2 Specific Objectives.....	5
1.4 Research hypothesis/ Research questions.....	5
1.5 Research Gap.....	5
1.6 Significance of the Research.....	6
1.7 Conceptual Framework.....	6
1.8 Delimitation /Scope of the Study.....	6
1.9 Structure of Thesis.....	7
Chapter Two.....	8
2.1 Introduction.....	8
2.2 The Structure of all Inorganic perovskite Thin Films.....	8
2.2.1 The Structure of CsPbI ₃	9
2.2.2 The Structure of CsPbI ₂ Br.....	10
2.2.3 Solvent Additives and their Structures.....	11
2.2.4 Silver Bromide (AgBr) and Its Structure.....	12
2.2.5 Antisolvents and their Chemical Structures.....	13
2.3 Defects in All-inorganic Perovskite.....	13
2.4 Methods of Improving all Inorganic Perovskite Thin Film.....	14
2.4.1 Solvent Additives Method.....	14
2.4.2 Metal Ion Doping Method.....	15

2.4.3 Antisolvents Treatment Methods.....	16
2.4.4 The Flory-Huggins theory of mixed solvents Oligomer.....	18
Chapter Three.....	19
3 Materials and Methods.....	19
3.1 Materials.....	19
3.2 Methods.....	19
3.3 Material Characterizations.....	20
3.3.1 X-ray Diffraction (XRD).....	20
3.3.2 Fourier transform infrared spectroscopy (FT-IR).....	20
3.3.3 Ultraviolet-Visible (Uv-Vis) Spectrometry.....	20
3.3.3 Photoluminescence (PL) spectrophotometer.....	21
3.3.4 Time-resolved photoluminescence.....	22
3.3.5 Scanning Electron Microscopy (SEM).....	22
3.3.6 Transmission electron microscopy (TEM).....	23
3.3.7 Atomic force microscope (AFM).....	23
3.3.8 Computational Methods.....	23
Chapter Four.....	25
Abstract:.....	25
4.1. Introduction.....	26
4.2. Materials and Methods.....	29
4.2.1 Materials.....	29
4.2.2 Methods.....	29
4.2.3 Characterization.....	29
4.2.4. Computational methods.....	30
4.3. Results and Discussion.....	30
4.4. Conclusions.....	44
Abstract:.....	45
5.1. Introduction.....	45
5.2. Materials and Methods.....	48
5.2.1 Materials.....	48
5.2.2 Methods.....	48
5.2.3 Thin Film Characterizations.....	48
5.2.4 Computational Method.....	49
5.3. Results and Discussion.....	49
5.4. Conclusions.....	63
Chapter Six.....	64

6. Facile Improvements of mixed Cesium lead halide (CsPbI_{2.93}Br_{0.07}) Perovskite Thin Film, The Effect of Antisolvent Treatment on Photo physical Property.....	64
Abstract.....	64
6.1 Introduction.....	64
6.1.1 Background of the Study.....	64
6.2. Materials and Methods.....	67
6.2.1 Materials.. ..	67
6.2.2 Methods	67
6.2.3 Characterization.....	67
6.3. Results and Discussion.....	68
6.3.1 The structures and properties of solvent and antisolvents.....	68
6.3.2 Optical Result and Discussion.....	69
6.5 Conclusions.....	76
Chapter Seven.....	77
7. Conclusion and Recommendation.....	77
7.1 Conclusion	77
7.2 Recommendation.....	78
References.....	79
Appendix	111
Annexes.....	114

List of Tables

Table 4. 1 Group contribution to (cohesive energy) for estimating the solubility parameter (δ).....	31
Table 4. 2 Properties of solvents and antisolvent.....	31
Table 4. 3 Flory-Huggins interaction parameter (χ) and molar volume ratio (r) when for the solvent such as DMF or DMSO.	32
Table 5. 1 Solubility parameter, molecular weight, density, and molar volume of solvent, non-solvent, CsPbI ₂ Br. δ' (SI unit) = $\delta \times 2.0455$	57
Table 5. 2 Crystallite size in CsPbI ₂ Br as a function of AgBr doping concentration.....	58
Table 5.3 Analysis of SAED image for CsPbI ₂ Br without annealing at room temperature.....	62
Table 6.1 Polarity index and boiling point of antisolvents.....	69

List of Figure

Figure 1. 1 Schematic representation of Conceptual framework	6
Figure 2. 1 The crystal structure of ABX_3	9
Figure 2. 2 The crystal structure of $CsPbI_3$ perovskite thin film.....	10
Figure 2. 3 The crystal structure of the $CsPbI_2Br$ cubic β -phase unit cell.....	11
Figure 2. 4 The Chemical structure of some Organic additives.....	12
Figure 2. 5 The crystalline structure of (a) $AgBr$ (b) $AgBr$ doped $CsPbI_2Br$ perovskite film	13
Figure 3. 1 The Photograph of FTIR Spectrometry	20
Figure 3. 2 Working principle of Photoluminescence (PL) spectroscopy	22
Figure 3. 3 Principle of Atomic Force Microscopy	23
Figure 4. 1 Chemical structures of organic additives and solvents. (a) Organic additives: DIO, CN, and ODT. (b) Solvents: DMF, DMSO, and CB.....	31
Figure 4. 2 Phase diagrams of binary additive-solvent systems: (a) additive-DMF system, and (b) additive-DMSO system.....	34
Figure 4. 3 Crystal structures of (a) yellow δ -phase $CsPbI_3$ and (b) black γ -phase $CsPbI_3$	35
Figure 4. 4 (a) Yellow δ -phase $CsPbI_3$ with the energy bandgap, $E_g = 2.87$ eV, and (b) black γ -phase $CsPbI_3$ with $E_g = 1.90$ eV. Density of states: (c) Yellow δ -phase $CsPbI_3$ and (d) black γ -phase $CsPbI_3$	36
Figure 4. 5 XRD patterns for (a) self-doped $CsPbI_3$ without organic additive and (b) self-doped $CsPbI_3$ with organic additives such as DIO (brown), CN (violet), and ODT (green).	37
Figure 4. 6 FTIR spectra of self-doped $CsPbI_3$ without and with organic additives, DIO, CN, and ODT	39
Figure 4. 7 SEM images: (a). Self-doped $CsPbI_3$, (b) self-doped $CsPbI_3$ with DIO, (c) self-doped $CsPbI_3$ with CN, and (d) self-doped $CsPbI_3$ with ODT	40
Figure 4. 8 (a) Selected area diffraction pattern and (b) high-resolution TEM image of the self-doped $CsPbI_3$ sample.	41
Figure 4. 9 UV-Vis absorption spectra of (a) yellow δ -phase $CsPbI_3$ and (b) black γ -phase $CsPbI_3$ and its derivative (e.g., Cs_4PbI_6 or low dimensional structure). Tauc plot for determining bandgap of (c) yellow δ -phase $CsPbI_3$ and (d) black γ -phase $CsPbI_3$ and its derivatives.....	42
Figure 4. 10 Self-doped $CsPbI_3$ without/with organic additive: (a) PL emission spectra and (b) Time-resolved PL decay spectra.....	44
Figure 5.1 (a) Unit cell and supercell of $CsPbI_2Br$ with lattice parameters, $a = b = 6.395$ Å and $C = 5.988$ Å. (b) B-site doping by silver for $CsPbI_2Br$ supercell with size of $2 \times 2 \times 1$	51
Figure 5. 2 Band structure of pseudo-cubic α -phase $Cs_4Pb_{4-x}Ag_xI_8Br_4$ when (a) $x = 0$, (b) $x = 1$, (c) $x = 2$, (d) $x = 3$, and (d) $x = 4$. (f) Bandgap as a function of Ag contents (%)......	52
Figure 5.3 (a) UV-Vis spectra of $CsPbI_2Br$ as a function of $AgBr$ concentration. (b) Bandgap as a function of $AgBr$ doping concentration (%).	54
Figure 5.4 Optical bandgap determination for $CsPbI_2Br$ as a function of $AgBr$ concentration by Tauc plot.	54
Figure 5.5 PL lifetime of $CsPbI_2Br$ thin film as a function of $AgBr$ concentration.	55
Figure 5.6 (a) FT-IR spectra of $CsPbI_2Br$ with or without $AgBr$ when processed with dimethyl sulfoxide (DMSO) and chlorobenzene (CB). (b) Chemical structures of DMSO and CB. (c) Solvent engineering process.....	57
Figure 5.7 $CsPbI_2Br$ as a function of $AgBr$ doping: (a) XRD patterns and (b) crystallite size.	58
Figure 5. 8 Structural stability test by XRD: (a) $CsPbI_2Br$ without $AgBr$ and (b) $CsPbI_2Br$ with 1% $AgBr$	59

Figure 5.9 SEM images: (a) CsPbI ₂ Br without AgBr, (b) CsPbI ₂ Br with 1% AgBr (c) CsPbI ₂ Br with 2% AgBr, and (d) CsPbI ₂ Br with 3% AgBr.....	61
Figure 5.10 HR-TEM image of CsPbI ₂ Br with different scale bars: (a) 2 nm, (b) 5 nm, and (c) 10 nm. (d) Selected area electron diffraction (SAED) pattern of CsPbI ₂ Br displaying the phase impurity at room temperature.....	62
Figure 6. 1 The chemical structure of antisolvents and solvents.....	69
Figure 6. 2 The optical spectra of (a) Uv-Vis absorbance (b) the Tauc plot of energy band gap and (c) the PL intensity of CsPbI ₃ perovskite film and 5%CsBr mixed with CsPbI ₃ perovskite film.....	70
Figure 6. 3 Optical spectra of Pure & mixed halide perovskite with annealing temperature and dripping time.....	71
Figure 6. 4 The FTIR spectra of CsPbI ₃ perovskite film and different concentrations of CsBr mixed with controlled perovskite film.....	72
Figure 6. 5 XRD patterns of controlled and 5% CsBr mixed with controlled perovskite film treated with mixed antisolvents.....	73
Figure 6. 6 The field emission scanning electron microscope (FE SEM) images of (a) CsPbI ₃ perovskite film treated with TEA, (b) 5% CsBr mixed CsPbI ₃ perovskite film treated with TEA.....	74
Figure 6. 7 TEM images of CsPbI ₃ perovskite film (a) without CsBr mixed (b) With CsBr mixed.....	75
Figure 6. 8 AFM image of (a) control film treated with TEA, (b) 5% CsBr treated with TEA.....	76

Abstract

Inorganic perovskite semiconductors have recently gotten great concern in the field of photovoltaics due to their excellent optoelectronic properties such as a superb carrier dispersion span, resilient light absorption intensity, low defect density, solution processability, narrow spectral bandwidth, and halide composition, tuneable direct band gap, covering the visible spectral range, high photoluminescence quantum yields, and high absorption coefficient. Perovskite materials are susceptible to degradation from heat, light, and moisture. On the other hand perovskite material can undergo a phase change from the optically active α -phase to the yellow δ -phase. A decrease in the performance and lifetime of the photovoltaic nanotechnology accompanies this phase transition. The above challenges can lead to disturbance in the applications of photovoltaic devices. To overcome the problems, we set objectives such as self-doping of all inorganic Cesium lead iodide film and treated with additives, doping mixed lead halide perovskite with silver bromide, and treating mixed halide perovskite film by mixed antisolvent. Experimentally, we used a solution processing method through a one-step spin-coating process, and theoretically, we examined the microelectronic crystal structure of the unit cell of the material by density function theory (DFT) and theoretical calculation based on Flory-Huggins theory. The optical properties of the film were characterized by ultraviolet-visible spectroscopy, photoluminescence spectroscopy, and time-correlated single-photon counting (TCSPC) spectroscopy. X-ray diffraction (XRD) characterized the films' crystal structure. An infrared spectrum of emission and absorption of the perovskite film demonstrated by Fourier transform infrared (FTIR) spectrometry. The microstructure of the film's morphology was studied by Field emission scanning electron microscopy, transmission electron microscopy (TEM), and atomic force microscopy. Primarily, we demonstrate self-doped cesium lead iodide film and treated by organic additives. In this case, the complete homogeneity of additive-solvent showing higher critical solution temperature (HCST) behavior is for both different additive-solvent mixtures chloronaphthalene: Dimethyl formamide > Octanediithiol: Dimethyl formamide > Diethyl octane: Dimethyl formamide. When 1, 8-diiodooctane (DIO), and 1-chloronaphthalene (CN) were used as stabilizers the manifestation process was improved prerequisite to the formation of an appropriate bandgap improvement to 1.76eV (doping with CN), 1.78eV (doping with DIO) from 1.83 eV (undoped). Secondly, we doped cesium lead mixed halide (CsPbI₂Br) perovskite film by varying silver bromide (AgBr) concentration to study the consequence of AgBr on the perovskite film. The bandgap tenability as a function of the silver doping level

using density function theory through half substitution of lead by silver, and experimentally with varying AgBr concentrations in the precursor solution of perovskite film. Resultantly, the film maximized the bandgap value from ~1.87 eV to ~1.96 eV. The lifetime of the film was increased from 0.99ns (undoped) to 1.187 ns (doped with AgBr). Generally from investigation, we found that doping with an appropriate concentration of silver bromide (AgBr) resulted in improved phase purity, increased crystallinity, uniform film coverage, and changed surface morphology. Finally, we investigate the effect of mixed polar antisolvents (mixed toluene with ethyl acetate) on cesium lead mixed halide perovskite film. Resultantly, the observed phase similarity indicated that the mixed CsBr in the perovskite film had no negative effect, miscible in precursor solution uniformly, and increased the crystalline size. From the overall demonstration, the perovskite film has improved optically, structurally, and morphologically. Finally, the self-doping method with additive manufacturing, doping silver bromide with all inorganic perovskite, and treating mixed halide perovskite with mixed antisolvent ought to help to produce a black γ -phase perovskite for light absorbing material in ambient conditions.

Chapter One

1. General Introduction

1.1 Background of the Study

Renewable energy sources are becoming increasingly important as the world faces a growing energy crisis. Due to the reduction of fossil energies, the use of renewable energy sources, their conversion mechanism from one to another, and conservation by more efficient power harvesting devices are the current global issues. It plays a vital role as one of the solutions to climate change, carbon dioxide reduction, and minimizing the greenhouse effect [1]. The modern world's social prosperity and economic growth depend on sustainable energy conversion and the development of novel storage [2]. Among conversion mechanisms of renewable energies, converting solar energy into electric energy is the most hopeful renewable energy resource and source, solving energy challenges and reducing carbon dioxide emissions [3].

Solar energy was crucial during the green industrial revolution due to its non-pollution, renewability, high energy consumption the most promising renewable energy sources, and new technology for photovoltaic nanotechnology [4]. Different types of absorption layers of photovoltaic materials (solar cells) are produced and modified from period to period to develop more effective and efficient devices; such as the amorphous silicon absorption layer of amorphous silicon solar cells [5], Cadmium Telluride absorption layer of Cadmium Telluride solar cells [6], Monocrystalline silicon absorption layer of solar cells [7], copper indium gallium selenide absorption layer of photovoltaics [8], thin-film solar cells [9], Polycrystalline silicon solar cell [10], dye-sensitized absorption layer solar cell [11], gallium arsenide absorption layer solar cells [12], biohybrid solar cell [13], CuInGaSe solar cells [14], multi-junction solar cells [15], quantum dot absorption layer of solar cell [16], plasmonic solar cells [14], Concentrator photovoltaic [17], and perovskite photovoltaics [18].

Perovskite photovoltaic is prepared from a material called perovskite, which is a crystalline compound with the formula ABX_3 , where the A and B are typically single-ion smaller radius cations and double-ion bigger radius cations respectively, and the X-site is typically halide anions. Perovskite solar cells have several advantages over traditional silicon solar cells such as low cost, fast response time, and high efficiency. Perovskite materials are relatively

inexpensive to produce, which makes perovskite solar cells are more cost-effective option than silicon-based photovoltaics. Perovskite photovoltaic can achieve an efficiency of over 21%, which is comparable to the high effectiveness of silicon solar cells. Conversely, solar cells formed by perovskite active layer can fast respond to light, which makes them a good option for applications of rapid power generation. Despite of numbers its disadvantages such as instability, toxicity, and negative impact on the environment, perovskite solar cells are promising new technology that could potentially revolutionize the solar energy industry. Perovskite light absorbing materials can be categorized under Organic, organic-inorganic, and all inorganic perovskite active layers by their A-site arrangements of cations such that; if A site is MA^+ or FA^+ , Rb/ Cs doped on MA^+ or FA^+ and Cs/Rb alone respectively.

Due to the volatile meioty of organic components, methyl ammonium, and formamidinium showing thermal and chemical instability, searching for solutions was conducted by different scholars for all inorganic perovskite semiconductor materials. Among the findings, the A site cations were replaced by inorganic cations to overcome the problems. Halide-based all-inorganic perovskite is a promising material for potential applications in optoelectronics devices. They are more efficient, cheaper to manufacture, and can be produced on a large-scale fabrication compared to organic perovskite photovoltaics [19]. Halide-based all-inorganic perovskite is used to perovskite materials as a light-absorbing semiconductor. Improving the light-absorbing layer was one of the mechanisms of device improvements, such as HTL improvement, and ETL improvements.

Semiconducting halide-based inorganic photovoltaics are energy harvesting devices, and have got great consideration outstanding to their wonderful photosensitive properties; such as superb carrier dispersion span [20], resilient light absorption [21], low defect density, ability to solution processing [22], narrow spectral bandwidth [23], halide composition, tenable direct band gap [24] covering the whole visible spectral range [25], high photoluminescence significant harvests [26] and high absorption coefficient [27]. All inorganic halide-based photovoltaics are a promising material for potential uses in optoelectronics applications. The PCE of all inorganic perovskite is exceeded by greater than 21% [28], nevertheless, the cubic phase creation with high temperature and phase shift to orthorhombic phase in ambient conditions, all inorganic Cesium lead halides perovskite lags from the organic and organic-inorganic optoelectronics application. The two big challenges faced by halide inorganic perovskite (HIP) materials are instability and phase behaviour. Halide inorganic perovskite (HIP) materials are susceptible to degradation from heat, light, and moisture. This can lead to

a decrease in the performance of the photovoltaic materials over time. Another challenge of perovskite light-absorbing material is its phase behaviour. Perovskite material can undergo a phase transition from the black α -phase to the yellow δ -phase (active phase to inactive phase). A decrease in the stability of the photovoltaic devices accompanies this phase transition.

Improving halide inorganic perovskite photovoltaic nanotechnology is the main concern of the energy conservation community in this era. Several strategies can be used to improve the stability and control the phase change from optically inactive to optically active black phase of perovskite photovoltaics, such as adding stabilizing agents to the perovskite films, doping perovskite using metal ion and metal halides, and dripping antisolvents into the precursor of perovskite, to protect the perovskite from the environment, and operating the optoelectronic device at lower temperatures [29-32].

Additive engineering is used to: tune the tolerance factor, modulate crystallization, and tailor the surface energy of perovskite resulting in improved perovskite film stability in PSCs [29]. It can afford fine switches of the dynamic film morphology and be investigated for their role in the improvement of the optoelectronics performance of perovskite solar cells [30]. Solvent additives are used to boost the perovskite film crystallinity, morphology, and stability of the film for PSCs [31]. Also, they are the best way for crystallization promotion, surface passivation, and ion regeneration [32].

Metal-ion doping method in perovskite semiconductor optoelectronics is partially replacing lead (Pb) or lead halide with other metal ions or metal-halides such as silver iodide (AgI), silver bromide (AgBr), etc. Doping perovskite with silver bromide is used to improve the morphology and performance of both organic and inorganic perovskite materials [33]. The antisolvent dripping and mixed halide composition methods are also the greatest fruitful techniques to develop the morphology of Cesium lead halide active-layer films to enhance the performance and modify the surface of the films for photovoltaic applications [34].

In this dissertation, we set an objective to make an excellent nanocrystalline light-absorbing layer thin film for good competence optoelectronic applications, using solvent additives in the precursor of self-doped CsPbI₃ perovskite film, doping all inorganic perovskite film with silver bromide, and treating all inorganic CsPbI₃ perovskite film by antisolvents. We prepared perovskite film via a solution processing method followed by one-step spin-coating methods and characterized the films optically, crystalline, and morphologically. Resultantly we found

the film had improved optical properties, increased crystalline size, and smooth surface morphology than untreated perovskite films.

1.2 Statement of the Problems

The approaches that change behaviour, save energy, and then develop new technology that can harvest energy in different applications are imperative. The growth of new materials for energy conversion, storing, and power conversion efficiency applications is significant to meet the energy challenges of the modern era. However, there are several challenges observed while using perovskite photovoltaics. Some of the challenges of optoelectronics devices, their instability is the most. Perovskite materials are susceptible to degradation from environmental conditions. This can lead to a decrease in the efficiency of the solar over time. Another challenge of perovskite light-absorbing material is its phase behaviour. Perovskite material can undergo a phase transition from the optically active phase (α -phase) to the optically inactive (δ -phase). A decrease in the performance of the photovoltaics accompanies this phase transition. The phase transition is triggered by environmental conditions such as temperature, UV- light, and humidity [35]. Several strategies may be used to recover the stability and control the phase of CsPbX₃ film from degradation and phase changes. To secure a black perovskite phase by avoiding a yellow one. The phase changes of the perovskite films occur, on the one hand from the annealing temperature of CsPbI₃ film. At high annealing temperature, the film was black perovskite phase while it changed to the yellow phase when the annealing temperature was cooling to room temperature. Different strategies to stabilize the perovskite film at lower annealing temperatures may overcome the problems. On the other hand, the performance of the CsPbI₃ perovskite film decreased due to environmental factors such as humidity, moisture, and UV light. To overcome such disturbance, from many strategies solvent stabilizers, and additive materials might be hindering the degradation of perovskite materials. CsPbI₃Br has morphological defects from fast crystallization and unmatched energetic alignment with the charge transport layer. To overcome such challenges developing strategies such as metal ion doping, treating with solvents/antisolvents and other strategies might be the way of problem-solving methods. CsPbI₃ film has also degraded since it is affected by temperature influence and environmental factors. Composition engineering of halides together with antisolvent treatment methods proposed among different problems followed by the layer serving as good optoelectronics applications.

1.3 Objectives

1.3.1 General Objectives

The general objective of this dissertation was to make a high-quality nanocrystalline perovskite thin film for good efficiency light-absorbing applications.

1.3.2 Specific Objectives

The specific objectives of this thesis were (1) to study the phase behaviour of self-doped cesium lead iodide thin film by combining an extra cesium iodide (CsI) into the precursor solution of perovskite, followed by examining the effect of solvent stabilizer on the photosensitive, physical, and surface morphological properties, (2) to develop the superficial morphology of CsPbI₂Br thin film with AgBr modification for light-absorbing materials and (3) to introduce mix-anti solvents in the mixed-halide all-inorganic perovskite precursor during the film making procedure to producing the light-absorbing active layer phase thin film for photovoltaic devices.

1.4 Research hypothesis/ Research questions

The following research questions were raised while conducting the research.

- ✓ Is the self-doping method applicable in all-inorganic perovskite thin films? What is the outcome of organic additives on modulating the surface morphology of all inorganic cesium lead iodide films for photovoltaic applications?
- ✓ Does doping silver bromide (AgBr) on CsPbI₂Br perovskite thin film improve the film's crystallinity and morphology?
- ✓ What methods are introducing mixed anti-solvents in the mixed-halide all-inorganic perovskite solar cell during film preparation and what development was seen in the active layer of the film?

1.5 Research Gap

The energy harvesting capacity of all inorganic perovskite photovoltaics is increased state-of-the-art from time to time, and the improvement mechanism is highly researched. The phase behaviour and instability of all inorganic (CsPbX₃, X= I, Br or mix of them) perovskite photovoltaics in air condition were not examined more. Due to this, the lifetime of light absorption material fabricated through such conditions is not valued for large-area fabrication. Because of this, the problems of phase behaviour and instability issues were not solved.

1.6 Significance of the Research

This research is expected to search for solar energy harvesting in a photovoltaics-improved way, at less cost and with good performance of cesium lead halide thin film to overcome the instability and phase change of CsPbX_3 ($X=\text{I}, \text{Br}$) thin film, resulting from moisture, oxygen, and humidity. The outputs are predicted primarily to improve light-absorbing active layer for the solar cell industry by providing emerging material-based solar cells for the recipient clients to use excellent stable and optoelectronic property material at low cost and easily processed to harvest more energy, and secondly to share the findings to the scientific community to apply the emerging cost-effective approach through which the constant performance of cesium lead halide solar cells improvement mechanisms.

1.7 Conceptual Framework

The framework of the study of this research work from its sample preparation to the final result and conclusion is settled in the following forms.

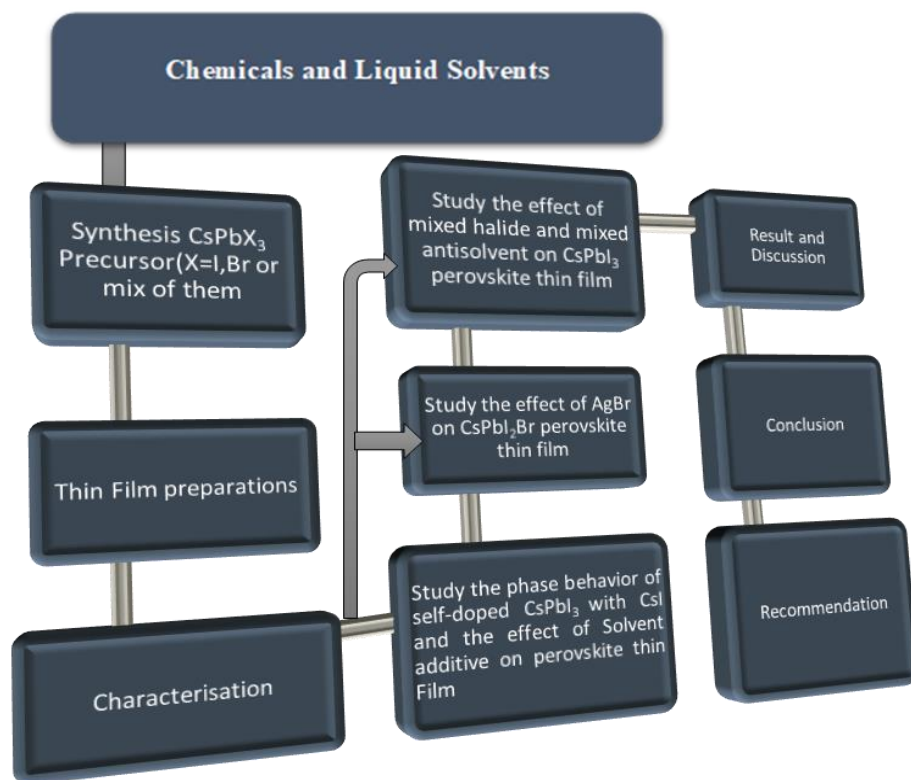


Figure 1. 1 Schematic representation of Conceptual framework

1.8 Delimitation /Scope of the Study

The study of this thesis work included all inorganic Cesium lead halide perovskite semiconductors such as Cesium lead triiodide (CsPbI_3), Cesium lead iodide bromide (CsPbI_2Br), the effect of dopant(AgBr), a solvent additive such as diithiolactane (DIO),

Chloronaphthalene(CN) and Octanediithiol(ODT), and antisolvents on the photosensitive, crystalline, and morphology of Cesium lead halide active layer based film semiconductors.

1.9 Structure of Thesis

The dissertation contains seven chapters. The first chapter explains the introductory part of the perovskite material included in this study. The problem faced in perovskite photovoltaics, the research gap showed in perovskite light absorbing materials, the objective to solve the problems faced in perovskite light absorbing materials, the significance of the study, and conceptual framework are included in this chapter. The second chapter contains some review literature related to the content of this study. Although the structure of all inorganic perovskite material, Solvent additives, antisolvents, dopant materials, all inorganic perovskite material, methods of improving all inorganic perovskite thin films, and the Flory-Huggins theory of mixed solvents Oligomer are discussed under this chapter. The third chapter contains the material and methodology of the study. In this section, the materials needed for the study, the methodology for each perovskite film preparation, the characterization techniques for each perovskite film, and the computational method for theoretical calculation were included. The fourth chapter discussed about results and discussions of the phase behavior and role of organic additives for self-doped CsPbI₃ perovskite semiconductor thin films. In this chapter, the material, method, characterization techniques, and result of self-doped and the effect of additives on perovskite film were explained. The fifth chapter discussed about surface improvement of CsPbI₂Br thin film with AgBr modification for light-absorbing materials, and the sixth chapter state about facile surface improvement of CsPbI₃ perovskite film via halide composition, treated with mixed-antisolvents in ambient air conditions. Finally, the seventh chapter explains the overall conclusion and recommendations.

Chapter Two

2 Review Literature

2.1 Introduction

All inorganic perovskite Caesium lead halides semiconductors have recently developed great devotion in arrears to their outstanding photovoltaic properties, including a superb life span, superior energy harvesting, low imperfection density [36], solution processing, narrow spectral bandwidth, halides composition, acceptable direct band gap, covering the perfect detectible spectral range [37], high photoluminescence quantum yields [38], high absorption coefficient. Different generations of photovoltaic materials improved from period to period by their power conversion efficiency of all inorganic perovskite photovoltaic [39, 40] nevertheless having poor stability [41], low crystallinity [42], and less durability than organic-inorganic perovskite-based solar cells [43], which lags all inorganic perovskite from organic and hybrid perovskites. Thus, improvements must be needed by implementing different methods, to develop the photovoltaic nanotechnology, to boost the enactment and constancy of the film morphology, and photovoltaics. Among the mechanisms to improve photovoltaic enhancements of Caesium lead halides, additive engineering [44], antisolvent engineering [26], boundary engineering, and doping with metal ions [44] are more valuable techniques.

2.2 The Structure of all Inorganic perovskite Thin Films

The period of investigation of privileged perovskite materials has an enduring history that has been intensively studied. Perovskite was 1st discovered by Gustav Rose, and its structure was discovered by Russian investigator L.A. Perovski in 1839 when studying the structure of calcium titanate oxide (CaTiO_3) in metamorphic rock [46]. Then any mineral material owing the structure of the form ABO_3 , where A and B are respectively bigger and smaller ionic radius metal cations, and the remaining is categorized under oxide perovskites [47]. Similarly, metal halides perovskites(MHPs) structure is represented by the general formula of ABX_3 [48], where A is an organic monovalent cation [(MA^+ , FA^+), or non-organic single-ion cation (Cs^+ , Rb^+)], B is a double-ion metal cation (lead (Pb^{2+}), Sn^{2+} (thin), and germanium (Ge^{2+})), and the X is a halogen or mixed halides anion or mix of them [49].

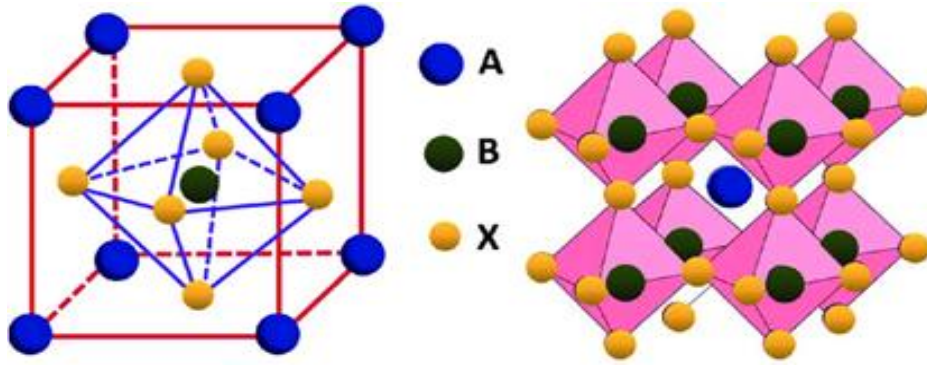


Figure 2.1 The crystal structure of ABX_3

[50]

An expression from Figure 2.1 for the Goldsmiths tolerance factor (t) was derived from the space between two ions is the same as the summation of their radius, that is $t = (R_A + R_X) / \{\sqrt{2}(R_B + R_X)\}$ where r_A , r_B , and r_X are the ionic radius of A, B, and X ions in the range octahedral factor range $0.8 \leq t \leq 1.0$ [51].

2.2.1 The Structure of $CsPbI_3$

$CsPbI_3$ perovskite thin films are a group of all inorganic semiconductor devices that have attractive consideration due to their great usage for the energetic layers of light-absorbing materials and other optoelectronics devices and have a bandgap of 1.73 eV [52]. These materials are composed of a layered structure of Cesium cation (Cs^+) and lead iodide anions (PbI_3^-) with cesium cation occupying the octahedral interstitial sites between the lead iodide layers. The perovskite structure is highly ordered, with long-range cation-anions ordering and short-range cation-cation and anions-anions ordering. This extraordinary degree of level is supposed to be responsible for the excellent optoelectronic properties of $CsPbI_3$ perovskite thin films. The working principles of the inorganic $CsPbI_3$ active layer for photovoltaic application were introduced by Eperon and co-workers in 2016 [53]. $CsPbI_3$ is a Cubic Perovskite structured material that crystallizes in the cubic $Pm\bar{3}m$ space group. The structure consists of a cubic lattice of PbI_6 octahedral (Figure 2.2), with Cs^+ ions inhabiting the body-centered positions and I^- ions covering the face-centered positions [54]. The Cs^+ ions are attached to 12 equal I^- atoms to form CsI_{12} cuboctahedra, which share corners with twelve equivalent CsI_{12} cuboctahedra. The CsI_{12} cuboctahedra faces with 6 equivalents CsI_{12} cuboctahedra and face with eight equivalents PbI_6 octahedral. According to Liu et al illustration of the following structure of the film [45], when it heating (annealing) by high temperature, the phase of the film changes from optical inactive (δ -phase) to optically active phase (α -phase), and when it cooled it changing to β -phase, γ -phase, and finally into δ -phase dramatically.

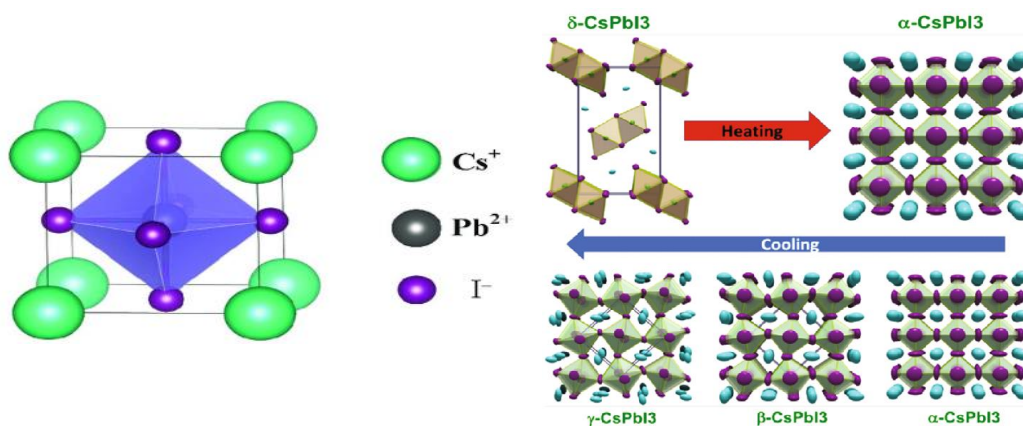


Figure 2.2 The crystal structure of CsPbI₃ perovskite thin film and its phase change [45,54]

CsPbI₃ perovskite thin films can be synthesized by a variety of methods such as spin coating, spray pyrolysis, and vapor-based methods such as molecular beam epitaxial and chemical vapor deposition [45]. The optimal synthesis method can have an important influence on the properties of the resulting thin films, such as the crystallinity, grain size, and defect density. The photovoltaic properties of CsPbI₃ active layer thin films are highly reliant on the film thickness. The energy harvesting coefficient of CsPbI₃ thin films increases with increasing film thickness while the photoluminescence quantum yield decreases. This is because thicker films have more defects, which can act as non-radiative recombination centers [52]. CsPbI₃ perovskite thin films have been shown to have excellent photovoltaic performance, and their perovskite solar cells are inexpensive to manufacture, which makes them a promising candidate for commercialization.

2.2.2 The Structure of CsPbI₂Br

Cesium lead iodide bromide (CsPbI₂Br) is a halide hydride perovskite material that is demonstrated for its photovoltaics applications, and its bandgap is suitable for absorbing sunlight. The crystal structure of CsPbI₂Br is Orthorhombic with the space group Pnma [55] presented in Figure 2.3. The unit cell consists of two CsPbI₂Br layers, with each layer consisting of a square lattice of CsPbI₂Br octahedral. The Cs⁺ cation occupies the octahedral interstices between the CsPbI₂Br two layers. The composition of iodide and bromide in an inorganic thin film for the active layer of light-absorbing material has a bandgap of 1.91eV and greater constancy in the black (cubic) phase is predictable to be a hopeful candidate as light-absorbing material in photovoltaics. CsPbI₂Br can be synthesized by a variety of methods, including thermal evaporation, solution-phase methods, and electrochemical

deposition methods. CsPbI_2Br is a promising material for use in photovoltaics and it is an energy bandgap semiconductor with extraordinary efficiency. Due to its poor quality and low PCE, stabilizing it with more efficient material such as metal halide doping (Example AgI , AgBr), antisolvent dripping, halide composition, and additive engineering play a vital role in overcoming instability problems [56]. Mixing Br into CsPbI_3 to form $\text{CsPbI}_{3-x}\text{Br}_x$ ($0 < x < 0.3$) can successfully grow the tolerance factor and develop phase stability. The energy bandgap of $\text{CsPbI}_{3-x}\text{Br}_x$ film raised with the add-up of Br content. The absorbance of the perovskite increases with increasing the thickness of the films.

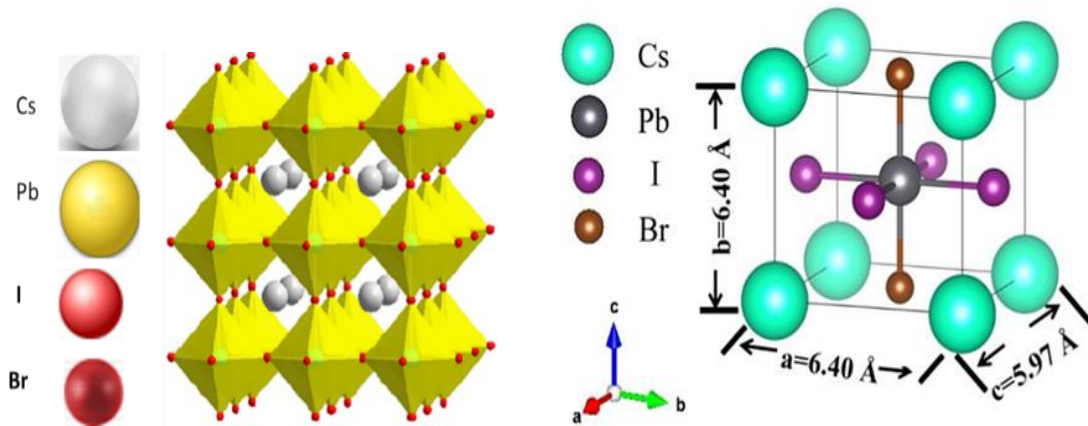


Figure 2.3 The crystal arrangement of the $\text{Cs}_4\text{Pb}_4\text{I}_8\text{Br}_4$ cubic β -phase unit cell [28]

The Figure shows the crystal structure of β -phase $\text{Cs}_4\text{Pb}_4\text{I}_8\text{Br}_4$. The gray, yellow, red, and magenta red balls denote Cs, Pb, I, and Br atoms.

2.2.3 Solvent Additives and their Structures

Organic molecules (additives) such as chloronaphthalene, diiodooctane, Octanediithiol, theophylline, theobromine, and caffeine (xanthines) have been commonly used for proved to be a good engineering solution and used for organic electronics. The strategy has been widely explored in bulk hetero-junction (BHJ), particularly the effect of adding 1, 8- diiodooctane (DIO) to the solvent since it allows morphological control of the active layer of PeSCs.

DIO is a versatile organic molecule and with the addition of it in the precursor solvent, the structure crystallinity increases, ultimately improving carrier mobility in the perovskite films. The insertion of DIO into the precursor of perovskite film can recover their enhancement in several ways[39]. First, DIO can help to inhibit the degradation of energy harvesting material by anion vacancies. It can scavenge these vacancies, preventing them from trapping electrons and holes. Second DIO can help to increase the permanence of the perovskite solar cells. Perovskite solar cells are typically unstable in the air, and they can degrade over time due to

exposure to oxygen and moisture. DIO can help to protect the perovskite materials from these environmental factors, leading to a longer lifetime for the solar cell[25]. Third, DIO can help to improve the effectiveness of the active layer of optoelectronics. DIO can increase the number of electron-hole pairs that are generated by light, and it can help to transport these pairs to the metal anion semiconductors. This makes DIO an important additive for photovoltaics, which are hopeful new technologies for renewable energy.

ODT is a sulfur-containing compound that has been shown to develop the permanence of active layer materials in air and moisture. ODT is thought to act as a sacrificial electron donor, providing to the organic cations to prevent them from being oxidized. ODT is a relatively inexpensive and easy-to-use material and it is effective in a variety of applications. The following chemical structures are some of the structures of solvent additives (Figure 2.4) and some are found in Figure 4.1.

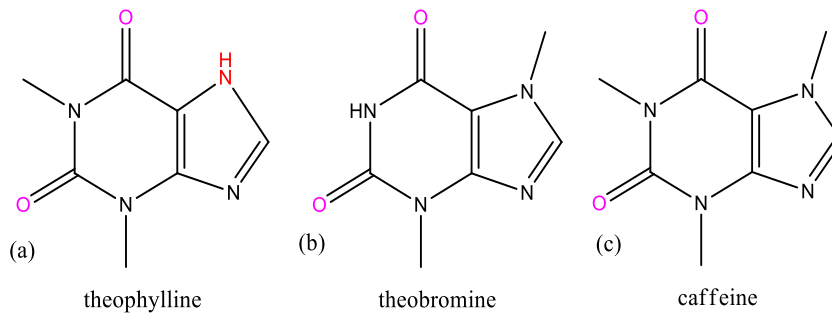


Figure 2.4 The Chemical structure of some Organic additives

2.2.4 Silver Bromide (AgBr) and Its Structure

Silver bromide (AgBr) is a soft, pale-yellow, water-insoluble, halite, rock salt structure and grows in the cubic $Fm\bar{3}m$ space group well known (along with other silver halides) for its unusual sensitivity to light [56]. Ag^{1+} is bonded to six equivalent Br^{1-} atoms to form a corner and edge-sharing $AgBr_6$ octahedral mixture (Figure 2.5a). The corner-sharing octahedral is not tilted. The bond lengths of Ag-Br are 2.89 Å, a melting point of 426 °C, and a boiling point of 1140 °C. AgBr is soluble in concentrated hydrochloric acid and nitric acid. This property has allowed silver halides to become the basis of modern photographic materials and doped by adding an extra molecule to the precursor of the perovskite used to increase charge carriers' conductivity in perovskite materials [57]. Silver bromide is a light-sensitive compound that decomposes when exposed to light and gives silver metal and bromine gas-tempering AgBr crystals between 250° and 400°C and shifting reproducibly to lower tempering Ag values when the AgBr crystals are cooled rapidly after tempering. The AgBr

doping approach minimizes the defect density of Cesium lead halide (CsPbX_3), surface functionalization used for energy harvesting, and improving film quality.

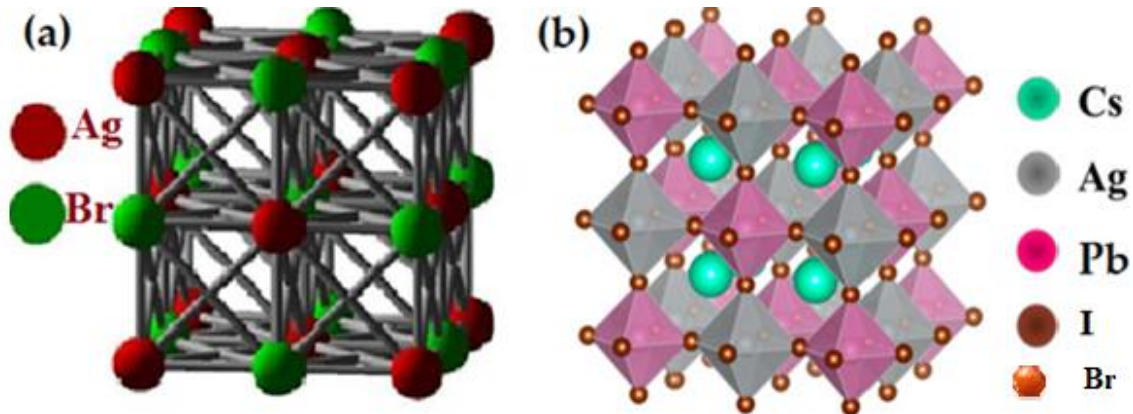


Figure 2.5 The crystalline structure of (a) AgBr (b) AgBr doped CsPbI_2Br perovskite film [58]

2.2.5 Antisolvents and their Chemical Structures

Antisolvent dripping is a common method in perovskite photovoltaics to facilitate the removal of the residual solvent and carefully control the nucleation situation and crystallization growth of the active layer of optoelectronics. Extraordinary performance, crack-free active layers with enhanced grain sizes are reached by using mixtures of different antisolvents such as the mixture of ethyl acetate (EA) with chlorobenzene (CB), and Ethyl Acetate (EA) with toluene (T), Ethyl Acetate (EA) with Isopropyl Alcohol (IPA) in which resulted in improved photovoltaic properties [57-59]. From different analyses ethyl acetate (EA) acted as a solvent that assists in dissolving the excess perovskite precursor due to its polar nature; toluene, IPA, and CB enhanced crystallization by reducing the solubility of the perovskite [60]. A polar antisolvent Toluene (C_7H_8) has an exact mass of 92.06 and a molecular weight of 92.14 and Ethyl acetate ($\text{C}_4\text{H}_8\text{O}_2$) (polar antisolvent) has an exact mass of 88.05 and a molecular weight of 88.11 mixed and produced ethyl propionate with toluene ($\text{C}_{12}\text{H}_{18}\text{O}_2$) having an exact mass of 194.13 and has a molecular weight of 194.27 shown in Figure 6.2. On the other hand, Ethyl acetate ($\text{C}_4\text{H}_8\text{O}_2$) mixed with a nonpolar antisolvent Chlorobenzene ($\text{C}_6\text{H}_5\text{Cl}$) to produce an ethyl acetate compound with chloromethyl (benzene) ($\text{C}_{11}\text{H}_{15}\text{ClO}_2$) is one of the mixed antisolvents. The chemical structure of single and mixed antisolvents is found in Figure 6.2.

2.3 Defects in All-inorganic Perovskite

In real prerequisite crystals, defects are point defects such as vacancies, interstitial, and antistatic, among which vacancies (mainly A-site and X-site) are exclusively detected due to their sufficiently low construction [26]. Antisite defects are the most important defects in

most compound semiconductors. The vacancy defects in perovskite films afford nonradiative recombination centers and increase ion migration. Intrinsic defects in the deep levels of the active layer of the film structure are surficial and physical; lattice defects affect the durable constancy of halide optoelectronics. The defect-tolerant nature of the perovskites is mainly attributed to their electronic band structure in which the highest energy level of the valence band in semiconductor is anti-bonding in nature (with mixed halide $3/4/5p$ and Pb $6s$) and the lowest energy level of conduction band gets stabilized by strong spin-orbit coupling in nature Perovskite solar cells, which having a good photovoltaic properties, has got attention in the past decade. Emerging more high-performance perquisite would keep exciting the PCE of PSCs, which is a great operation for the field [58].

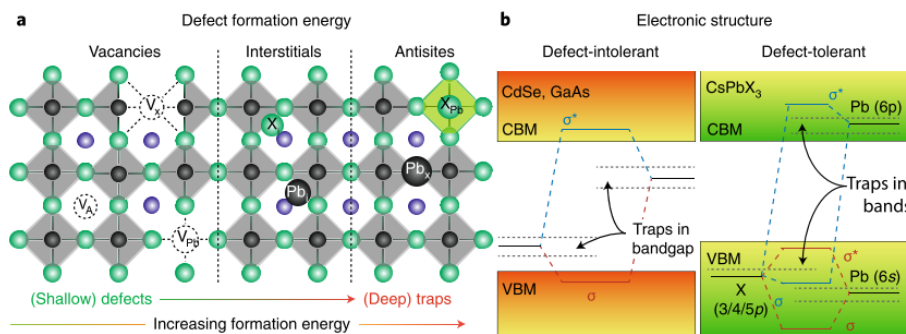


Figure 2. 6 Factors contributing to the defect-tolerant behaviors of lead halide perovskites a. Typical point defects in LHPs, including vacancies, interstitial and anti-site atoms, in the direction of growing establishment energy (or decreasing chance of existence), and their depths in the band gap. b. Schematic representation of electronic band structure of typical defect-in tolerant semiconductors and LHPs.[58]

2.4 Methods of Improving all Inorganic Perovskite Thin Film

The phase of cesium lead halide perovskite film is not constant in ambient conditions and degrades (changes) into an optically inactive phase in ambient conditions. Stabilizers such as organic additives, metal ion doping, and halide composition engineering with antisolvents were proposed to overcome the degradation of the phase of CsPbX_3 perovskite film.

2.4.1 Solvent Additives Method

The solvent additives method is the insertion of a minor element of high tempering point solvent into the precursor of dissolved another host solvent to support imperfection passivation, well-ordered nucleation and manifestation, enhancement of PCE, and optimization of the active layer in terms of phase separation and molecular packing. Also, solvent stabilizers are used to develop the coverage and uniformity of the thin film, stabilize

the intrinsic structure, and withstand the performance limiting factors of all inorganic PeSCs, improving the performances of both polymer and perovskite photovoltaics. Solvent additives are mostly used in organic solar cells by modulating the morphology to boost crystallization via forming an intermediate phase [59]. The strategy of additives for light-absorbing active layer-based solar cells seeks to recover the balance between stability and energy harvesting efficiency. Organic molecules (additives) such as chloronaphthalene, diiodooctane, Octanediithiol, theophylline, theobromine, and caffeine (xanthines) have been commonly used for proved to be a good engineering solution and used for organic electronics. DIO, CN, and ODT have established solvent additives to simplify the aggregation to improve phase separation, used in organic perovskite to tune the film [60], and chelate with lead to the intermediate phase [61]. The strategy has been widely explored in bulk hetero-junction (BHJ), particularly the effect of adding 1, 8-diiodooctane (DIO) to the solvent since it allows morphological control of the active layer of PeSCs. With the addition of DIO in the solvent the structure crystallinity increases, ultimately improving carrier mobility in the perovskite films. DIO ($C_8H_{16}I_2$) additives are used for photon excitation and energy transportation [62], to improve the surface morphology of the perovskite [63], and to develop the miscibility in light-absorbing active layer [64]. Also, DIO enhances the high energy harvesting and constancy of the film, hence developing the perovskite device and increasing the PCE [65]. CN is a common additive in polymer-based organic solar cells [66] used in crystallization control and mobilization of holes. CN is used to resist the film from degradation [67], increase the PCE of BHJ-based photovoltaic devices [68], and extend crystal growth [69]. ODT additives are used to increase the conductivity of photovoltaic [70], control the electrical and surface morphology properties of GSCs, improve phase separation [71], extend the lifetime of the OSCs, improve absorption [72], and maximize the mobility of the hole in the active layer of OSCs [73].

2.4.2 Metal Ion Doping Method

Currently, metal halide perovskite film is doping lead (Pb) with other metals such as and resultantly improves the performance and the phase of the films [74]. Also, by increasing the hardening temperature of the light-absorbing layer, the particle size of the film was enlarged, and the crystallinity was improved [75]. Presently, studies established that by warming reinforced spin-coating technique bright dispensation [76], intermolecular conversation, and boundary passivation [77], the mixture of antisolvents and additive drip techniques of the metal halide optoelectronics can be reserved. The PCEs are increased, but it isn't easy to

manage due to the complex steps to preparation of films and sensitivity to oxygen, moisture, and UV light of precursor of the active layer. The enhancement of all-inorganic metal halide film performance is still a problem due to the difficult preparation method and the sensitivity of perovskite precursor to environmental conditions. Many scholars conduct different investigations to develop the enhancement and consistency of metal halide photovoltaics. Some scholars investigated the reduction of trap density of perovskite film by stabilizing the CsPbI₃ film using guanidinium iodide (GAI) as an additive [788] and got an improvement on the hole-transporter base. Other groups studied the CsPbIBr₂ film using an AgI additive [79]. They found less in number of grain boundaries, and increased particle extent, crystallinity, and photosensitive energy harvesting while reducing transporter recombination and trap density from the film of PSCs [80]. Also in other investigations, investigators improved the Cesium lead halide film by reducing the grain boundary and the surface defect followed by enhancement of charge using Mn⁺ doping on the film [34], Improved the Cesium lead halide film morphology uniformity, crystallinity, and desired phase by high annealing temperature [81]. On the other ways, some groups of investigators improved the all-inorganic perovskite film quality, uniform surface morphology, and low tramp density by passivation of Phenyl ethyl ammonium bromide and CsBr perovskite film [37] while other groups doped AgBr in CsPbBr₃ precursor and from observation results, they reduced defect density and were pinhole-free in the investigated films [16].

2.4.3 Antisolvents Treatment Methods

Antisolvent treatment is a technique that is used to induce fast and condensed nucleation of film that leads to constant and pinhole-free pictures. These techniques are achieved by dripping an antisolvent into the precursor solution, which results in the solubility reduction of the solute in the original solvent and consequently generates supersaturation driving forces [35]. Antisolvent treatment is a process that is used to prompt fast and condensed nucleation of the active layer that leads to constant and voidless films. This process involves the insertion of antisolvents into the precursor solution of perovskite, which results in the reduction of the concentration of the saturated solution in the original solvent and consequently generates a supersaturation driving force. This driving force causes the solute to precipitate out of the solution and form crystals [38]. The type of antisolvent used, the degree of supersaturation, and the crystallization temperatures are all factors that can affect the manifestation procedure and the resulting kinds of stuff of the active layer of optoelectronics. Antisolvent has been shown to develop the effectiveness, stability, and

uniformity of active layers of photovoltaics. The process leads to the establishment of uniform and void-free films, which reduces the amount of light that is lost due to scattering and reflection. Additionally, the process can help to develop the constancy of the solar cell by dropping the amount of defects in the film. The mixed antisolvent method is a variation of the traditional antisolvent method. In this method, two different antisolvents are used in combination. This can help improve the extraction effect and lead to the development of even more similar and pinhole-free films. The crystallization of perovskite by antisolvents reaches supersaturation and solidification by revealing a solution of the product to another solvent in which the product is sparingly soluble. During the crystallization of perovskite crystals, the methods of annealing, the time of annealing, and the annealing temperature strongly affect the crystalline quality and crystal structure in perovskite film. Compared with the single antisolvent treatment, the mixed antisolvent combines the advantages of two antisolvents [82]. The mixed antisolvent treatment method prompts fast and condensed nucleation of perovskite that leads to constant and voidless films. A better extraction effect can be reached by regulating the mixing ratio of different antisolvents. The mixed antisolvent is better than the single antisolvent treatment because it combines the advantages of two solvents. A better extraction effect can be reached by regulating the mixing ratio of different antisolvents. The crystallization of perovskite by antisolvent reaches supersaturation and solidification by revealing a solution of the product to another solvent in which the product is sparingly soluble. During the crystallization of perovskite crystals, the methods of annealing, the time annealing, and the annealing temperature strongly affect the crystalline quality and crystal structure in perovskite film [83]. Antisolvent is added to the solution resulting in the reduction of solubility of the solute in the original solvent and consequently generating a supersaturation driving force. Antisolvents are classified as oxygenated solvents, hydrocarbon solvents, and halogenated solvents. Solvents contain oxygen in their molecular structure known as oxygenated solvents, that contain hydrogen and carbon atoms are hydrocarbon solvents and those that contain halogens are halogenated solvents. Compared with the single solvent, the advantage of mixed solvents is that they combine the advantages of two solvents and a better extraction effect can be achieved by adjusting the collaborating ratio of different stabilizers [84]. Factors affecting the crystallizations are types of solvents, degree of supersaturations, crystallization temperature, and agitation, rate of cooling, impurity and additives, suspended particles, seeding and flow regime, and the surface of crystallizations [85].

2.4.4 The Flory-Huggins theory of mixed solvents Oligomer

The polymer solution of thermodynamics describes the dispensation of liquid solvents that can be preserved as an oligomer. The Flory-Huggins theory is a thermodynamic theory that describes the mixing of two or more solvent components in a situation [86]. The theory is based on the assumption that the molecules of each component are independent of each other and that the interactions between the molecules are only due to the entropic effect of mixing. The theory predicts that the free energy of mixing two components is given by: $\nabla G_m = -nRT\chi\phi_1\phi_2$ Where ∇G_m the free energy of collaborating, n is the number of moles of each component, R is the constant(gas constant), T is the temperature, and χ is the Flory-Huggins interaction parameter [87].

The Flory-Huggins interaction limit measures the strength of the interactions between the molecules of the two components. In this study, the processing solvent stylizers (solvent additives) are treated as oligomers. An oligomer is a polymer that is composed of a small number of monomers. The Flory-Huggins theory can be used to describe the mixing of a polymer with an oligomer. The free energy of any two miscible solvent additives is given by

the Flory-Huggins interaction parameter: $\frac{\nabla G_m}{RT} = \frac{\phi_1}{X_1} \ln \phi_1 + \frac{\phi_2}{X_2} \ln \phi_2 + \chi\phi_1\phi_2$ where ϕ_1 and ϕ_2

are volume fractions of two different solvents, X_1 and X_2 are relative molar volumes of two different solvents. The Flory-Huggins theory predicts that the allowed energy of mixing a solvent additive/antisolvent with an oligomer will be less than the free energy of fraternizing a solvent additive with a monomer [88]. This is because the oligomer has a larger number of monomers than the solvent, and the interactions between the monomer of the oligomer are stronger than the interactions between the monomer of the polymer. The Flory-Huggins philosophy can be used to predict the miscibility of a polymer with an oligomer. The miscibility of a polymer with an oligomer is determined by the values of the Flory-Huggins interaction parameter [89]. If the Flory-Huggins interaction parameter is positive, the additive/antisolvent and the oligomer will be immiscible and if it is negative, the additive/antisolvent and the oligomer will be miscible.

Chapter Three

3 Materials and Methods

3.1 Materials

The materials chemicals and liquid solvents for this research work were lead iodide (PbI_2 , 99.99%, Sigma-Aldrich, Darmstadt, Germany), cesium iodide (CsI , 99.99%, Sigma-Aldrich, Darmstadt, Germany), Cesium bromide (CsBr , 99.9%, Sigma-Aldrich, Darmstadt, Germany), and Silver bromide (AgBr , 99.99%, AR chemicals, Delhi, India), Dimethyl formamide (DMF 99.5%, AR chemicals, Delhi, India), Dimethyl sulfoxide (DMSO, 99%, AR chemicals, Delhi, India), chlorobenzene ($\geq 99.5\%$, AR chemicals, Delhi, India), Toluene ($\geq 99.5\%$, AR chemicals, Delhi, India), and Ethyl acetate (99%, grade LR, model SYMAX). Indium thin oxide slide, square (ITO glass, Sigma-Aldrich, Darmstadt, Germany), Experimental glass, 1, 8-diiodooctane (DIO, 98%, TCI chemicals, Tokyo, Japan), 1-chloronephthaline (CN, 99%, TCI chemicals, Tokyo, Japan), and 1,8-octanediithiol (ODT, 95%, TCI chemicals, Tokyo, Japan) which were used as received without further purification.

3.2 Methods

The precursor solutions and film preparation by the one-step solution processing method. Solutions are homogeneous mixtures that are mixed so thoroughly that neither component can be observed independently of the other. In this work, we dissolved the solute into the solvent by moles per unit volume stoichiometry to colloid a homogenous mixture as liquid solutions. Since the solubility of the solid increases with increasing temperature, we used room temperature (RT) to 343 K to homogenize the liquid solution in the given period. The mixture of different ratios of solute chemicals such as CsI & PbI_2 (2:1, 1:1), CsBr & PbI_2 (1:1), and AgBr , liquefied in the mixture of dimethyl formamide (DMF) and dimethyl sulfoxide (DMSO), and DMSO alone respectively. In the first case 2% ODT, 2% DIO, and 2% CN were added to the precursor of the perovskite film ($2\text{CsI}/\text{PbI}_2$) which dissolved in the mixture of DMF&DMSO. For the second case, CsBr , and PbI_2 dissolved in the DMSO, and AgBr was added as dopants. For the last cases, equal amounts of CsI & PbI_2 dissolved in the mixture of DMF&DMSO (4:1) and 5% CsBr were added concerning CsI and treated with mixed antisolvents such as toluene & ethyl acetate (TEA), Chlorobenzene & ethyl acetate (CBEA) during spin-coating.

3.3 Material Characterizations

The prepared perovskite films were characterized by different techniques to study the thin films' optical, crystallinity, and morphology properties.

3.3.1 X-ray Diffraction (XRD)

The structural properties, particle size, and arrangement of the perovskite film of all inorganic perovskite thin films were examined by X-ray diffraction (XRD) analyzer (model: the Rigaku mini flex-300/600 diffractometer, Tokyo, Japan, and model: the Drawell XRD-700 diffractometer, Tokyo, Japan) with Cu K α (3KW) X-ray radiations ($\lambda = 1.5406 \text{ \AA}$) having a source potential of 40 kV and source current of 15 mA. The ordinary crystallite size of the film was guessed from the Scherer formula where $D = \text{average particle size (nm)}$, $\lambda = \text{wavelength (nm)}$ of the light source, $\beta = \text{is the full width at half maximum (FWHM) of the corresponding diffraction peak}$, $\theta = \text{the diffraction angle (degree)}$, and $K (0.94)$ is the Scherer constant [90].

3.3.2 Fourier transform infrared spectroscopy (FT-IR)

FTIR is an analytical method used to identify inorganic materials and is extremely sensitive to increases in humidity as the optical windows are made of hygroscopic materials. The attenuated total reflection (ATR) was engaged to record the FT-IR spectra of the perovskite thin films in the range $4000\text{--}400 \text{ cm}^{-1}$ with a resolution of 4 cm^{-1} were performed with a PerkinElmer spectrum two FTIR spectrometers in transmittance mode.

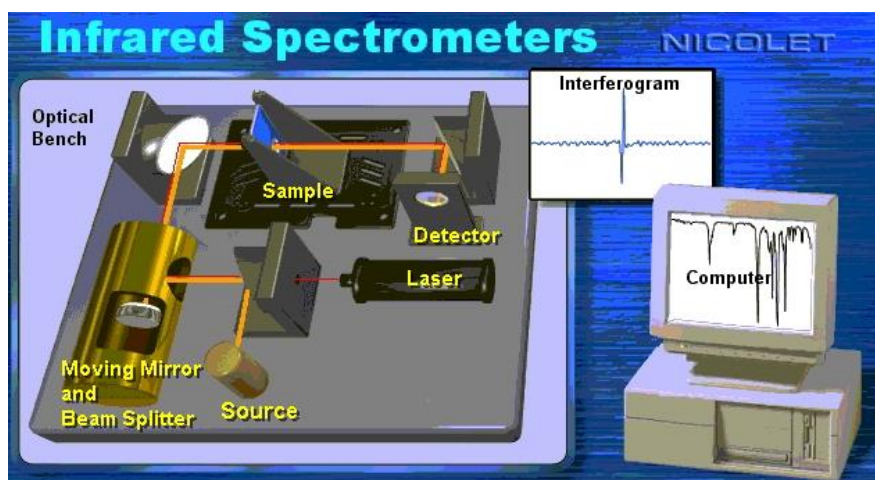


Figure 3.1 The Photograph of FTIR spectrometry

3.3.3 Ultraviolet-Visible (Uv-Vis) Spectrometry

The absorption intensity of the all-inorganic perovskite film was investigated by ultraviolet-visible (UV-Vis) spectroscope (PerkinElmer Lambda 25, Kyoto, Japan). Absorption edges result from electronic transitions between a valence band's top and the conduction band's

bottom. Any photon with energy greater than this band gap will be absorbed. The intensity of an absorption band is related to the concentration of the absorbing ion in the crystal. Thus, optical spectra can determine the amount of particular ions in crystals. The light passing through a crystal at a given wavelength can be measured in units of percent transmission, $\%T=100 \times I/I_0$ where I_0 is the intensity of light incident upon the crystal, and I is the intensity passing through the crystal. Most instruments present the intensity in absorbance units: Absorbance, $A = -\log_{10}(I/I_0)$ [91].

The band gap energy of a semiconductor describes the energy needed to excite an electron from the valence band to the conduction band. An accurate determination of the band gap energy is crucial in predicting photophysical and photochemical properties of semiconductors. In particular, this parameter is often referred to when photocatalytic properties of semiconductors are discussed. In 1966 Tauc proposed a method of estimating the band gap energy of amorphous semiconductors using optical absorption spectra. His proposal was further developed by Davis and Mott. The Tauc method is based on the assumption that the energy-dependent absorption coefficient α can be expressed by the following equation $(\alpha h\nu)^{1/m}$ vs. $B(h\nu - E_g)$ where h is the Planck constant, ν is the photon's frequency, E_g is the band gap energy, and B is a constant. The m factor depends on the nature of the electron transition and is equal to 1/2 or 2 for the direct and indirect transition band gaps, respectively [88,90]

The reservation of energy bandgap is based on the plot of energy versus energy density $(\alpha h\nu)^2$ vs. $h\nu$, where α is the absorption coefficient, h is Planck's constant, and ν is the frequency of the incident photon.

3.3.3 Photoluminescence (PL) spectrophotometer

Photoluminescence (PL) spectrophotometer is a contactless, non-destructive technique of probing the electronic arrangement of materials, governed by stimulated emission of radiation. When light is irradiated onto a sample, photo-excitation starts, absorbing light and imparting excess light energy into a material, the sample can disintegrate this extra energy in two ways: by energy emission or through luminescence. The light can be analyzed spectrally, spatially, and temporally. In photoluminescence spectroscopy, we measured the light energy of emitted light as a function of wavelength by using optical spectroscopy. PL occurs when a specimen emits light after absorbing a photon from an external light source such as a UV energy source. When the high-energy source is used to stimulate, all available electrons are

excited into their energy state [92]. On the other hand, Photoluminescence (PL) spectroscopy is a form of light emission spectroscopy in which the light emission comes from a process called photo-excitation. As the light is directed onto a sample, the electrons inside the sample move into excited states. When electrons jump from the excited states to their equilibrium states, the energy can be released as light. PL spectra were noted by measuring the light energy of the emitted radiation as a function of varying excited wavelengths. This work investigated the thin films photoluminescence (PL) emission spectra by a steady-state/transient fluorescence spectrophotometer (SHIMADZU RF-6000, Kyoto, Japan) with an excitation wavelength of 420 nm and 520 nm.

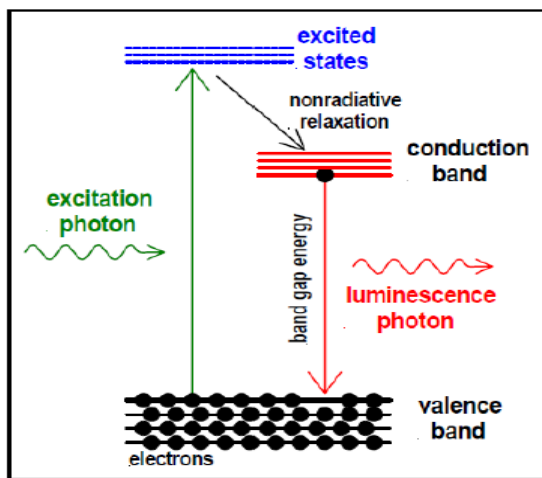


Figure 3.2 Working principle of Photoluminescence (PL) spectroscopy

3.3.4 Time-resolved photoluminescence

Time-resolved photoluminescence is used to detect the radioactive decay of the samples in which excited electrons have a radioactive decay channel. Theoretically, the time-resolved PL intensity measurement rate equations are given by $N(t) = N_0 \exp(-t/\tau)$, where $\tau = 1/(A + A')$, N is the excitation condition, and A and A' are the radiative & nonradiative recombination respectively. The decay curve of the emitted photon should be exponential [93]. This research recorded the PL lifetime using time-correlated single-photon counting (TCSPC) (model: Fluor log 3 TCSPC, Horiba, and Houston, TX).

3.3.5 Scanning Electron Microscopy (SEM)

SEM is a versatile and powerful microscopic technique for material characterization and uses electrons for imaging, morphological studies, and nano & microstructure studies. The microstructure image of all-inorganic perovskite thin films was characterized by Field

emission scanning electron microscopy (FE-SEM, Carl ZEISS microscopy, MAIA3 XMH (model 2016) 119-0025, Germany).

3.3.6 Transmission electron microscopy (TEM)

TEM is a microscopic method that utilizes a particle beam of electrons to visualize specimens and produce extremely magnified images up to several million times. Its working method is to record a topography image of the specimen from the electron beam after it has passed through a thin film of the specimen under study [47]. In this case, electrons are transmitted through a sample, forming an image. Transmission electron microscopy relies on interactions between photon energy and a thin transparent sample of the concentration material for its characterization. The nanostructure image of the perovskite thin film was obtained using a high-resolution transmission electron microscopy (HR-TEM, Model: JEOL, JEM-2100, Peabody, MA, USA) with an operating voltage of 200 kV.

3.3.7 Atomic force microscope (AFM)

The atomic force microscope is a scanning probe microscope in which a topographical image of the sample surface can be achieved based on the interactions between a tip and a sample surface as shown in Figure 3.3. The idea of AFM for the first time demonstrated in 1986 by Binnig and Quate while demonstrating a small probe tip at the end of a cantilever [91].

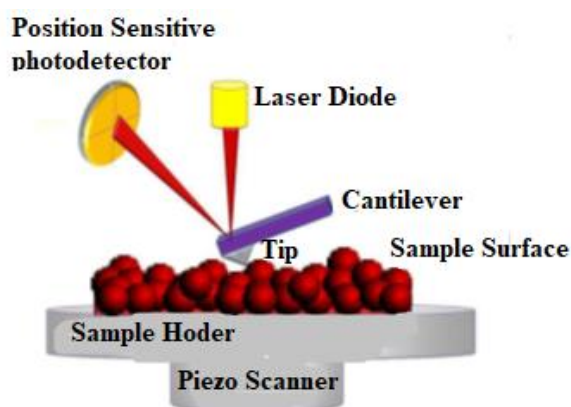


Figure 3.3 Principle of Atomic Force Microscopy

AFM uses a sharp tip to probe the superficial features by scanning and can image the surface topography with extremely high magnifications, up to one million times comparable or even better than electronic microscopes. The film's surface morphology and roughness of all inorganic perovskite thin films were characterized by AFM (AFM, model Park NX10).

3.3.8 Computational Methods

The computational method was calculated by the projector-augmented wave method, included in the VASP code, and was used for all DFT calculations. The Perdew-Burke-

Ernzerhof (PBE) parameterization of the generalized gradient approximation- underestimated (GGA-U) was used to describe the conversation correlation function, and the exchange-correlation function was used for all structural relaxation. The electronic band arrangements of the unit cells of perovskite were intended by Cambridge Serial Total Energy Package software (CASTEP, Materials Studio 2017, Vélizy Villacoublay, France)[38]. The unit cell in the Brillouin zone was employed to estimate the electronic band structures.

Chapter Four

4. Phase Behavior and Role of Organic Additives for Self-Doped CsPbI₃ Perovskite Semiconductor Thin Films

Abstract: The phase change of all-inorganic cesium lead halide (CsPbI₃) thin film from yellow δ -phase to black γ -/ α -phase has been a topic of interest in the perovskite optoelectronics field. Here the main focus is securing a black perovskite phase by avoiding a yellow one. In this work, we fabricated a self-doped CsPbI₃ thin film by incorporating an excess cesium iodide (CsI) into the perovskite precursor solution. Then, we studied the effect of organic additives such as 1, 8-diiodooctane (DIO), 1-chloronaphthalene (CN), and 1, 8-octanedithiol (ODT) on the optical, structural, and morphological properties. Specifically, we employed Flory-Hugging's theory based on the oligomer level of additives' molar mass to elucidate the binary additive-solvent solution thermodynamics. We found that the miscibility of additive-solvent displaying an upper critical solution temperature (UCST) behavior is in the sequence of CN: DMF > ODT: DMF > DIO: DMF, which trends could be similarly applied to DMSO. Black γ -phase exhibits in the XRD graph with referenced peak for self-doped and DIO & CN doped CsPbI₃ perovskite film showed phase improvements in line with the Selected area diffraction pattern of TEM. Multiple domains of self-doped CsPbI₃ with DIO and relatively flat images with CN show improvements in the morphology of the films. The FTIR result showed that self-doped CsPbI₃, self-doped with DIO, and self-doped with CN are similar structures indicating that after the yellow phase changes to the black γ -phase, the structure of the perovskite film was stable with self-doped and self-doped with DIO & CN the energy band gap reduced to 1.83 eV, 1.78 eV, and 1.76 eV respectively, showing an appropriate energy bandgap improvement for photovoltaic applications. Finally, the self-doping strategy with additive engineering should help fabricate a black γ -phase perovskite although the mixed phases of δ -CsPbI₃, γ -CsPbI₃, and Cs₄PbI₆ were observed in ambient condition. However, the results may provide insight into the stability of metastable γ -phase CsPbI₃ at room temperature.

4.1. Introduction

Metal halide perovskites (MHPs) have the general formula of ABX_3 , where A is methyl ammonium (MA) $CH_3NH_3^+$, formamidinium (FA) $CH(NH_2)_2^+$, methylhydrazinium $CH_3(NH_2)_2^+$, aziridinium $(CH_2)_2NH_2^+$, cesium (Cs), or rubidium (Rb), B is lead (Pb), tin (Sn) or manganese (Mn), and X is halide (Cl, Br, I) or its mixture [94-98]. MHPs can serve as a semiconducting active layer for photovoltaic (PV) cells, photodetectors (PD), light-emitting diodes (LEDs), field-effect transistors (FETs), and sensors [99, 100]. Due to the thermal instability of organic cations, all-inorganic cesium lead halide ($CsPbX_3$, X= Cl, Br, I) becomes an alternative material by incorporating the inorganic cesium instead of MA or FA [101-105]. $CsPbX_3$ is known to have long charge carrier diffusion length, strong light absorption, defect tolerance, thermal tolerance, narrow spectral bandwidth, tunable direct bandgap, high photoluminescence quantum yields (PLQY), and solution/melt processability [106-118]. The power conversion efficiency (PCE) of all-inorganic $CsPbX_3$ perovskite solar cells (PSCs) has reached ~21.15% [119] whereas the best PCE of $FAPbI_3$ solar cell is ~ 26% in 2023 [120].

Among cesium lead halides, the cubic phase α - $CsPbI_3$ has the smallest tolerance factor $t = (r_A + r_X) / \{\sqrt{2} \cdot (r_B + r_X)\} = 0.805$, where r_A , r_B , and r_X are the radius of cation A, cation B, and anion X, respectively [121,122]. This t value slightly falls out from the structural stability condition of $0.813 \leq t \leq 1.107$, indicating that α - $CsPbI_3$ may undergo a rapid phase transformation below 320 °C [123]. Hence, α - $CsPbI_3$ (black cubic) is structurally unstable and converted into β - $CsPbI_3$ (black tetragonal), γ - $CsPbI_3$ (black orthorhombic), and δ - $CsPbI_3$ (yellow orthorhombic) at room temperature [106-126]. Specifically, δ - $CsPbI_3$ is non-perovskite but thermodynamically most stable at room temperature, suggesting that this phase should be avoided for perovskite optoelectronics. However, because of its energy bandgap (E_g) of 1.73 eV [105] affording a significant photon harvesting, $CsPbI_3$ has received more attention than the other cesium lead halides ($CsPbCl_3$ with $E_g = 3.03$ eV and $CsPbBr_3$ $E_g = 2.23$ eV) for PeSC applications [127-128]. In this process, the researchers have tried to overcome the intrinsic phase instability of $CsPbI_3$ through additive engineering, quantum dots, dimension engineering, composition engineering, metal ion doping, solvent engineering, surface/defects passivation, and interfacial engineering [129-136].

In 2015, Snaith and coworkers demonstrated the working all-inorganic $CsPbI_3$ solar cell for the first time, in which hydroiodic acid (HI) was identified to stabilize γ - $CsPbI_3$ at a relatively lower temperature, ~100°C [137]. Marronnier et al. observed the temperature-dependent

phase transformation from orthorhombic-to-cubic ($\delta \rightarrow \alpha$) upon heating whereas cubic-tetragonal-orthorhombic ($\alpha \rightarrow \beta \rightarrow \gamma$) upon undercooling, indicating that CsPbI₃ could temporally retain its black γ -phase at room temperature [138]. Zhang et al. improved the crystal structure stability of γ -CsPbI₃ through interface engineering by depositing γ -CsPbI₃ on the top of iodine-doped reduced graphene oxide [139]. Wang et al. enhanced the γ -phase CsPbI₃ stability and minimized trap density through controlling crystallization dynamics by chlorine doping [140]. Liu and coworkers demonstrated that the γ -phase could be stabilized by reducing defect densities acting as both recombination center and ion migration space, for which they employed an acyloin ligand (1,2-di(thiophen-2-yl)ethane-1,2-dione (DED)) as a phase stabilizer and defect passivation [118]. Huang et al. recognized that the intrinsic instability of γ -phase originates from the small ion radius of cesium. Hence, to solve this problem, they incorporated small amounts of poly (alkyl amine hydrochloride) (PAACl) additive to the perovskite precursor solution and improved the stability of γ -phase CsPbI₃ [141]. Vaynzof and coworkers demonstrated the fabrication of a relatively stable γ -CsPbI₃ thin film through co-evaporation of CsI and PbI₂ with a small amount of phenylethylammonium iodide (PEAI), affording a preferable crystal orientation (columnar domains) with reduced defect densities [142]. Recently, Zhu and coworkers identified the excess CsI itself (i.e., more than 1 = CsI/PbI₂) identified a favorable formation of black γ -phase instead of yellow δ -phase, which is interesting in that it used a self-component rather than external one [143].

Additive engineering has been frequently employed to enhance the performances of polymer solar cells (PSCs) and PSCs [130, 144, 145]. In the case of PSCs, the phase-separation scale should be controlled within the exciting diffusion length (~10-47 nm depending on fullerene or non-fullerene acceptor and conjugated polymer) [146-148]. On the other hand, in the PeSCs, it is important to control the nucleation and crystal growth of perovskite from the colloidal perovskite precursor dispersion via intermediate phase engineering (IPE) [149,150], which is for obtaining a high-quality perovskite layer (ideally a single crystal but practically a polycrystalline with minimized defects). Specifically, 1, 8-diiodooctane (DIO), 1-chloronaphthalene (CN), and 1,8-octanedithiol (ODT) have been commonly used for organic electronics [151-155].

In 2007, Heeger and coworkers demonstrated that the addition of a few volume percent of alkanedithiols including ODT has contributed to the enhancement of PCE from 2.8% to 5.5% through improving the bulk-heterojunction morphology of PSCs [156-158]. Then in the next year the same group identified that DIO was the best among 1,8-di(R)octanes (R: SH, Cl, Br,

I, and CO_2CH_3) as an additive for PSCs and suggested two criteria: (a) selective solubility of the electron acceptor and (b) high boiling point of additive [158]. Then to date, this additive strategy has been continuously applied for non-fullerene-acceptor (NFA)-based PSCs as well as all-polymer solar cells (all-PSCs) [151, 158]. For example, in 2020, Li et al. observed the vertical composition and crystallinity could be regulated by employing the DIO additive, contributing to the photophysical properties of the active layer in NFA-based PSCs [153]. Then, in 2021, Boa et al. observed the synergetic effect of two additives, CN and thiophene derivative, on the optimization of the active layer in terms of phase separation and molecular packing, resulting in high-efficiency NFA-based PSC [152]. Recently, Liu et al demonstrated CN promoted the self-aggregation of polymer donors in all-PSCs [151]. However, in the field of PeSCs, conventional solvent additives such as DIO, CN, and ODT are relatively less studied for all-inorganic PeSCs although there are some for the hybrid PeSCs [159-163]. For example, in 2014, Jen and coworkers demonstrated that the bidentate halogenated additive, DIO can enhance the crystallization of MAPbCl_3 through a temporal chelation between DIO and PbCl_2 , i.e., enhancement of solubility of PbCl_2 [159]. In 2015, Chen and coworkers proved that the CN additive is beneficial in regulating the crystallization of $\text{MAPbI}_{3-x}\text{Cl}_x$ [160]. In 2018, Peng et al. observed that the DIO additive also could enhance the crystallinity of $\text{MAPbI}_{3-x}\text{Cl}_x$ for high-efficiency PeSCs just like CN [161]. In the same year, Tsai et al. proved that DIO is useful for the crystallinity, coverage, and uniformity of the MAPbI_3 thin film for PeSCs [162]. Then recently, Ghorai et al. reported the ligand-mediated revival of degraded α -phase CsPbI_3 nanocrystals by using 1-dodecanethiol (DSH), in which a heavily distorted α - CsPbI_3 could be converted to the cubic CsPbI_3 phase via the trigonal Cs_4PbI_6 through the etching with the surface ligand/passivator, DSH [163].

In this study, we studied the all-inorganic CsPbI_3 perovskite thin film doped with the excess cesium iodide with molar ration, $\text{CsI/PbI}_2= 2$, which was inspired by Qui et al.'s interesting results with $\text{CsI/PbI}_2= 1, 1.05, 1.5$ and 4 in a nitrogen filled glove box [143]. However, in our case, we carried out all the experiments in ambient conditions, indicating the results may suggest air processability and stability for the CsPbI_3 thin film. Then we examined the organic additive (DIO, CN, and ODT) effects on the structural, optical, and morphological properties of the self-doped CsPbI_3 thin film for the first time. Hence, through this work, the dual effects, self-dopant and external additives can be elucidated in air. Furthermore, we report the phase behavior of binary additive-solvent system for the first time based on the Flory-Huggins theory, presenting the role of additive in a typical solvent (DMF and DMSO) medium used for perovskite electronics.

4.2. Materials and Methods

4.2.1 Materials

The materials used for the experimental works are lead iodide (PbI_2 , 99.99%, Sigma-Aldrich, Darmstadt, Germany), cesium iodide (CsI , 99.99%, Sigma-Aldrich, Darmstadt, Germany), DMF (99.5%, AR chemicals, Delhi, India), DMSO (99 %, AR chemicals, Delhi, India), chlorobenzene ($\geq 99.5\%$, AR chemicals, Delhi, India), 1,8-diiodooctane (DIO, 98%, TCI chemicals, Tokyo, Japan), and 1-chloronephthaline (CN, 99%, TCI chemicals, Tokyo, Japan), and 1,8-octanediithiol (ODT, 95%, TCI chemicals, Tokyo, Japan) were used as received without a further purification.

4.2.2 Methods

The perovskite precursors (0.8 mmol CsI and 0.4 mmol PbI_2 without/with organic additives) were dissolved in 600 μL DMF and 400 μL DMSO solvent mixtures and stirred overnight at room temperature. Here, the additive was DIO, CN, or ODT, which was 2% of the DMF/DMSO mixed solvents by volume. Then, the perovskite precursor solution was filtered by a polytetrafluoroethylene (PTFE) syringe filter with 0.22 μm pore size. Then, 70 μL of colloidal perovskite precursor dispersion was dispensed on the top of the ITO glass substrate. Here, the spin coating was processed with 1,000 rpm for 10 sec and then 4,000 rpm for 40 sec. During spinning (after ~ 20 sec), 200 μL CB antisolvent was dispensed on the top of the wet perovskite precursor film. Then, the thin-film samples were gently annealed on a hotplate at 120 $^\circ\text{C}$ for 10 min and cooled down to room temperature for further characterization. Note that Qiu et al. [143] annealed their thin film on 320 $^\circ\text{C}$ (i.e., a phase transition temperature for black α -phase CsPbI_3 with cubic structure) for 3 min in a N_2 -filled glove box. However, we processed our thin film in the air without transferring to a glove box because we have an interest in the air stability of all-inorganic CsPbI_3 samples.

4.2.3 Characterization

The ultraviolet-visible (UV-Vis) absorption data were obtained using UV-Vis spectroscopy (SHIMADZU UV-2600, Kyoto, Japan) in the 300-800 nm wavelength range. The photoluminescence (PL) emission spectra of the self-doped CsPbI_3 thin films were acquired using a spectrophotometer (SHIMADZU RF-6000, Kyoto, Japan) at the excitation wavelength of 420 nm the PL peak was found to range in between 570-670 nm. The PL decay curves were recorded by using a time-correlated single photon counting (TCSPC) (Model: Fluorolog 3 TCSPC, Horiba, USA). The transmission electron microscopy (TEM) images were obtained by using a high-resolution TEM (HR-TEM, Model: JEOL, JEM-2100,

Peabody, MA, USA) with an operating voltage of 200 kV. The structural properties of the self-doped CsPbI₃ thin films were investigated by using the X-ray diffraction (XRD) analyzer (model: the Rigaku mini flex-300/600 diffractometer, Tokyo, Japan) in the angle range between $2\theta = 10^\circ - 80^\circ$. The microstructural morphologies of the thin films were characterized by using the field-emission scanning electron microscopy (FE-SEM, MAIA 3XMH TESCAN, and Kohoutovice, Czech Republic). The atomic force microscopy (AMF) tapping-mode images were obtained by using the Park NX10 AFM (Park Systems, Suwon, Korea). The Fourier-Transform infrared spectroscopy (FT-IR) analysis was performed in a transmittance mode by using the PerkinElmer Spectrum Two FT-IR Spectrometer (Waltham, MA, United States). Here, the attenuated total reflection (ATR) was employed to record the FT-IR spectra of the self-doped CsPbI₃ thin films without/with organic additives in the range 4000-400cm⁻¹ with a resolution of 4 cm⁻¹ [164].

4.2.4. Computational methods

The electronic band structures of the unit cells (δ -CsPbI₃ and γ -CsPbI₃) were calculated using the Cambridge Serial Total Energy Package (CASTEP, Materials Studio 2017, Vélizy-Villacoublay, France) software. The Perdew-Burke-Ernzerhof (PBE) parameterization of the General Gradient Approximation (GGA) was used to portray the exchange-correlation function. The unit cell in the Brillouin zone was employed to estimate the electronic band structures. For the geometry optimization, the energy, maximum force, maximum displacement, and maximum stress were 5×10^{-5} eV/atom, 0.01 eV/Å, 5×10^{-4} Å, and 0.02 GPa, respectively.

4.3. Results and Discussion

Figure 4.1 shows the chemical structures of (a) additives (DIO, CN, and ODT) and (b) solvents (DMF, DMSO and CB). Here CB was used as an antisolvent during the solvent engineering process. Tables 1 and 2 summarize the properties of additives and solvents, respectively. Specifically, DMF and DMSO have Guttmann's donor number (D_N) of 26.6 kcal/mol and 29.8 kcal/mol whereas CB has $D_N = 3.3$ kcal/mol, indicating that DMF and DMSO can have a strong coordination bonding with haloplumbate containing Lewis acid Pb²⁺ but CB cannot [164]. Therefore, the less polar CB molecule could act as an antisolvent, which has a weaker basicity as well as a smaller solubility parameter (δ) of $9.5 \text{ (cal/cm}^3)^{1/2}$ than the other two solvents (DMF and DMSO) [163,165].

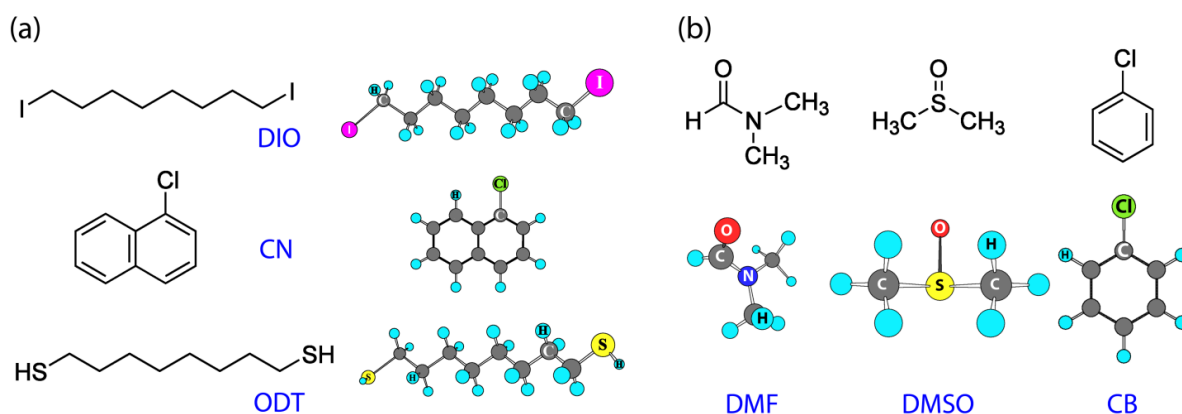


Figure 4. 1 Chemical structure of organic additives and solvents. (a) Organic additives: DIO, CN, and ODT. (b) Solvents: DMF, DMSO, and CB

Table 4.1 Group contribution to (cohesive energy) for estimating the solubility parameter (δ)

Here, E_{coh}^{group} and E_{coh} are cohesive energy per group and entire molecule, respectively. MW_2 is molecular weight, ρ_2 is density, v_2 is the molar volume of organic additives, b.p. is boiling point, and δ_2 is solubility parameter, respectively. Here, the subscript-2 denotes an additive molecule whereas the subscript-1 will be used for solvent [166, 167].

Additive	Group	E_{coh}^{group} (J/mol)	Group Number	E_{coh} (J/mol)	MW_2 (g/mol)	ρ_2 (g/cm ³)	V_2 (cm ³ /mol)	b.p. (°C)	δ_2 (MPa) ^{1/2}	δ_2 (cal/cm ³) ^{1/2}
DIO	-CH ₂ -	4,190	8	71,620	366.02	0.818	447.5	167-169	19.0	9.3
	-I	19,050	2							
CN	-Cl	12,990	1	58,056	162.62	1.194	136.2	111-113	20.7	10.1
	-CH=CH-	10,200	3							
	>C=C(H)	4,860	1							
	>C=C<	9,606 ^a	1							
ODT	-CH ₂ -	4,190	8	77,050	178.36	0.970	183.9	269-270	18.8	9.2
	-S-	8,800	2							
	-H	12,965 *	2							

* It was estimated from the solubility parameter data in the literatures [168, 169].

Table 4.2 Properties of solvents and antisolvent. MW_1 is molecular weight, ρ_1 is density, \hat{V}_1 is the molar volume of solvent, b.p. is boiling point, δ_1 is solubility parameter [165], and D_N is Guttmann's donor number [164], receptively. Here, the subscript 1 denotes the solvent molecule.

Solvent	MW_1 (g/mol)	ρ_1 (g/cm ³)	\hat{V}_1 (cm ³ /mol)	b.p. (°C)	δ_1 (MPa) ^{1/2}	δ_1 (cal/cm ³) ^{1/2}	D_N (kcal/mol)
DMF	70.09	0.948	73.9	153	24.8	12.1	26.6
DMSO	78.13	1.100	71.0	189	29.7	14.5	29.8
CB	112.56	1.110	101.4	132	19.5	9.5	3.3

In this study, for preparing a perovskite precursor solution, we used the mixed solvents composed of DMF: DMSO = 3:2 volume ratios according to the literature report [170]. Then, we added DIO, CN, or ODT as a solvent additive into the perovskite precursor solution, resulting in the change of solvent quality, good or poor. Hence, we investigated the phase behavior of binary additive-solvent systems. Note that although we used a mixed DMF: DMSO solvent system, we should decouple it for understanding phase behavior theoretically.

The Flory-Huggins theory can describe polymer solution thermodynamics [171-173]. In this study, the processing solvent additives can be treated as an oligomer. Note that oligomer has a molecular weight whose degree of polymerization ≤ 10 . Compared to the solvents such as DMF and DMSO, the molecular size of the organic additives (DIO, CN, and ODT) falls into the oligomer level (see Tables 4.1 and 4.2). Hence, for the binary additive-solvent mixture modeled as an oligomer-solvent system, the Gibbs free energy of mixing could be expressed as eqn. (1) according to Flory-Huggins theory [171]

$$\frac{\Delta G_{mix}}{RT} = \frac{\phi_1}{r_1} \ln \phi_1 + \frac{\phi_2}{r_2} \ln \phi_2 + \chi_{12} \phi_1 \phi_2 \quad (1)$$

where $\phi_1, \phi_2, r_1,$ and r_2 are the volume fraction and relative molar volumes of components 1 (solvent) and 2 (additive), respectively. In addition, $R [= 1.987 \text{ cal/ (K}\cdot\text{mol)}]$ and T (K) are the gas constant and temperature, respectively. Importantly, the χ_{12} interaction parameter could be defined as $\chi_{12} = \hat{V}_1 / RT (\delta_1 - \delta_2)^2$ [171, 174], where \hat{V}_1 is the molar volume of solvent whereas δ_1 and δ_2 are the solubility parameter of the component 1 and 2, respectively.

Table 3 shows the χ_{12} and r_2 for each system when $r_1 = 1$ for a solvent (DMF or DMSO). Then the binodal curve can be calculated based on the below two equilibrium equations.

$$\Delta\mu_1^\alpha = \Delta\mu_1^\beta \quad (2)$$

$$\Delta\mu_2^\alpha = \Delta\mu_2^\beta \quad (3)$$

Where $\Delta\mu_i = \partial\Delta G_{mix} / \partial n_i$ is the chemical potential of component, $i (= 1, 2)$ and α & β are oligomer-lean phase and oligomer-rich phase, respectively [171-173].

Table 4.3 Flory-Huggins interaction parameter (χ) and molar volume ratio (r) when for the solvent such as DMF or DMSO.

System	DIO:DMF	CN:DMF	ODT:DMF	DIO:DMS O	CN:DMSO	ODT:DMS O
χ_{12}	291.6/T	148.8/T	312.8/T	966.2/T	691.8/T	1003.7/T
r_2^*	6.1	1.8	2.5	6.3	1.9	2.5

* Note that $r_2 \leq 10$ indicates that the component 2 can be treated as a model oligomer.

Figure 4.2 shows the temperature-composition phase diagrams (i.e., the binodal curves) of (a) additive: DMF and (b) additive: DMSO systems, which were constructed by solving equations (2) and (3), simultaneously. First all, the original Flory-Huggins theory can capture a big essential picture without losing the physical meaning [171], indicating that we should understand the predicted phase behavior qualitatively, not quantitatively. Second, as indicated in Table 4.3, the phase behavior is largely governed by χ_{12} and r_2 . Third, small χ_{12} denotes better miscibility between additive and solvent, indicating that the additive-DMF system is better miscible than the additive-DMSO system (see Table 4.3). In Figure 4.2, the additive-solvent miscibility has a similar sequence for both solvents, (a) CN: DMF > ODT: DMF > DIO:DMF for the additive-DMF solution, and (b) CN:DMSO > ODT:DMSO > DIO:DMSO for the additive-DMSO solution. However, the additive-DMF solution shows the immiscibility region below room temperature (< 300 K) whereas the additive-DMSO solution displays it at a higher temperature (< 1,000 K), indicating that the additive-DMF system has a better miscibility than the additive-DMSO mixture. Hence, in the DMF: DMSO= 3:2 mixture, if we employ an organic additive, the solvent quality is going to be down, specifically because the additive is not much miscible with DMSO. Hence, we can expect that versatile iodide plumbate (PbI_n^{2-n} with $n=2-6$) are going to be more aggregated (i.e., self-interactions are increased) if the additive is present in the perovskite precursor solution. Here it is noteworthy that (1) the perovskite precursor solution is a colloidal dispersion, and (2) DMF and DMF-DMSO mixture are retrograde solvent systems [175-176]. Hence, the addition of organic additive will have the similar effect to the raise of temperature in the sense that the self-interactions among haloplumbate are enhanced, which may affect the perovskite crystallization process resulting in a different morphology of the final perovskite thin films. See Figure 4.S1 and Table 4.S1 in Supplementary Materials for the Flory-Huggins interaction parameter at 298 K (= 25 °C).

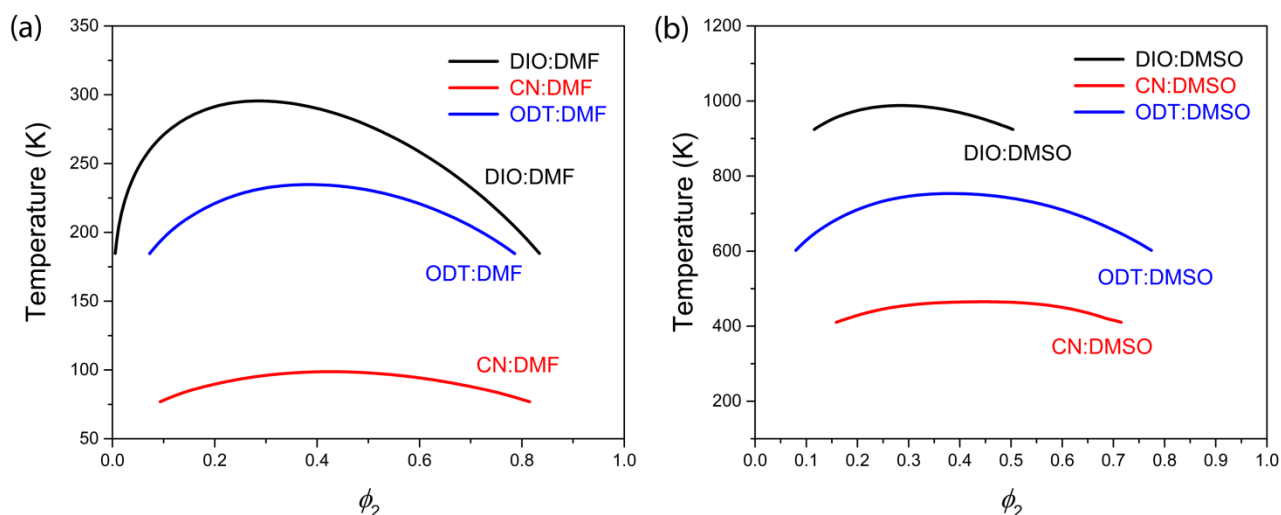


Figure 4. 2 Phase diagrams of binary additive-solvent systems: (a) additive-DMF system, and (b) additive-DMSO system.

Here, the additive could be DIO, CN or ODT, which has a molar volume with oligomer level compared to the typical solvents such as DMF and DMSO.

At room temperature, the thermodynamically stable phase for CsPbI_3 is yellow δ -phase [104, 124-125]. However, when temperature is increased to 587 K, it can undergo a phase transition into black α -phase [124-126]. Then when α -phase was cooled down, it can transform to β -phase at 554 K and to γ -phase at 457 K. Hence, at room temperature, CsPbI_3 could stay in yellow δ -phase (Figure 4.3a) or black γ -phase (Figure 4.3b), which are both orthorhombic. In this work, to escape yellow δ -phase (i.e., non-perovskite), we added excess CsI into the perovskite precursor solution, which we call ‘self-doping’ because CsI is a part of its original precursor solution. However, when we add an excess CsI, it is known that Cs_4PbI_6 could be formed together with γ -phase CsPbI_3 [177] (see Figure S2 for the trigonal phase of Cs_4PbI_6). For clarification, at this moment, it is noteworthy that in the field of conjugated polymer, ‘self-doping’ indicates the polymer contains charge and become polyelectrolyte [178]. However, here we use the ‘self-doping’ for the case of the perovskite doped with its own component (i.e., perovskite precursor) by excess addition.

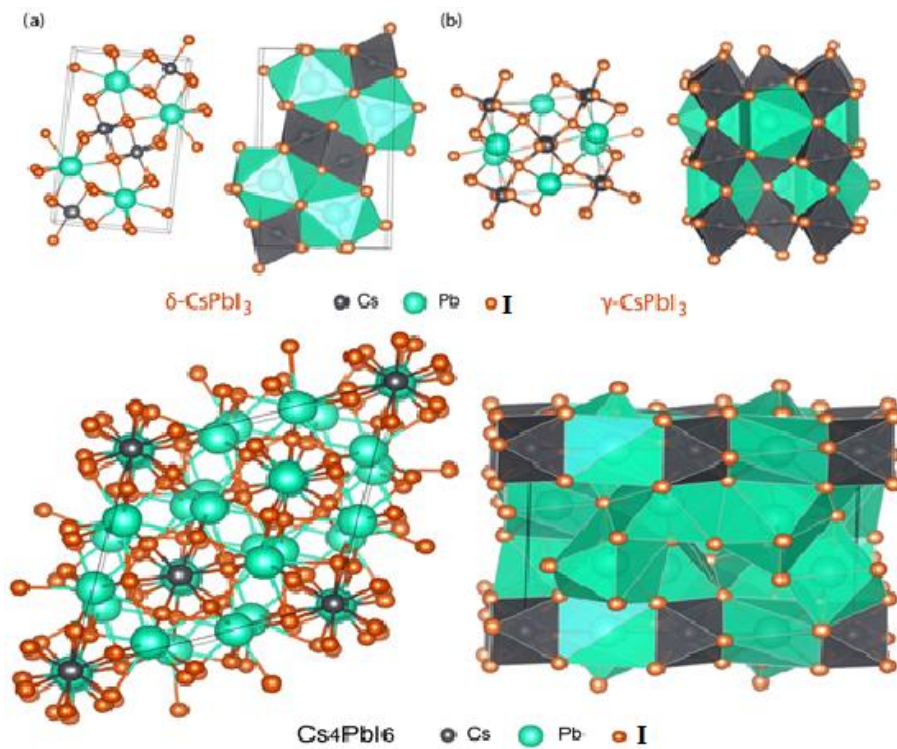


Figure 4.3 Crystal structures of (a) yellow δ -phase CsPbI₃ and (b) black γ -phase CsPbI₃

Figures 4.4a and b show the electronic band structure for (Figure 4.4a) yellow δ -phase and (Figure 4.4b) black γ -phase CsPbI₃, calculated based on the unit cell structure shown in Figure 4.3. Figure 4.4c and d display the density of states for structure for δ -phase and γ -phase CsPbI₃, respectively. Here, the estimated energy bandgap is 2.87 eV for δ -phase and 1.90 eV for γ -phase, respectively. The results are slightly larger than the experimental values which will be explained in Figure 4.9 of Uv-Vis absorption and energy bandgap section.

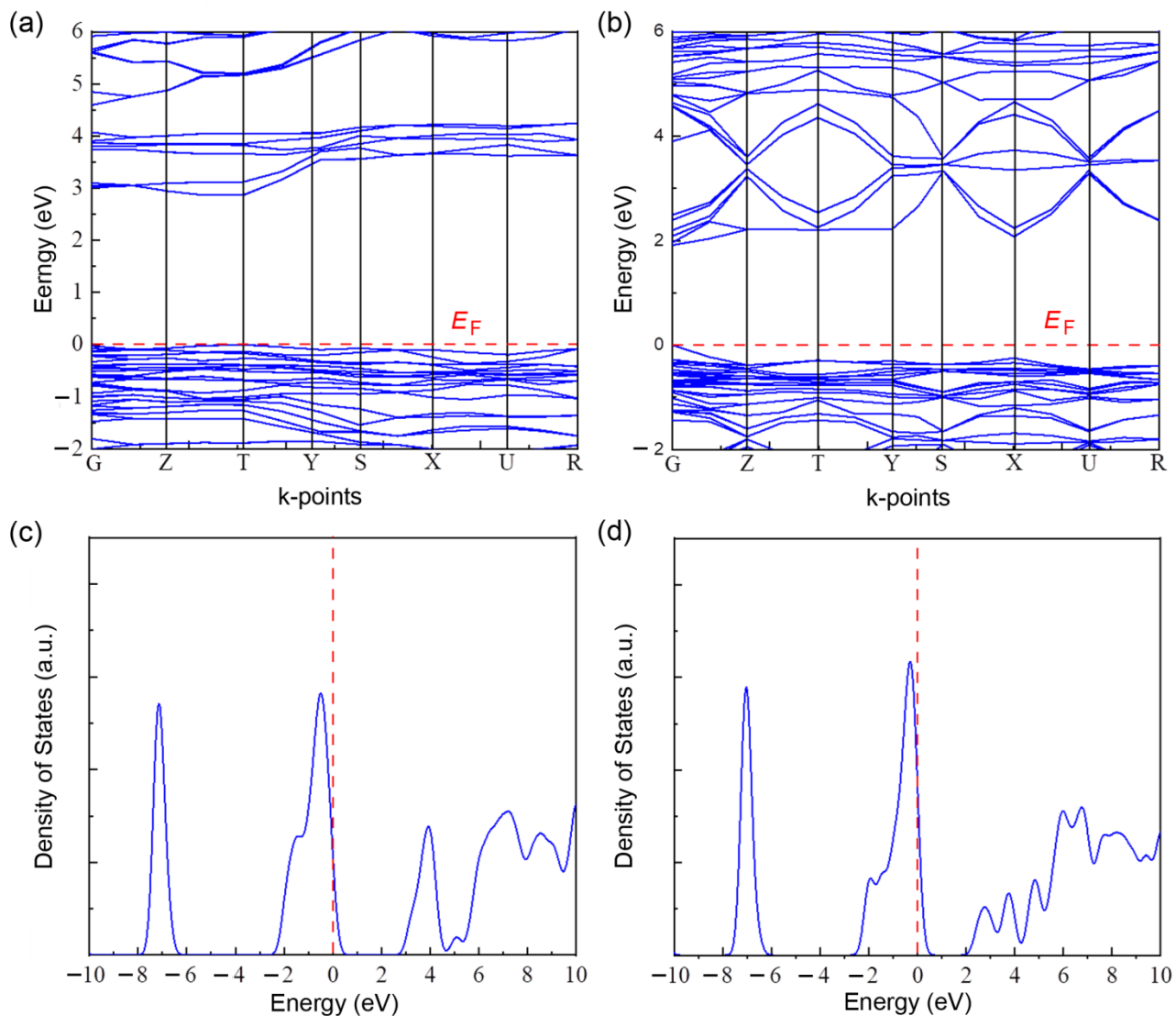


Figure 4. 4 (a) Yellow δ -phase CsPbI₃ with the energy bandgap, $E_g= 2.87$ eV, and (b) black γ -phase CsPbI₃ with $E_g= 1.90$ eV. Density of states: (c) Yellow δ -phase CsPbI₃ and (d) black γ -phase CsPbI₃. Here, E_F stands for Fermi energy

Figure 4.5a shows the XRD pattern of self-doped CsPbI₃ without additives whereas Figure 4.5b displays the XRD patterns of self-doped CsPbI₃ with the organic additives, DIO, CN, and ODT, which may highlight the results of air-processed cesium lead iodide samples. First of all, when CsPbI₃ was prepared with excess CsI, we can observe γ -phase CsPbI₃ with orthorhombic structure. However, at room temperature, the most stable structure is unfortunately δ -phase CsPbI₃. Specifically, when γ -phase CsPbI₃ is exposed to a humid condition, it is known that it transforms into the stable δ -phase CsPbI₃ (non-perovskite as shown in Figure 4.3a) [179]. Furthermore, the excess CsI compounds afford the formation of the trigonal Cs₄PbI₆ phase. Hence, as shown in Figure 4.5a, the self-doped CsPbI₃ shows the XRD patterns mainly originating from the three compounds such as γ -/ δ -phase orthorhombic

CsPbI₃ and trigonal Cs₄PbI₆ [180]. Note that in this study, the reaction condition was 2CsI + PbI₂, which could be sources for the reactions of CsI+PbI₂ and 4CsI+PbI₂, producing γ -/ δ -CsPbI₃ and Cs₄PbI₆ and others. Interestingly, Cs₄PbI₆ is known to be used for synthesizing CsPbI₃ compounds [181]. Hence, as shown in Figure 8a, the self-doped CsPbI₃ sample's black γ -phase exhibits the XRD peaks at $2\theta = 13.9^\circ, 19.9^\circ, 28.1^\circ, 32.1^\circ,$ and 41.3° , corresponding to the orthorhombic crystallographic planes, (020), (200), (040), (013), and (242), respectively. On the other hand, its yellow δ -phase displays the XRD peaks at $2\theta = 10.6^\circ, 13.2^\circ, 27.2^\circ, 31.2^\circ,$ and 36.8° , corresponding to the crystallographic planes, (002), (102), (122), (016), and (043), respectively. Note that for this peak assignment, the Inorganic Crystal Structure Database (ICSD), 4127359 and 27979, were used for γ -phase and δ -phase, respectively. In the case of Cs₄PbI₆, the XRD peaks are observed at $2\theta = 12.0^\circ, 23.4^\circ, 26.4^\circ, 42.0^\circ,$ and 53.9° , corresponding to the trigonal crystallographic planes, (012), (300), (131), (060), and (354), respectively [182]. Figure 8b shows the XRD patterns for the self-doped CsPbI₃ with versatile organic additives, DIO (brown), CN (violet), and ODT (green solid line). As shown in Figure 4.5b, in the case of the green-colored data, the additional small-multiple peaks were observed indicating that the phase purity is worst among the samples. Remind that only the self-doped CsPbI₃ ($E_g = 2.59$ eV) with the additive ODT displayed the significant blue shift in UV-vis spectra in Figure 4.9b and d, indicating that the useful black γ -phase might be minimized when ODT was employed as an organic additive for the self-doped CsPbI₃.

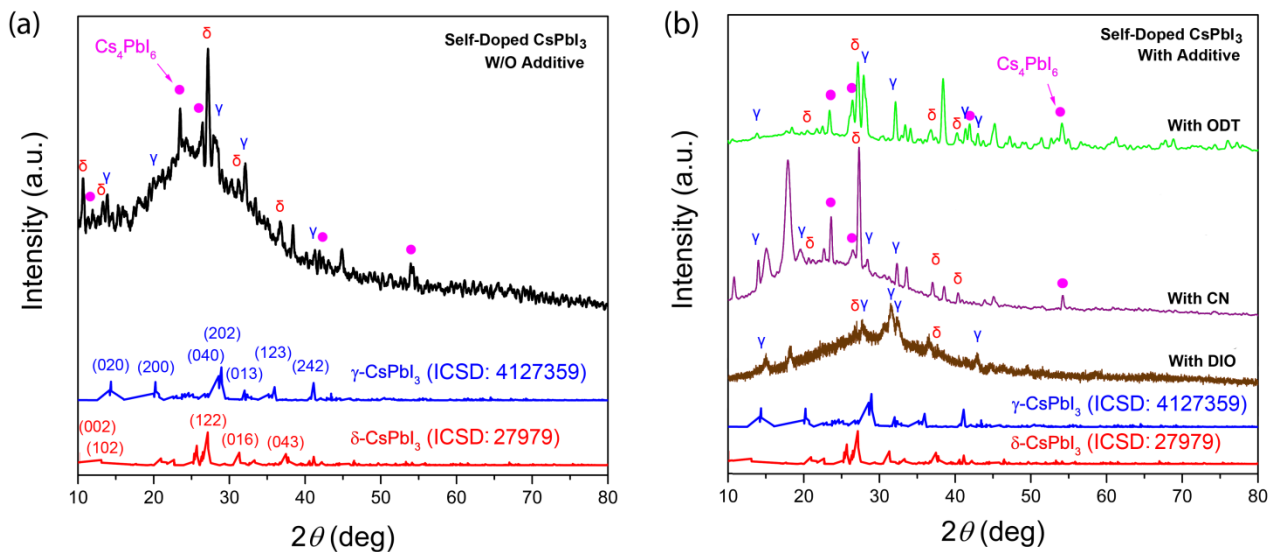


Figure 4. 5 XRD patterns for (a) self-doped CsPbI₃ without organic additive and (b) self-doped CsPbI₃ with organic additives such as DIO (brown), CN (violet) and ODT (green).

Note that the blue solid line is for γ -CsPbI₃ from Inorganic Crystal Structure Database (ICSD-4127359) whereas the red solid line is for δ -CsPbI₃ from ICSD-27979. The pink filled circles indicate the XRD peaks from the trigonal Cs₄PbI₆ phase [180].

We investigated whether the organic additive stays with the self-doped CsPbI₃ or not based on the FT-IR spectroscopy. Accordingly, we obtained Figure 4.6 explaining the functional group in the sample compounds. Largely speaking, the self-doped CsPbI₃ without/with additive (DIO or CN) are showing the characteristic FT-IR spectra with the three main peaks at 894 cm⁻¹, 758 cm⁻¹ and ~443 cm⁻¹ [183], indicating that DIO and CN molecules like other solvents such as DMF/DMSO did not stay in the perovskite film after thermal annealing at 120 °C for 10 min (within the detection limit of IR instrument). However, in the case of ODT-added sample, the film displays several additional peaks at 3774 cm⁻¹, 2920-2848 cm⁻¹ and 1483 cm⁻¹, originating from O–H vibration (from absorbed water) and/or C–C stretching vibration, C–H stretching, and C–H scissoring, respectively [184-187]. The presence of C-H vibration from ODT's alkyl moiety indicates that ODT could be ionized (i.e., R–SH → R–S⁻ + H⁺) and reacted with the perovskite precursor (haloplumbate). Note that alkylthiol (e.g., ODT) has been used to form a self-assembled monolayer on the surface of metal nanoparticles through the reaction between thiolate anion (RS⁻) and metal (e.g., Au) [188], suggesting the binding reaction between thiolate anion and haloplumbate (specifically, soft lead element). The characteristic peak between 894 cm⁻¹ - 443 cm⁻¹ originating from C-H stretching and C-O stretching for all perovskite films.

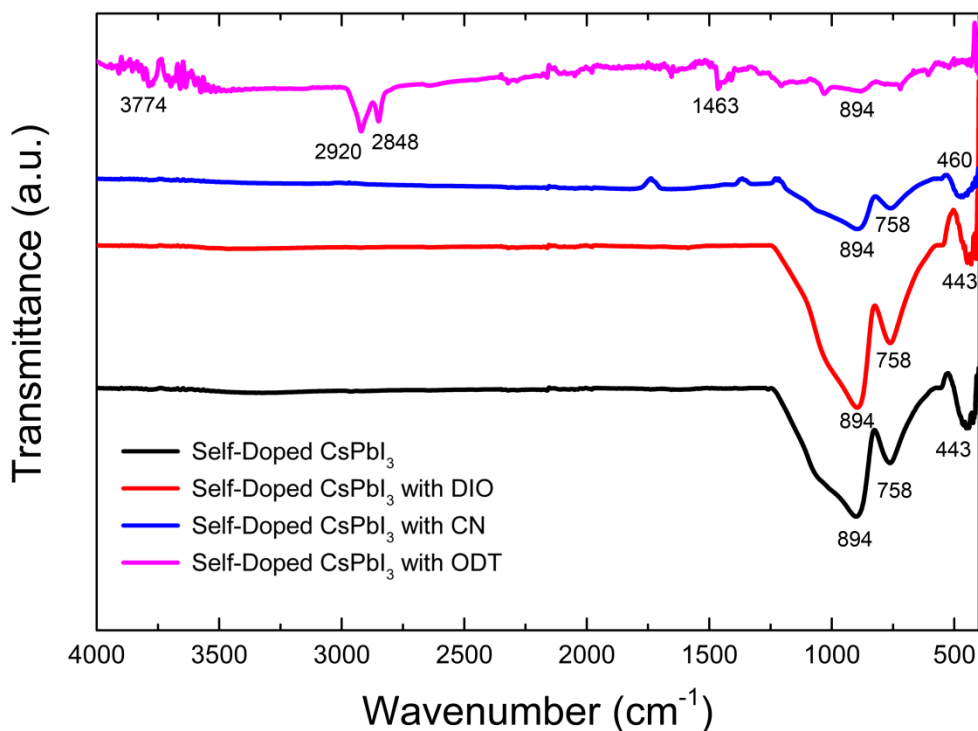


Figure 4. 6 FTIR spectra of self-doped CsPbI₃ without and with organic additives, DIO, CN, and ODT

Figure 4.7 shows SEM image of the self-doped CsPbI₃ without/with organic additives, DIO, CN, and ODT. The self-doped CsPbI₃ without additive displays the rod-like textural morphology (Figure 4.7a) whereas the self-doped CsPbI₃ with additives shows commonly some nano scale spots on the surface of films (Figure 4.7b, c, and d) which is in line with Kim et al.'s report [189]. However, depending on the additive species, the morphology is somewhat different. The self-doped CsPbI₃ with DIO shows a multiple domains whereas the sample with CN exhibits a relatively flat image. Interestingly, the self-doped CsPbI₃ with ODT displays some abnormal texture in the diagonal direction (flow-like image), indicating that a film is not uniform because of the ODT's special character (e.g., probably the ignitability of ODT; in this case, there might be columbic interactions and chemical reactions between thiol with haloplumbate in the perovskite precursor solution state). AFM tapping mode images could be found in Figure S4, in which the self-doped CsPbI₃ with ODT shows the rod-like shape instead of granular spots, indicating that the sample could be nonuniform (from different degree of phase transformation) when processed in air.

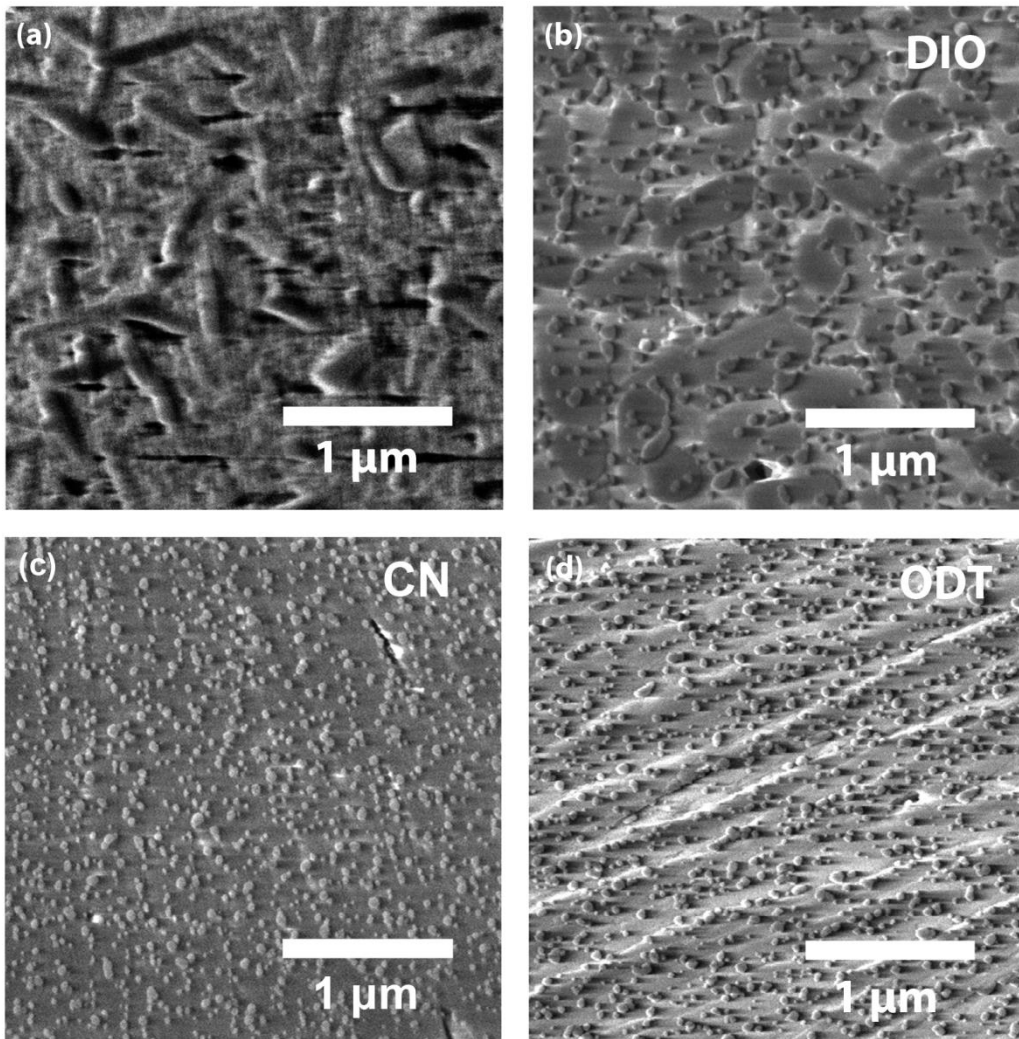


Figure 4. 7 SEM images: (a). Self-doped CsPbI₃, (b) self-doped CsPbI₃ with DIO, (c) self-doped CsPbI₃ with CN, and (d) self-doped CsPbI₃ with ODT

Importantly, for understanding both the two PL peaks and the two-step PL decay, we examined the high-resolution TEM (HR-TEM) image for the self-doped CsPbI₃. As shown in Figure 4.8, the selected area diffraction pattern (Figure 4.7a) as well as the high-resolution TEM image (Figure 4.8b) could be identified, displaying the nanocrystals embedded in the crystalline matrix. As an example, we selectively checked another sample, the self-doped CsPbI₃ with the additive ODT, the result could be found in Figure 4.S3, displaying a similar nanostructure image, i.e., the nanocrystals domains embedded in the crystalline matrix.

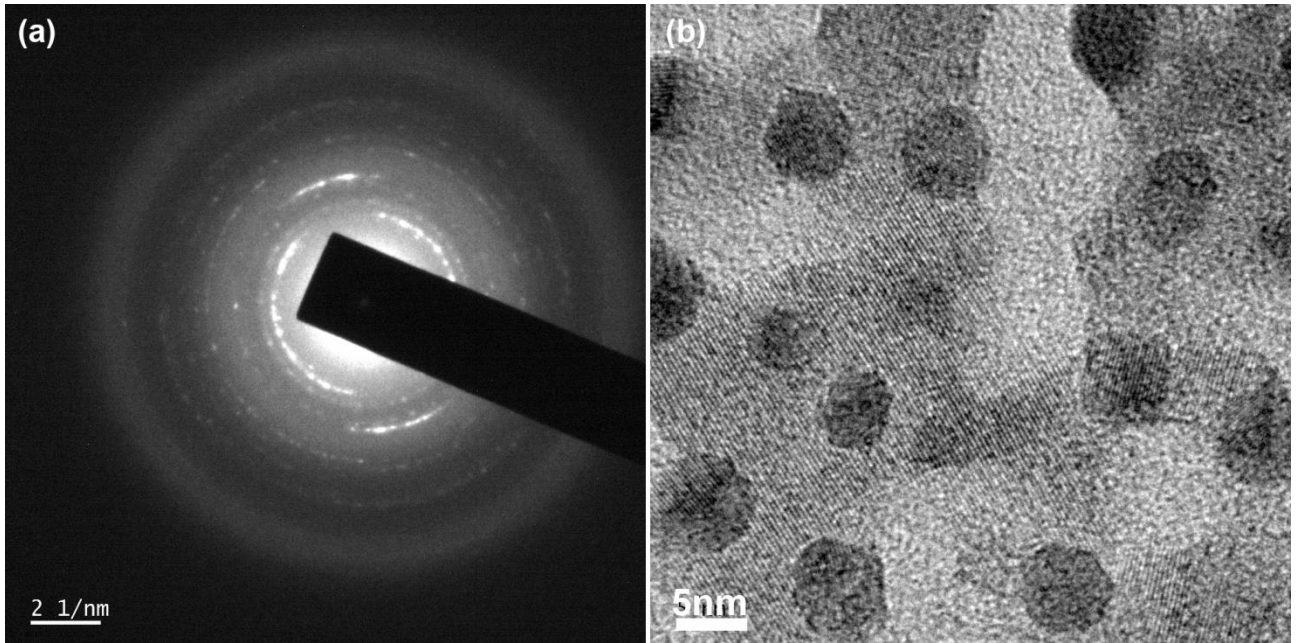


Figure 4. 8 (a) Selected area diffraction pattern and (b) high-resolution TEM image of the self-doped CsPbI₃ sample.

Figure 4.9a and b show Uv-vis absorption spectra for (a) the yellow δ -phase CsPbI₃ and (b) the self-doped CsPbI₃ without/with three organic additives (DIO, CN, and ODT). As shown in Figure 5a, when CsI: PbI₂ = 1:1 under ambient conditions, the resulting structure is a yellow δ -phase orthorhombic crystal (recall Figure 4.3a). On the other hand, Figure 4.9c and d display the determination of bandgap based on the Tauc plot, $(\alpha hv)^2$ vs. hv , where α is the absorption coefficient, h is Plank's constant, and ν is the frequency of incident photon [190]. Resultantly, the yellow δ -phase CsPbI₃ exhibits the optical bandgap (E_g) of 2.84 eV at the wavelength (λ , i.e., absorption edge) of 437 nm whereas the self-doped γ -phase CsPbI₃ displays $E_g = 1.83$ eV. However, when the organic additive (DIO, CN, and ODT) was incorporated into the perovskite precursor solution, the resulting film showed different energy bandgap like $E_g = 1.78$ eV at $\lambda = 697$ nm for DIO, $E_g = 1.76$ eV at $\lambda = 705$ nm for CN and $E_g = 2.59$ eV at $\lambda = 479$ eV for ODT, confirming that the presence of additive affected the crystallization process of perovskite (γ -phase) and non-perovskite (δ -phase). Here, it is notable that when the organic additive (DIO or CN) was incorporated into the film, E_g was reduced from 1.83 eV to 1.78 eV (DIO) or 1.76 eV (CN). This reduction suggests that the internal crystal structures of thin films were better organized when the additive was present in the perovskite precursor solution. The result was in line with γ -phase of XRD result (Figure 5), the structural property of FTIR result (Figure 4.6) and selected area of diffraction pattern

of TEM image (Figure 4.7). On the contrary, when the organic additive ODT was employed for the perovskite-film process, E_g was widened from 1.83 eV to 2.59 eV (but still smaller than $E_g = 2.84$ eV of yellow δ -phase), indicating that the contribution of γ -phase CsPbI₃ might be minimized in this sample. Here, we guess that if ODT is ionized ($R-SH \rightarrow R-S^+ + H^+$) in the perovskite precursor solution, the octacarbon-chainlike cation ($-S^+$) may partly increase the d -spacing of perovskite layers just like low dimensional perovskite [191-193] and/or the accompanying polarity change of a colloidal dispersion medium may induce the formation of more δ -CsPbI₂ and Cs₄PbI₆ with a larger bandgap under ambient condition.

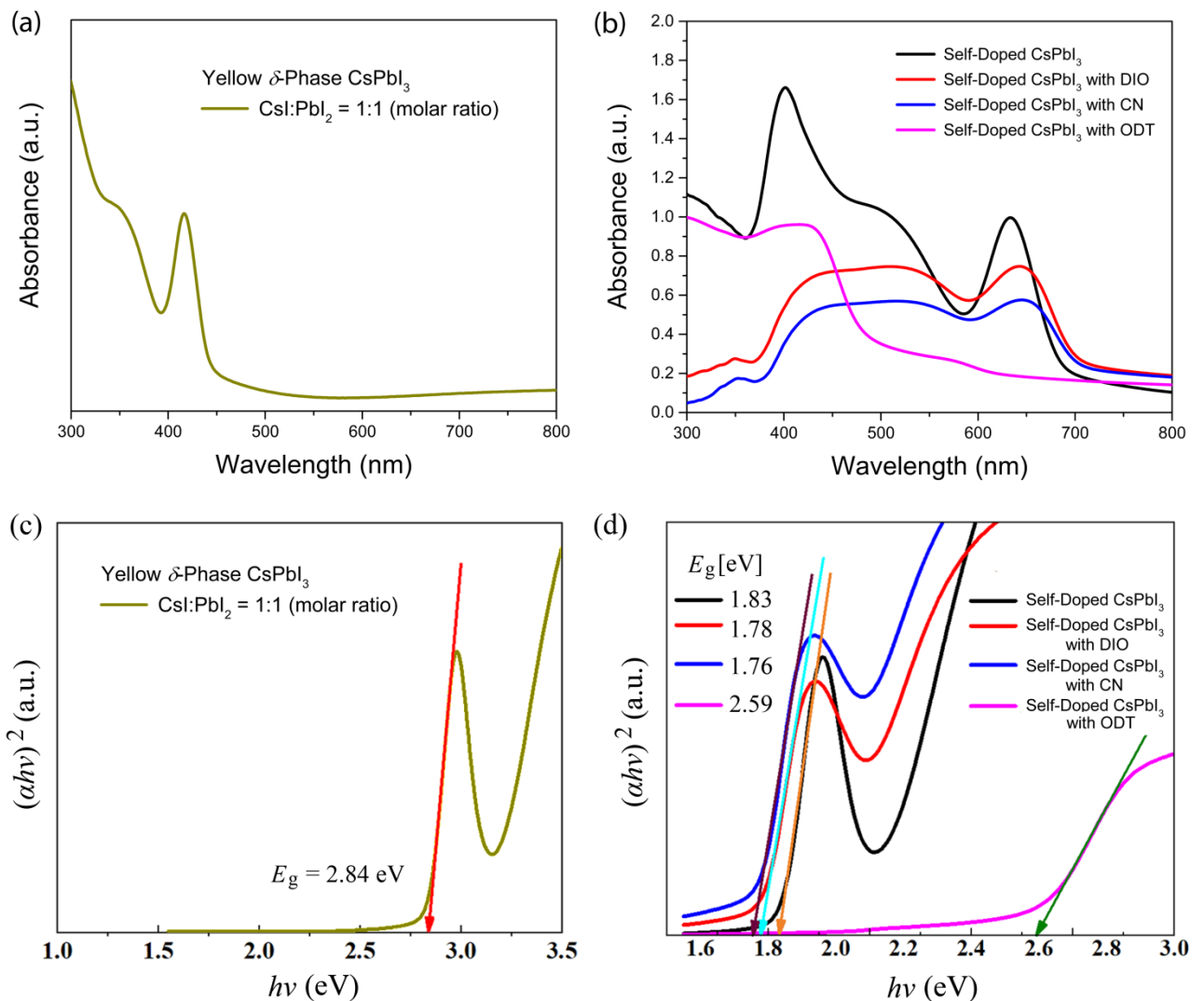


Figure 4. 9 UV-Vis absorption spectra of (a) yellow δ -phase CsPbI₃ and (b) black γ -phase CsPbI₃ and its derivative (e.g., Cs₄PbI₆ or low dimensional structure). Tauc plot for determining bandgap of (c) yellow δ -phase CsPbI₃ and (d) black γ -phase CsPbI₃ and its derivatives.

Finally we check whether the lifetime of the perovskite film improved or not using PL & PL lifetime analysis. Figure 4.10a shows the PL spectra of self-doped CsPbI₃ without/with organic additives. Interestingly, the PL spectra exhibit two different peaks at ~636 nm and 590 nm for the self-doped CsPbI₃ without additive (the black solid line in Figure 4.10a). However, when DIO, CN, and ODT were added for the self-doped CsPbI₃, the PL peak positions were shifted to 627nm/597 nm (DIO), 636nm/583nm (CN) and 637nm/586nm (ODT), respectively. Here, it is interesting that the PL peak position of ODT-added sample is comparable to those of others, which is different from the results of UV-Vis spectra in Figure 4.9b. One possibility is that in Figure 5b, there is a small bump around ~600 nm, which might be partially linked to the above PL emission. Here it is noteworthy that the environmental condition was air (not a controlled glove box), making the samples exhibit diverse characteristics (i.e., the degree of internal phase transformation might be different). Figure 6b displays time-resolved PL (TRPL) decay curve of self-doped CsPbI₃ without/with organic additives. First of all, the decay curve looks two steps, i.e., a normal decay and additional small bump, which makes the regular model (single, double, triple exponential fitting) not suitable for describing the PL decay data. Hence, according to the literature report [191], we estimate the PL lifetime at the 63% decay point in Figure 4.10 b. Resultantly, the PL lifetime is ~1.1 ns (self-doped CsPbI₃, DIO and CN) and ~0.9 ns (for self-doped CsPbI₃ with ODT). However, as shown in Figure 4.10b, there are PL decay tail curve, indicating that DIO > CN > ODT ≈ 'without additive'. Hence, we assume that the two PL peaks as well as the two-step TRPL decay curves related to displayed may be from the nanocrystals embedded in the crystalline matrix of the TEM image (Figure 4.7). Therefore, it seems that additive engineering contributes to the slight enhancement of PL lifetime.

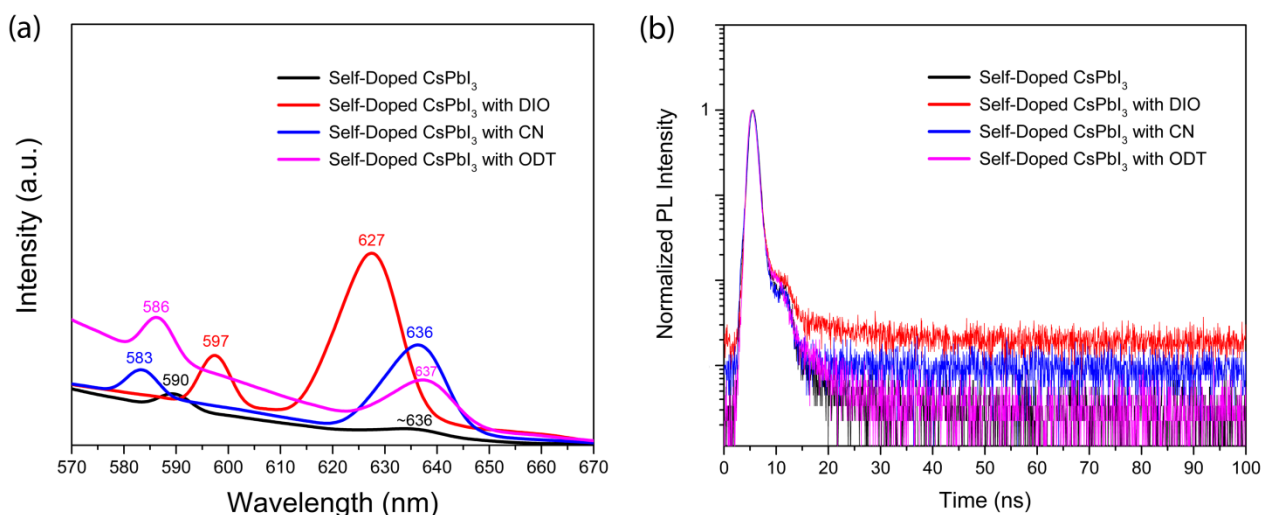


Figure 4. 10 Self-doped CsPbI₃ without/with organic additive: (a) PL emission spectra and (b) Time-resolved PL decay spectra.

4.4. Conclusions

We demonstrated that the self-doped CsPbI₃ with CsI: PbI₂=2:1 could be useful for retaining a black γ -phase mixture by escaping a pure yellow non-perovskite δ -phase under ambient condition. In addition, when DIO and CN were employed as an organic additive, the crystallization process was partially modified leading to the energy bandgap of 1.78 eV (DIO) and 1.76 eV (CN) instead of 1.83 eV (without additive). However, in the case of the CsPbI₃ with ODT, the bandgap become more wide like \sim 2.59 eV, which might originate from the ionizability of ODT affecting the crystallization process. Interestingly, the PL spectra shows two emission peaks and the PL decay curves displayed two steps, suggesting a compound mixture, about which HR-TEM showed the embedded nano-domains in a crystalline matrix. In the case of additive-solvent's phase behavior, the predicted miscibility is CN: DMF (or DMSO) > ODT: DMF (or DMSO) > DIO: DMF (or DMSO) based on the Flory-Huggins theory. Specifically, additive is less miscible with DMSO, indicating that the presence of additive (DIO, CN and ODT) makes the solvent medium be poorer than that without additive. Future work may include the tunability of the phase purity for the self-doped CsPbI₃ perovskite under ambient condition for the perovskite solar cell applications. Finally, considering the interchangeability between two orthorhombic phases (γ -phase and δ -phase) and between two crystalline compounds (Cs₄PbI₆ and CsPbI₃), our results provide insight on the stability of γ -phase CsPbI₃ perovskite thin film. In other words, the meta-stable γ -phase thin film processed under a controlled environment (e.g., N₂ filled glove box) will undergo a phase transformation and the phase purity will decrease with time.

Chapter Five

5. All-Inorganic Cesium Lead Mixed-Halide Perovskite CsPbI₂Br Thin Films: AgBr Doping Effects on Material Properties

Abstract: All-inorganic perovskite semiconductors have received a significant interest for their potential stability over heat and humidity. However, the typical CsPbI₃ displayed the phase instability in spite of its desirable bandgap of ~1.73 eV. Herein, we study the mixed halide perovskite CsPbI₂Br by varying Ag-doping concentration. For this purpose, we examined its bandgap tenability as a function of Ag-doping level by using density functional theory (DFT). Then, we study the effect of Ag on the structural and optical properties of CsPbI₂Br. Resultantly, we find that Ag-doping may not only allow partial bandgap tenability from 1.91 eV to 2.05 eV and increase photoluminescence (PL) lifetime from 0.990 ns to 1.187 ns, but also contribute to the structural stability according to the x-ray diffraction (XRD) data. Furthermore, through analysing the intermolecular interactions based on Hansen solubility parameter, the solvent engineering technique is explained in relation to the solvent trapping phenomena in the CsPbI₂Br layer. However, Ag-doping may result in pinhole-like defect morphology in films when introduced into the perovskite precursor solution via AgBr ionic compound.

5.1. Introduction

Metal halide perovskites (MHPs) are a next-generation semiconductor for electronics and optoelectronics such as emerging photovoltaics (PVs), light-emitting diodes (LEDs), field-effect transistors (FETs), photodetectors, and sensors [95,104,194-198]. MHPs have a chemical formula of ABX₃, in which A-site = organic, inorganic, or hybrid (MA, FA, Cs, or mixture); B-site = metal (Pb, Sn, or mixture); X-site = halide (Cl, Br, I, or mixture). Here, MA and FA stand for methyl ammonium (CH₃NH₃⁺) and formamidinium (HC(NH₂)₂⁺), respectively [199,200]. In 2009, Miyasaka group demonstrated for the first time that MAPbI₃ and MAPbBr₃ can serve as a visible-light sensitizer for PV cells, resulting in the power conversion efficiency (PCE) of 3.81% and 3.13%, respectively [94]. Then in 2012 and 2015, MHP solar cells reached ~10% and ~20% PCE, respectively, displaying the dramatic advancement in the PV technologies for a short period of time [201-202]. Then, currently, the certified PCE of MHP solar cells is more than ~26%, indicating that perovskite PVs is on the way to commercialization by competing with the traditional silicon PVs [203-205].

Meantime, in 2014, Snaith group compared three materials, CsPbI₃, MAPbI₃ and FAPbI₃, which have the bandgap (E_g) of 1.73 eV, 1.57 eV, and 1.48 eV, respectively, and focused on the FAPbI_yBr_{3-y} ($y= 0$ to 1) perovskite system, demonstrating the usefulness of the slightly larger FA cation as well as the tunability of bandgap [199]. Then in 2015, researchers paid serious attention to the fact that the organic-inorganic MHP solar cells have an intrinsic stability problem such as vulnerability in heat and humidity, originating from the presence of organic moieties such as MA and FA [206-207]. For example, Cahen and Hodes group compared hybrid organic-inorganic MAPbBr₃ and all-inorganic CsPbBr₃ for demonstrating that the A-site in ABX₃ structure does not have to be organic cation only for high quality PVs, paving the pathway for all-inorganic MHP solar cells with enhance stability [206]. Then, in the same year, the working all-inorganic CsPbI₃ solar cells with PCE of ~1.7-2.9% were reported for the first time by kinetically overcoming the phase instability [207]. This is because thermodynamically the most stable phase of CsPbI₃ is non-perovskite yellow orthorhombic at room temperature (RT) [208]. Then during the past decade, all-inorganic MHP solar cells have been further advanced based on the perovskite family of CsPbI₃, CsPbBr₃, CsPbIBr₂, and CsPbI₂Br [209-210]. Among these, the two extreme materials are CsPbI₃ and CsPbBr₃ because the former has high visible light-absorption but poor phase stability, whereas the latter has good phase stability but low light-absorption owing to its wide bandgap. Hence, it should be obvious to find an optimum condition between the two extremes thorough composition engineering, resulting in the many research on CsPbI₂Br with the bandgap of ~1.8-1.9 eV. Here, CsPbI₂Br shares the promising merits of MHPs such as high absorption coefficient, tunable bandgap, long exciton diffusion length, low exciton binding energy, and ambipolar transport with high mobility, resulting in PCE > 17% [211-213]. In addition, based on its specific bandgap, it can serve as a photoactive material for top-cell in the tandem structural PV cells [213].

However, CsPbI₂Br also has some disadvantageous properties such as morphological defects from fast crystallization and un-matched energetic alignment with charge transport layer [209-210]. Hence, many research groups have interest in doping engineering especially for the B-sites (i.e., Pb replacement) in the CsPbI₂Br structure [214-222]. For example, Zhu et al. reported the antimony (Sb³⁺) doping in the B-site of CsPbI₂Br, resulting in the decrease of surface defects, suppression of charge recombination, and improvement of phase stability [214]. Ma et al. demonstrated the triple improvement in film quality, radiative recombination and energy-level alignment through the zirconium (Zr⁴⁺) doping in the B-site of CsPbI₂Br [215]. Han et al. reported the improved passivation, Fermi level adjustment (n-type doping),

and crystallinity by adding calcium (Ca^{2+}) into CsPbI_2Br [216]. In the case of Zhang et al., they doped both A-/B-sites for the air-stable $\text{Cs}_{1-x}\text{Rb}_x\text{PbI}_2\text{Br}$ with guanidinium (GA^+), resulting in high crystallinity, appropriate surface morphology, favorable electronic property and reduced trap-density [217]. Guo et al. proved that niobium (Nb^{5+}) doping can increase the perovskite tolerance factor and stability the α - CsPbI_2Br phase [218]. Yang et al. reported the air-stable $\text{CsPb}_{1-x}\text{Ge}_x\text{I}_2\text{Br}$ ($x= 0.1, 0.2, \text{ and } 0.3$) perovskites by germanium (Ge^{4+}) doping, resulting in a better effective recombination lifetime and low trap densities [219]. Liu et al. doped CsPbI_2Br by indium (In^{3+}) and chlorine (Cl^-), resulting in inhibition of yellow photo-inactive phase and improvement of long-term ambient stability [220]. Duan et al. studied the lanthanide ($\text{La}^{3+}, \text{Ce}^{3+}, \text{Nd}^{3+}, \text{Sm}^{3+}, \text{Eu}^{3+}, \text{Gd}^{3+}, \text{Tb}^{3+}, \text{Ho}^{3+}, \text{Er}^{3+}, \text{Yb}^{3+}, \text{ and } \text{Lu}^{3+}$) doping into CsPbI_2Br , resulting in the increased grain size and carrier lifetimes [221]. Lau et al. reported the less toxic strontium (Sr^{2+}) doping into CsPbI_2Br , providing the passivation effect [222]. All of these clearly demonstrate that CsPbI_2Br could be an improved functional semiconductor by partially substituting the Pb^{2+} sites with other metal ions for the next-generation optoelectronic devices, motivating our works [209-210,223].

Hence, in this study, we doped CsPbI_2Br with AgBr by expecting the co-doping effects from both Ag^+ ions and Br^- ions for the first time. However, it is noteworthy that Chen et al. demonstrated the defect passivation of CsPbBr_3 with AgBr through the substitutional Ag^+ -doping on Pb^{2+} -sites [224]. However, in our case, we studied the CsPbI_2Br system containing the mixed halide, indicating that not only Ag^+ but also Br^- could serve as a dopant, affecting the properties of MHP thin film. This is because the additionally added bromine ions may compete with iodine ions when complexed with Pb^{2+} , suggesting that Br^- will act as a co-dopant with Ag^+ ions. Note that bromine ion ($D_N = 33.7$) has a higher Gutmann donor number (D_N : Lewis basicity) than iodine ion ($D_N = 28.9$) [225-226], suggesting that Br can replace I in CsPbI_2Br with high probability. First, based on the density functional theory (DFT), we calculated the silver-doping effect (the substitutional doping on the B-sites) on the electronic structure of CsPbI_2Br . Then, by adding AgBr into the perovskite precursor solution with $\text{PbI}_2:\text{AgBr} = 1: 0.01\text{-}0.03$ (molar ratio), we studied the doping effects on the optical, structural, and morphological effects. In addition, we explained the solvent-engineering mechanism [104,227] because, through this process, the trace of solvent-antisolvent was trapped during the film formation, detected by infrared (IR) spectroscopy. For this purpose, we interpret the intermolecular interaction between solvent and antisolvent based on the Hildebrand and Hansen solubility parameter [228-229].

5.2. Materials and Methods

5.2.1 Materials

Lead iodide (PbI₂, 99.99%, Sigma-Aldrich, Darmstadt, Germany), cesium bromide (CsBr, 99.9%, Sigma-Aldrich, Darmstadt, Germany), and silver bromide (AgBr, 99.99%, AR chemicals, Delhi, India), chlorobenzene (CB, ≥99.5%, AR chemicals, Delhi, India), and dimethyl sulfoxide (DMSO; 99.0%, Sigma-Aldrich) were purchased and used without further purification.

5.2.2 Methods

The perovskite precursor solutions were prepared to form CsPbI₂Br perovskite (without or with AgBr), for which the composition was controlled as follows, CsBr(PbI₂)_{1-x}(AgBr)_x with x= 0.00, 0.01, 0.02, and 0.03. Here, the control sample is as follows: CsBr (1M) and PbI₂ (1M) in 1 mL DMSO. Then, after stirring overnight at 70°C, the solutions were filtered by a polytetrafluoroethylene (PTFE) syringe filter with 0.22 μm pore size. Then 70 μl of solution was dropped on top of the glass substrate and spin-coated at 1500 rpm for 45 seconds. During spinning, after ~25 sec, 200μL CB antisolvent was dispensed on top of the wet perovskite precursor film. After spin coating, the sample was annealed thermally at 70 °C for 2 minutes and subsequently at 280°C for 10 minutes. Then all the characterizations were carried out in the air.

5.2.3 Thin Film Characterizations

The X-ray diffraction (XRD) patterns were obtained using the Drawell XRD-700 diffractometer, Tokyo, Japan) with Cu Kα (3KW) X-ray radiations ($\lambda = 1.5406 \text{ \AA}$) having a source potential of 40 kV and source current of 15 mA in the diffraction angle range between $2\theta = 10^\circ - 80^\circ$. Scanning electron microscope (SEM) images were obtained using the benchtop SEM (JCM-6000 Plus, JEOL, Japan). On the other hand, the high-resolution transmission electron microscopy (HR-TEM) images were investigated by using the model (JEM-2100, JEOL, Japan). The absorption spectra of the film were investigated by ultraviolet-visible (UV-Vis) spectroscopy (PerkinElmer Lambda 25, Kyoto, Japan) in the wavelength range of 300-800 nm. The photoluminescence (PL) lifetime curves were recorded by using the time-correlated single-photon counting (TCSPC) (model: Fluor log 3 TCSPC, Horiba, and Houston, TX, USA). The Fourier-transform infrared (FT-IR) spectroscopy data were obtained using the PerkinElmer spectrum two FT-IR spectrometer in transmittance mode from 4000 to 400 cm⁻¹. All measurements were taken at room temperature in ambient conditions.

5.2.4 Computational Method

The electronic band structures of the compounds (CsPbI₂Br and Ag-doped CsPbI₂Br) were calculated based on the density functional theory (DFT) using the Vienna Ab initio Simulation Package (VASP) software in the supercomputing resources provided by Indian Institute of Science, Bengaluru, India. The Perdew-Burke-Ernzerhof (PBE) exchange-correlation functional was used for all structural moderation. The origin software was used for sketching band structure of the perovskite film.

5.3. Results and Discussion

The projector augmented wave (PAW) method, which is included in the VASP code, was used for all DFT calculations [230]. The Perdew-Burke-Ernzerhof (PBE) exchange-correlation functional was used for all structural relaxation [231]. After optimizing the CsPbI₂Br based on the tetragonal β -CsPbI₃ crystal structure (space group P4/mbm), the lattice parameters were determined to be $a = b = 6.395 \text{ \AA}$ and $c = 5.988 \text{ \AA}$. These values are very close to Chen et al.'s reports, $a = b = 6.40 \text{ \AA}$ and $c = 5.97 \text{ \AA}$ for pseudo-cubic α -phase CsPbI₂Br [232]. Next, the $2 \times 2 \times 1$ supercells (Figure 1) were built using the optimized structure as a basis to study the electronic structures of Cs₄Pb_{4-x}Ag_xI₈Br₄ ($x = 0, 1, 2, 3,$ and 4) perovskites. Here, when $x=0$, the structure is equivalent to 4 times of the pure CsPbI₂Br perovskite as shown in Figure 1a (supercell), whereas when $x=1, 2, 3,$ or 4 , the structures become the silver doped perovskite as shown in Figure 1b. Here, note that the radius of Br⁻ is smaller than that of I⁻, which allows CsPbI₂Br to form a stable crystal structure compared to CsPbI₃. In this study, Pb-Br and Pb-I have the bond length of 2.9940 \AA and 3.1975 \AA , respectively.

According to Shannon [233], the effective ionic radius at the relevant coordination number (CN) is as follows: Cs⁺ (CN=XII) (1.88 \AA), Pb²⁺ (VI) (1.19 \AA), I⁻ (VI) (2.20 \AA), and Br⁻ (VI) (1.96 \AA). Hence, if we calculate Goldschmidt's tolerance factor, $t = (R_A + R_X) / \{\sqrt{2}(R_B + R_X)\}$, t is 0.851 for CsPbI₃, 0.855 for CsPbI₂Br, and 0.861 for CsPbBr₃, respectively. Here, $R_A, R_B,$ and R_X are the radius of A, B, and X, respectively. On the other hand, if we calculate the effective octahedral factor, $\mu = R_B / R_X$, μ is 0.541 for CsPbI₃, 0.561 for CsPbI₂Br, and 0.607 for CsPbBr₃, respectively. Note that for CsPbI₂Br, we used the average $\bar{R}_{I_2Br} = (R_{I^-} \times 2 + R_{Br^-} \times 1) / 3 = 2.12 \text{ \AA}$ for the radius of mixed halogen. Note that to be cubic phase, the perovskite should have $0.81 < t < 1.11$ and $0.44 < \mu < 0.90$ [209-210].

Note that the ionic radius of cesium is dependent on CN. For example, if cesium has CN of VI, VIII, IX, X, XI, and XII, the ionic radius is 1.67 Å, 1.74 Å, 1.78 Å, 1.81 Å, 1.85 Å, and 1.88 Å, respectively. Hence, if some literature employs CN = VI instead of XII for cesium ion, the ionic radius will be 1.67 Å. Therefore, they reported $t = 0.807$ for CsPbI₃ and $t = 0.815$ for CsPbBr₃, respectively [218]. However, Cs⁺ cation has 12-fold coordination site [234], indicating Cs⁺ (CN=XII) (1.88 Å) is correct. Importantly, material should have a tolerance factor of 0.9-1.0 to form an ideal cubic structure [235], indicating the aforementioned t values are far away from the ideal values. In other words, they can easily undergo structural deformation. Furthermore, thermodynamically, the most stable structure of CsPbI₃ is non-perovskite orthorhombic yellow delta-phase with $E_g = \sim 2.82$ eV at RT whereas that of CsPbBr₃ is orthorhombic gamma-phase with $E_g = \sim 2.3$ eV [164, 235-237]. Therefore, it should be reasonable to study CsPbI₂Br for improving the structural stability of CsPbI₃ via composition engineering (e.g., B- and X-site modification in ABX₃ structure) for solar cell applications.

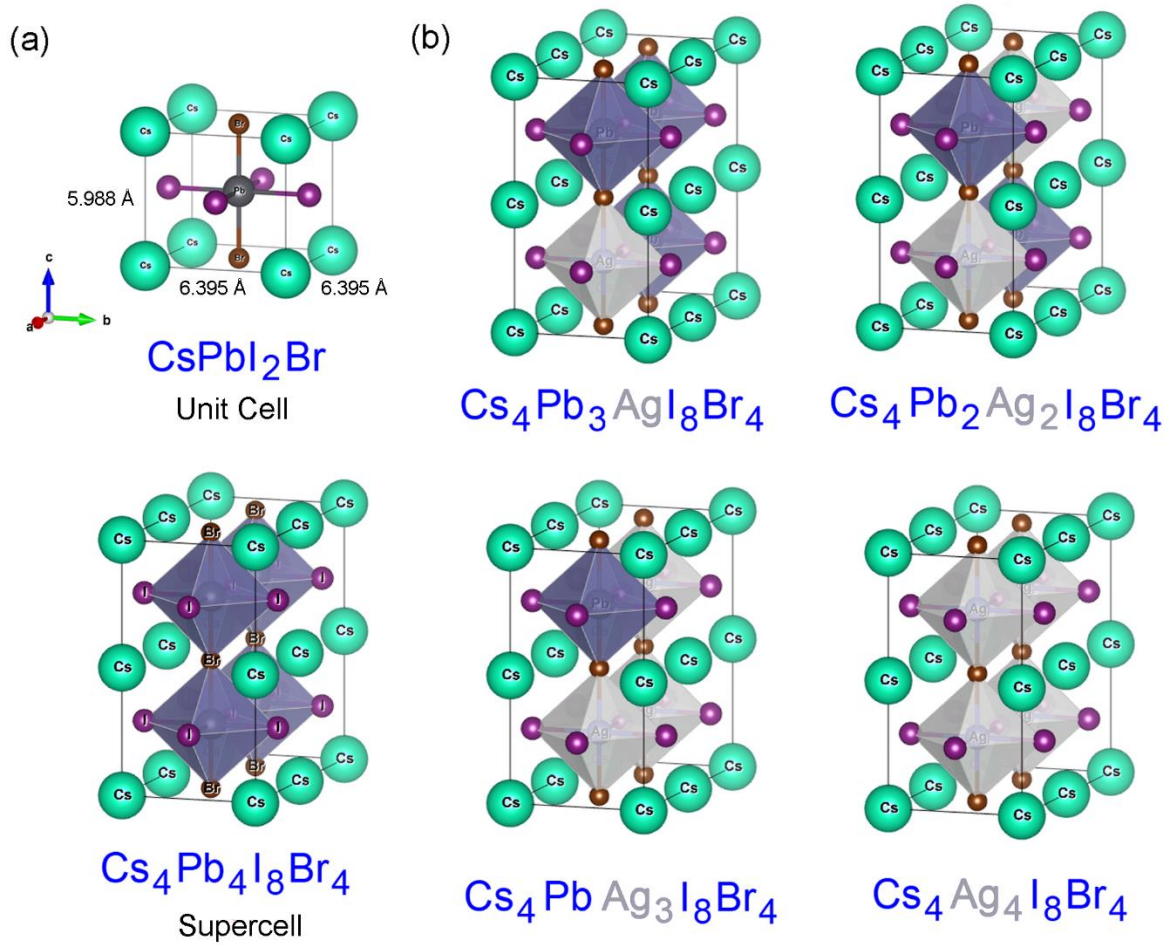


Figure 5.1 (a) Unit cell and supercell of CsPbI₂Br with lattice parameters, $a = b = 6.395 \text{ \AA}$ and $c = 5.988 \text{ \AA}$. (b) B-site doping by silver for CsPbI₂Br supercell with size of $2 \times 2 \times 1$.

Figure 5.2 shows (a-e) the electronic structures of pseudo-cubic α -phase Cs₄Pb_{4-x}Ag_xI₈Br₄, and (f) the resulting bandgap as a function of the silver doping level. Here, we assumed that the silver atom may stay with CsPbI₂Br as a substitutional dopant in line with the literature report [224]. First, except for Cs₄Pb_{4-x}Ag_xI₈Br₄ ($x = 3$), all the others display the direct bandgap characteristics. Second, although the bandgap of CsPbI₂Br is known to be $\sim 1.8\text{-}1.9 \text{ eV}$ [239-241], the DFT results exhibit that it is 1.361 eV , indicating the typical underestimation of bandgap (smaller values) [242-243]. Hence, we need to focus on the trend of bandgap. Third, when Cs₄Pb_{4-x}Ag_xI₈Br₄ ($x = 2$), the bandgap is the largest, 1.966 eV . Fourth, when Cs₄Pb_{4-x}Ag_xI₈Br₄ ($x = 4$), i.e., $4[\text{CsAgI}_2\text{Br}]$, the bandgap is the smallest, 1.060 eV . Finally, this trend of the bandgap is summarized in Figure 2f, providing the insightful silver-doping effect on the electronic structure of CsPbI₂Br qualitatively.

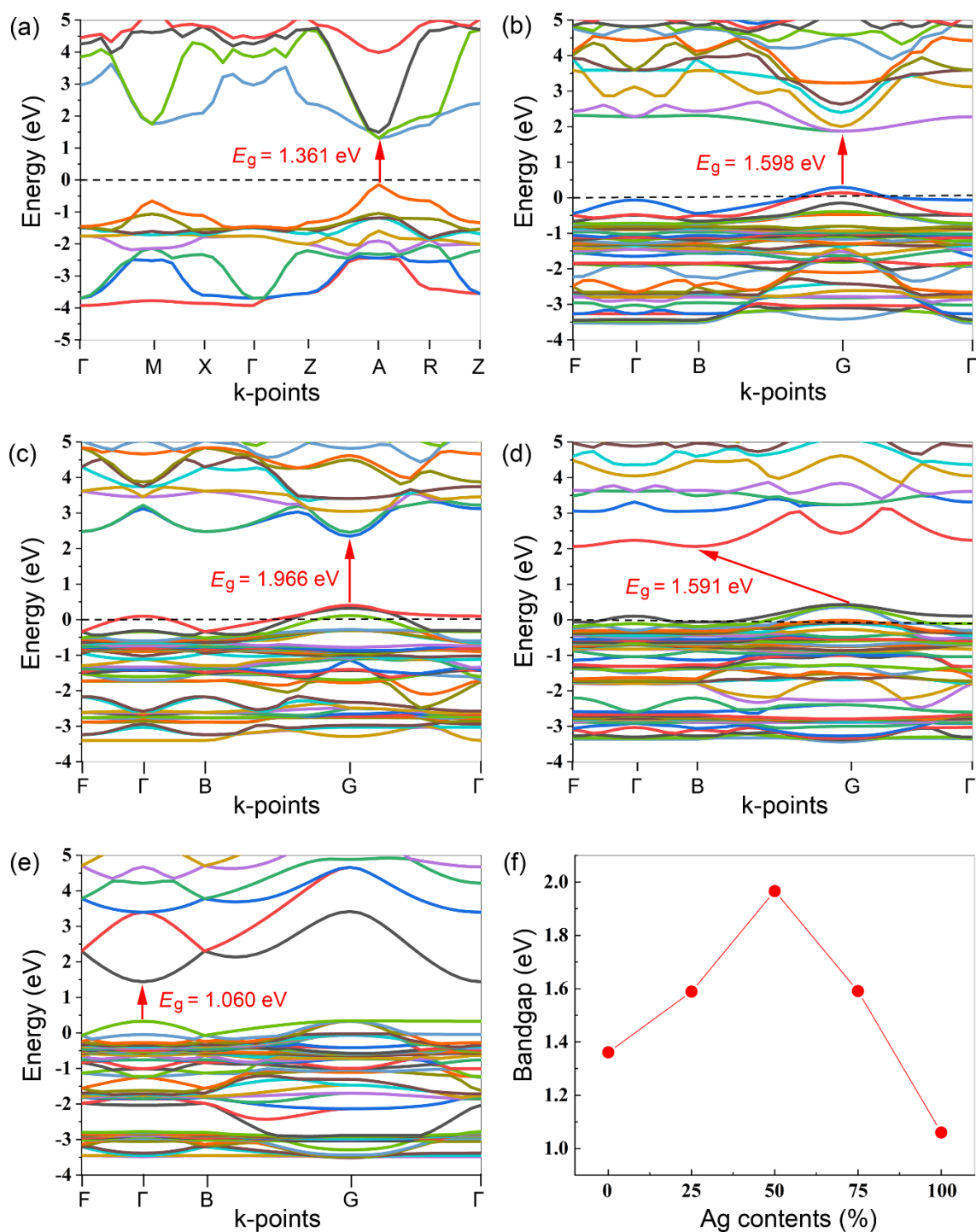


Figure 5.2 Band structure of pseudo-cubic α -phase $\text{Cs}_4\text{Pb}_{4-x}\text{Ag}_x\text{I}_8\text{Br}_4$ when (a) $x=0$, (b) $x=1$, (c) $x=2$, (d) $x=3$, and (e) Bandgap as a function of AgBr contents (%).

In this study, we introduced Ag atoms into the CsPbI_2Br crystals by dissolving AgBr compounds into the perovskite precursor solutions, indicating that there are mutual effects from both Ag^+ cations and Br^- anions. Here, in the perovskite precursor solutions, Br^- anions

can serve as a processing additive because the bromine anions have high Guttmann's donor number ($D_N = 33.7$, Lewis basicity) [225-226] affecting the crystallization of perovskites via the modified interactions between DMSO ($D_N = 29.8$) and perovskite precursors in solution state. Figure 5. 3a shows the each bandgap by optical observation, for which Tauc plot was employed as usual. First of all, CsPbI₂Br without AgBr, the bandgap is 1.84 eV, which falls in the general bandgap (~1.8-1.9 eV) of CsPbI₂Br [239-241]. Here, it is notable that CsPbI₃ and CsPbBr₃ have the bandgap of ~1.73 eV and ~2.3 eV, respectively. However when AgBr was employed in the perovskite precursor solutions, the resulting bandgap increased slightly from 1.87 eV at 1 % AgBr to 1.95 eV at 2% AgBr and 1.96 eV at 3% AgBr. Figure 5.3a shows the absorbance spectra of the perovskite film and Figure 5.3a shows the summary of the results, i.e., the bandgap as a function of AgBr-doping concentrations. Remind that the bandgap is a key factor with stability and cost for practical solar cells, determining the theoretical PCE based on the Shockley-Queisser limit [244]. Importantly, Ravi et al. pointed out that in CsPbX₃ perovskite, the conduction band minimum (CBM) is dominantly affected by Pb 6p whereas the valence band maximum (VBM) is mainly determined by anti-bonding hybridization Pb 6s and X np orbitals, specifically, the major effect from X np [245]. Therefore, the bandgap shift in Figure 5.4 could be explained as follows. Ag-doping may affect CBM-shift whereas Br-codoping may contribute to VBM-shift although these effects will be small-scale because of the amounts (~1-3%) of AgBr-doping concentration. Then, we measured the PL lifetime for the CsPbI₂Br when AgBr was 0, 1, 2, and 3 %. Accordingly, as shown in Figure 5.5, the PL lifetime was enhanced from 0.990 ns (0% AgBr) to 1.187 ns (3% AgBr) with increasing AgBr amounts, suggesting that the AgBr doping helps minimizing the nonradiative transition according to the many literature reports (e.g., the defect passivation by B-site doping) [214-222, 224].

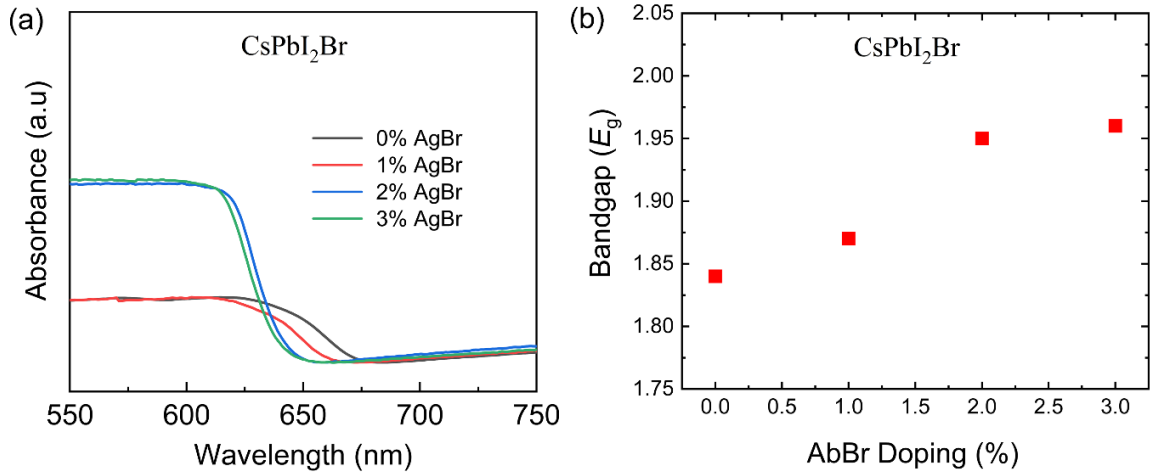


Figure 5.3 (a) UV-Vis spectra of CsPbI₂Br as a function of AgBr concentration. (b) Bandgap as a function of AgBr doping concentration (%).

Optical bandgap determination for CsPbI₂Br as a function of AgBr concentration by Tauc plot.

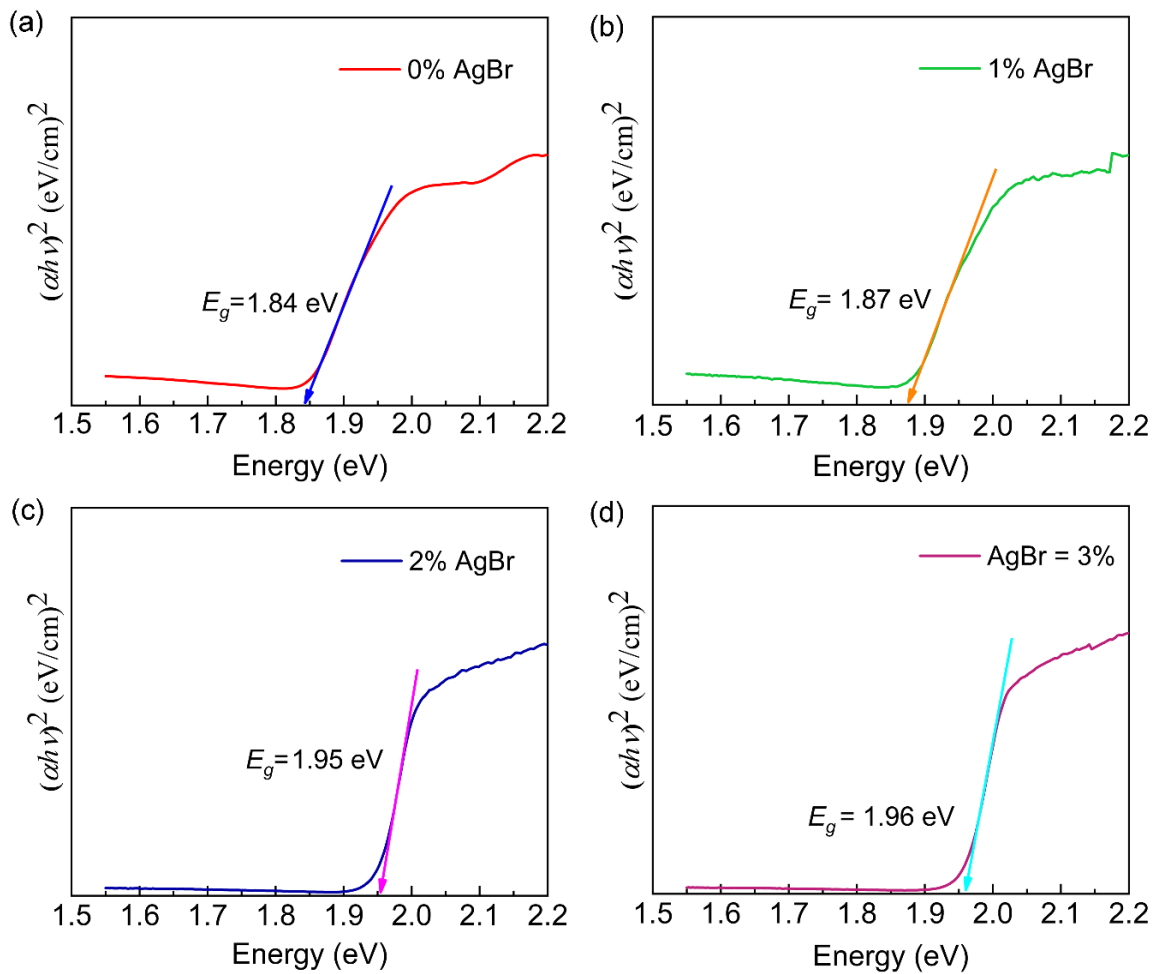


Figure 5.4 Optical bandgap determination for CsPbI₂Br as a function of AgBr concentration by Tauc plot.

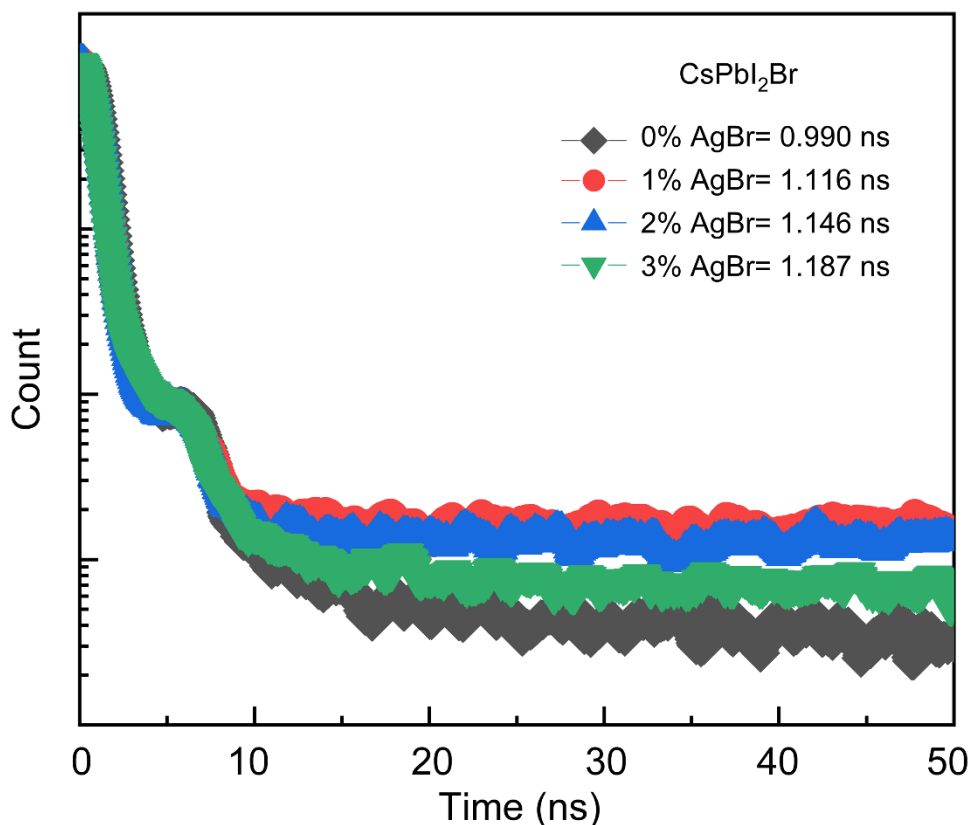


Figure 5.5 PL lifetime of CsPbI₂Br thin film as a function of AgBr concentration.

Then we examined the FT-IR spectra for the CsPbI₂Br thin film as a function of AgBr doping level in the perovskite precursor solutions. As shown in Figure 6a, we can find only the FT-IR peaks from the solvents remaining inside of the CsPbI₂Br thin film. This observation indicates that the trace amounts of solvent molecules may survive in the trapped state inside of the perovskite film although the annealing temperature (> 250 °C) was higher than the boiling points of solvents (DMSO: 189 °C and CB: 132 °C; structures are in Figure 5.6b). Here, the detailed peak assignment is as follows [246]: First, in the high-frequency regions, 3025-2849 cm⁻¹, =C-H and -C-H vibration were observed from DMSO and CB molecules inside of the CsPbI₂Br crystals. At 1676 cm⁻¹, -C=C vibration from the aromatic ring of CB was detected. On the other hand, at 1387 cm⁻¹, 1092 cm⁻¹ and 738 cm⁻¹, -CH₃, S=O and -C-Cl vibration were displayed, respectively. Finally, the small peak at 463 cm⁻¹ is ascribed to the molecular vibration of the antisolvent CB.

Importantly, through Figure 5.6c, we may explain the solvent engineering [227] process related to the solvent trapping phenomena. Here, the solvent engineering procedure is as follows. The antisolvent (chlorobenzene) dripping on top of the wet perovskite precursor film (solvent: DMSO) during spinning results in the fast crystallization and deposition of a

perovskite film. Here, for understanding the intermolecular interactions, the solubility parameter (δ) data [228] of solvent, antisolvent, and perovskite are needed. First, DMSO and CB have $\delta = 14.5$ (cal/cm³)² and $\delta = 9.5$ (cal/cm³)², respectively [247]. In the case of CsPbI₂Br, we may estimate it from the water contact angle ($\theta_c = 32.76^\circ$) data reported by Chen and co-workers [248]. Li and Neumann [249] suggested the relation between contact angle and surface energy, $\cos \theta_c = -1 + 2\sqrt{\gamma_{sv}/\gamma_{lv}} \cdot \exp[-\bar{\beta}(\gamma_{lv} - \gamma_{sv})^2]$, where γ_{lv} , γ_{sv} , and γ_{sl} are surface energies for liquid-vapour, solid-vapour, and solid-liquid, respectively. The constant $\bar{\beta}$ is 0.000115 m⁴/mJ² and γ_{lv} is 72.8 mJ/m² for water, respectively. Then, by inputting $\theta_c = 32.76^\circ$, we may estimate $\gamma_{sv} = 63.05$ mJ/m². Then, from the relation of $\delta[(\text{cal/cm}^3)^2] = 1.829058\sqrt{\gamma_{sv}}$ [250-251], we obtained $\delta = 14.5$ (cal/cm³)² or $\delta'(\text{SI unit}) = \delta \times 2.0455 = 29.7$ MPa^{1/2}, respectively (Table 1). Hence, because CsPbI₂Br and DMSO have the same solubility parameter, there is a high probability that DMSO may be trapped in the CsPbI₂Br. However, in the case of CB, the two solvent-antisolvent (CB and DMSO) molecules are miscible because of the entropy-driven mixing, affording CB to wash DMSO during its dripping process. However, when CB was dropped on top of the wet perovskite precursor film, CB might be also trapped into the crystal structure of CsPbI₂Br although CB and CsPbI₂Br have two different polarity, i.e., CB is slightly polar (polarity index = 2.7) but CsPbI₂Br and DMSO (polarity index = 7.2) are highly polar [252]. Hence, CB's trapping could be understood based on the physical trap instead of mutual affinity between CB and CsPbI₂Br. On the other hand, DMSO can be trapped by two reasons, both affinity and physical confinement. Accordingly, even after thermal annealing at 280°, the trace amounts of solvents could be still trapped according to the FT-IR spectra in Figure 5.6a.

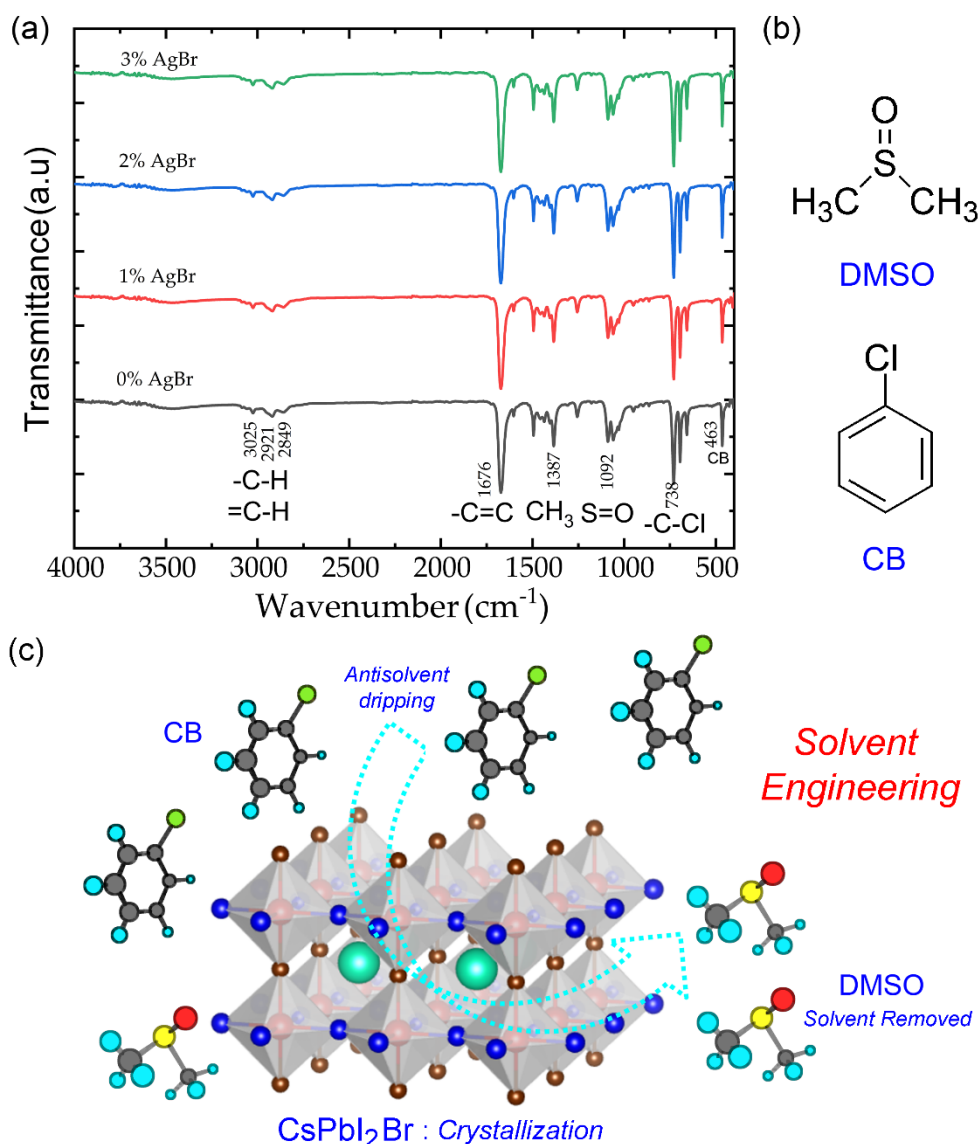


Figure 5.6 (a) FT-IR spectra of CsPbI₂Br with or without AgBr when processed with dimethyl sulfoxide (DMSO) and chlorobenzene (CB). (b) Chemical structures of DMSO and CB. (c) Solvent engineering process.

When CB is dripping on top of the wet perovskite (precursor) film, DMSO can be washed away. During this process, some solvent molecules could be trapped in the perovskite thin film.

Table 5.1 Solubility parameter, molecular weight, density, and molar volume of solvent, non-solvent, CsPbI₂Br. δ' (SI unit) = $\delta \times 2.0455$.

Chemical	δ' (MPa ^{1/2})	δ [(cal/cm ³) ²]	MW (g/mol)	ρ (g/cm ³)	\hat{v}_i (cm ³ /mol)
DMSO	29.7	14.5	78.13	1.10	71.03
CB	19.4	9.5	112.56	1.11	101.41
CsPbI ₂ Br	29.7	14.5	673.82	4.79 ^a	140.67

^a this is estimated based on the lattice parameters, $\mathbf{a}=\mathbf{b}$ = 0.640 nm and \mathbf{c} = 0.597 nm.

Figure 5.7a shows the XRD patterns of CsPbI₂Br as a function of AgBr doping concentration. First, in the absence of AgBr, the CsPbI₂Br perovskite thin film displays the typical (100) and (200) peaks [253]. However, by increasing AgBr concentration (see ~2-3% AgBr), the other peaks such as (211), (300) and (222) are intensified, indicating that the crystallographic ordering decreases with increasing AgBr concentrations. This observation implies that the crystallization kinetics was changed when AgBr was introduced into the perovskite precursor solutions. Second, we estimated the crystallite size (*D*) by using Scherrer's relation of $D = 0.9\lambda / (B \cdot \cos \theta)$, where λ (= 0.154 nm) is the wavelength of x-ray whereas *B* is the full-width-at-half-maximum (FWHM) at the diffraction angle θ . The results are summarized in Figure 7b and Table 2. As shown in Figure 7b, there is no clear linear trend when AgBr was introduced into the perovskite precursor, implying that although the morphology might be changed through different crystallization kinetics, the crystallite size (i.e., the average single crystalline domains in the polycrystalline structure) is not much changed but similar to all the condition whether doped or not.

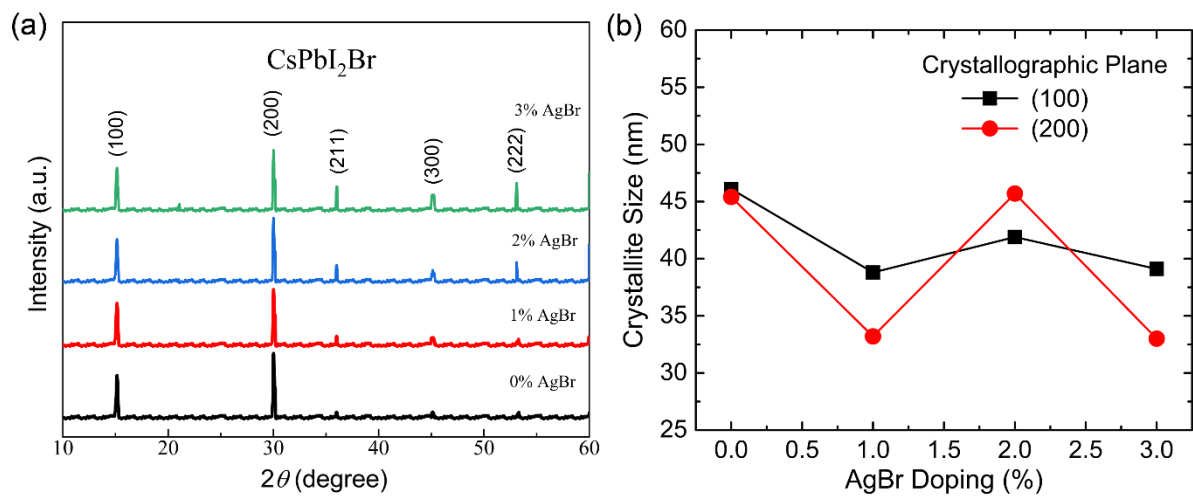


Figure 5.7 CsPbI₂Br as a function of AgBr doping: (a) XRD patterns and (b) crystallite size.

Table 5.2 Crystallite size in CsPbI₂Br as a function of AgBr doping concentration.

Plane	AgBr (%)	2 θ (°)	<i>B</i> (rad)	<i>D</i> (nm)
(100)	0	15	0.003036	46.1
	1	15	0.003601	38.8
	2	15	0.003334	41.9
	3	15	0.003573	39.1
(200)	0	30	0.003640	45.4
	1	30	0.004319	33.2
	2	30	0.003140	45.7
	3	30	0.004347	33.0

Figures 5.8 a and b shows the stability test of the perovskite thin-film, (a) CsPbI₂Br without AgBr and (b) CsPbI₂Br with 1% AgBr doping. These two samples were selected for this test because the surface morphology is relatively uniform than the others (~2-3 % AgBr doped perovskite samples). Interestingly, the both samples show the growing of the minor peaks at (211) and (222) crystallographic planes with time, indicating that the orientational ordering decreases with time. Here, it is notable that except for single crystalline perovskite thin films, all the polycrystalline films are thermodynamically metastable because the defect area (including polycrystalline nature) makes the surface energy increase. Hence, for lowering the Gibbs free energy, the sample can undergo phase transition. In this case, by decreasing the orientational order (i.e., increasing (211)-(222) XRD peaks), the film may reduce its free energy. Furthermore, when we see the CsPbI₂Br sample without AgBr-doping in Figure 8a, compared to the same sample (but different batch) in Figure 5.7 (black solid line), the additional strong peak at (300) crystallographic plane was observed [i.e., more orientational order because the (100), (200) and (300) planes are equivalent], indicating the batch-to-batch partial uncertainty depending on the drying process in the laboratory under ambient conditions. Importantly, 1% AgBr doped CsPbI₂Br shows structural stability (i.e., the XRD peak position is the same with aging time), but 0% AgBr sample shows clearly the major peak's shift to the left direction (i.e., a partial expansion of crystal; see the dotted red-line box in Figure 8a). This aging-effect data proves that the AgBr doping should contribute to the structural stability of CsPbI₂Br perovskite films. The results are reasonable because AgBr addition increases stability (wider bandgap and improved tolerance to environments)

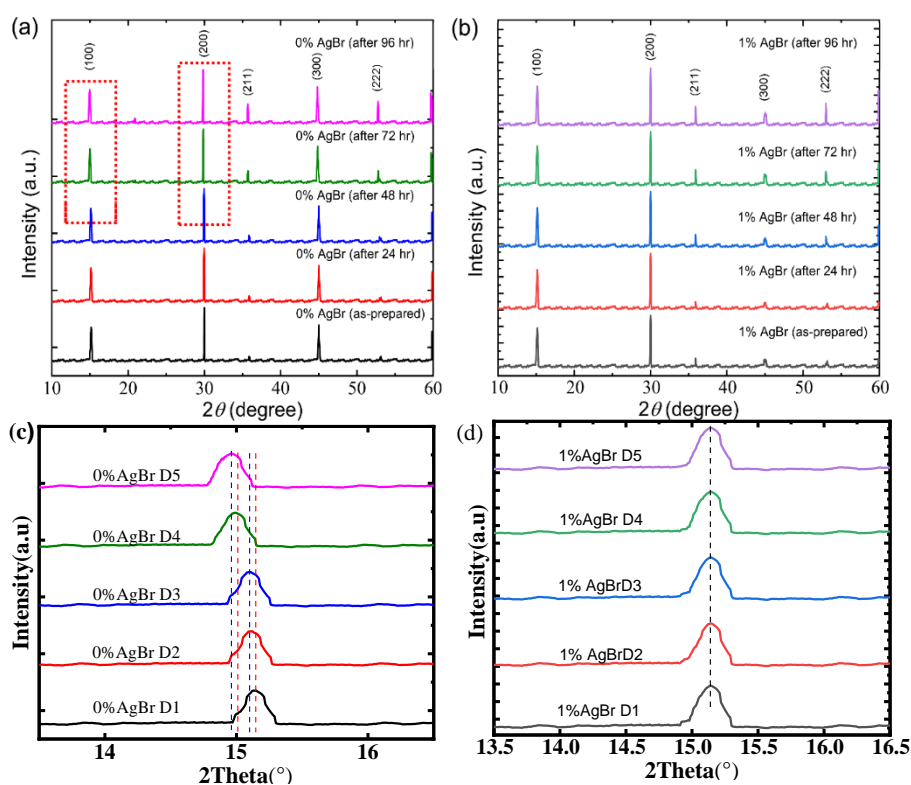


Figure 5.8 Structural stability test by XRD: (a)&(c) CsPbI₂Br without AgBr and (b)&(d) CsPbI₂Br with 1% AgBr.

Figure 5.9 shows the SEM images displaying the microstructural morphologies of the CsPbI₂Br sample as a function of AgBr doping concentration. First, the CsPbI₂Br thin films [(a) without AgBr and (b) with 1% AgBr] are relatively uniform whereas the other films [with ~2-3% AgBr] are non-uniform by displaying the crystal domains and defect sites. Probably, the samples (Figure 5.9 c and d) were grown very fast (or fast aggregate) in the presence of high doping (~2-3% AgBr). However, remind that according to XRD data in Figure 5.7, the crystallite size is not much different from sample to sample depending on the AgBr doping. The average crystallite size is 41.5 ± 3.4 nm and 39.3 ± 7.2 nm at (100) and (200) crystallographic planes, respectively. However, as shown in Figure 5.9, the film processing condition should be improved further in future. Finally, we examined the drop cast CsPbI₂Br sample on the TEM copper grid without any annealing process (Figures 5.10a-c). Also Figure 10d displays the selected area electron diffraction (SAED) pattern of CsPbI₂Br displaying the phase impurity, which is different from the XRD pattern in Figures 5.7a and 5.8, indicating that without annealing (> 250 °C), the sample has high phase impurity, e.g., non-perovskite yellow phase (see Table 5.3 containing estimated 2θ date for

comparison purpose). Hence, the pseudo-cubic α -phase CsPbI_2Br with ‘iodine atoms’ might be kinetically stable (not thermodynamically) due to polymorphism [208,234], although the kinetics should be further investigated from the viewpoint of stability in future. Therefore, ‘iodine’ has double sides, increasing light absorption but causing stability problems under ambient conditions.

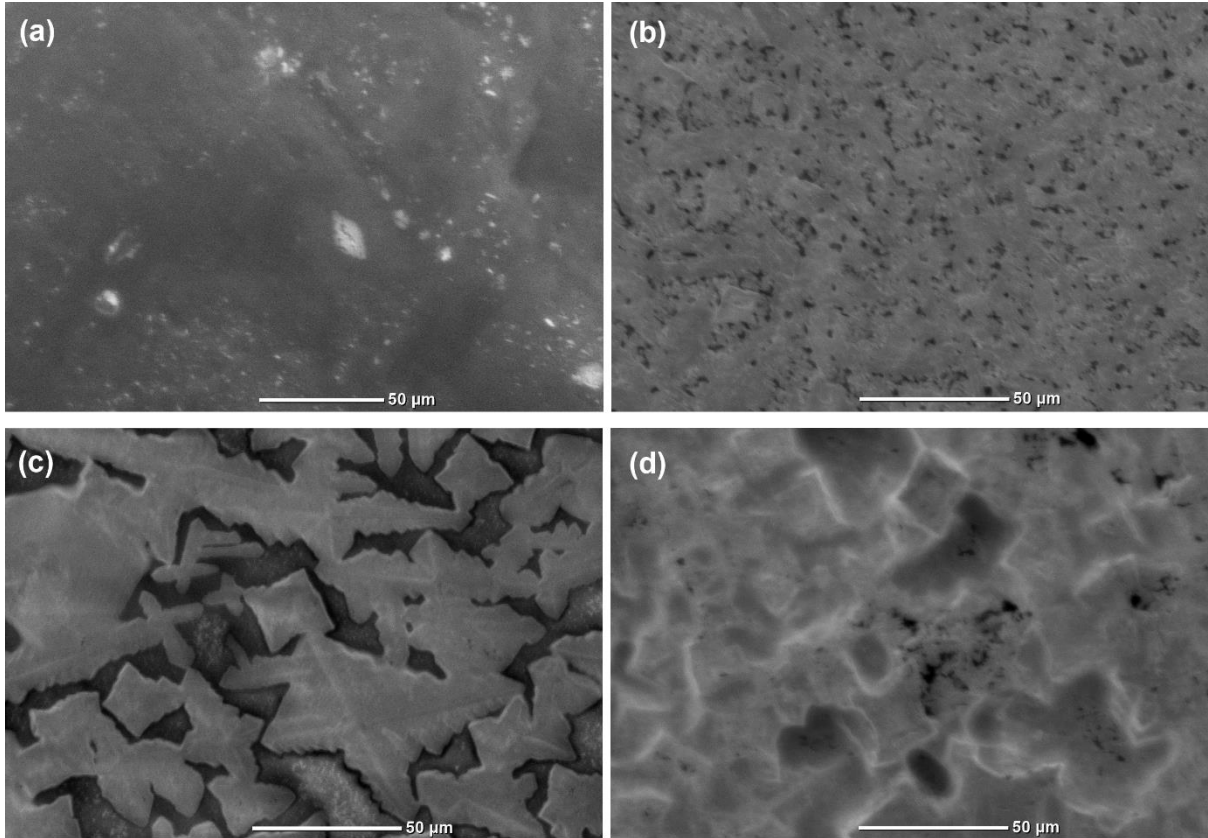


Figure 5.9 SEM images: (a) CsPbI_2Br without AgBr, (b) CsPbI_2Br with 1% AgBr (c) CsPbI_2Br with 2% AgBr, and (d) CsPbI_2Br with 3% AgBr.

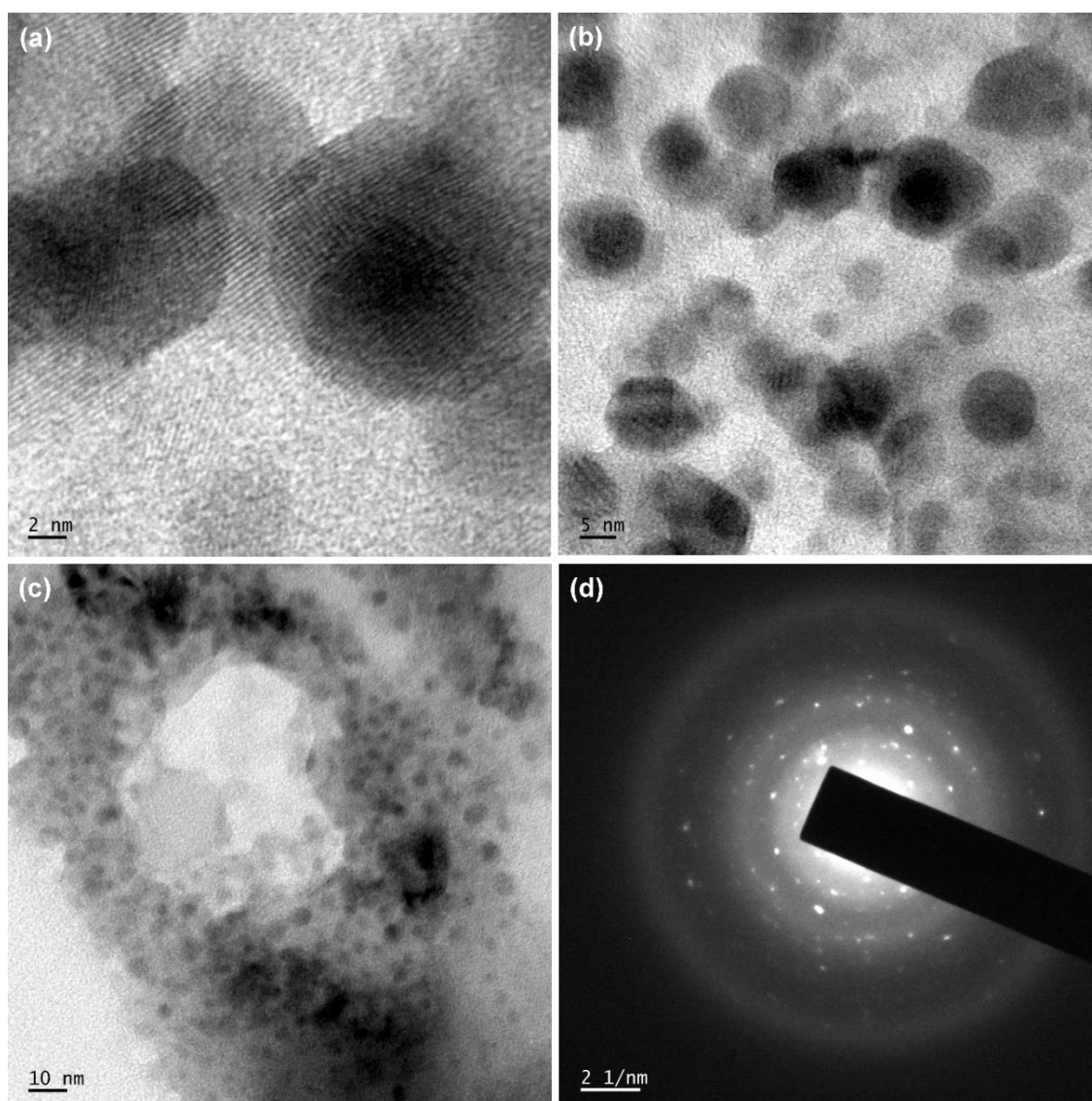


Figure 5.10 HR-TEM image of CsPbI₂Br with different scale bar: (a) 2 nm, (b) 5 nm, and (c) 10 nm. (d) Selected area electron diffraction (SAED) pattern of CsPbI₂Br displaying the phase impurity at room temperature.

Table 5.3 Analysis of SAED image for CsPbI₂Br without annealing at room temperature.

Perovskite	Diameter (1/nm)	Radius (1/nm)	<i>d</i> -Spacing (nm)	2 θ (°)
CsPbI ₂ Br	3.91	1.96	0.51	17.3
	5.23	2.63	0.38	23.2
	6.32	3.16	0.32	28.2
	8.05	4.03	0.25	36.1
	10.08	5.04	0.20	45.7
	12.10	6.05	0.17	55.5

5.4. Conclusions

CsPbI₂Br is an interesting light-harvesting semiconductor for next generation, displaying the bandgap of ~1.84-1.96 eV and the improved stability compared to CsPbI₃. First, we demonstrated that it was possible to tune the bandgap of CsPbI₂Br by substituting the lead atoms by silvers based on the DFT calculation. Here, the bandgap reached the maximum by substituting the half of Pb by Ag. Second, when we added AgBr into the perovskite precursor solution from 1% to 3% vs. PbI₂, the bandgap increased monotonically from ~1.87 eV to ~1.96 eV, which is in line with the trend predicted by DFT calculation. Third, the PL lifetime was enhanced by employing AgBr into the perovskite precursor solution, e.g., from 0.990 ns (CsPbI₂Br without AgBr) to 1.187 ns (CsPbI₂Br with 3% AgBr). Fourth, the FT-IR spectra showed that the solvents (DMSO and CB) were trapped inside of the CsPbI₂Br-AgBr (0-3%) thin films based on the physical trap and/or affinity. Fifth, the XRD patterns displayed the strong (100) and (200) peaks, but when AgBr was introduced (or time increased), the minor peaks at (211) and (222) crystallographic planes were partially enhanced, indicating that the orientational order was diminished by AgBr doping and/or time passing. Sixth, when AgBr was introduced into the film, the crystallization process was changed, affecting the morphologies of films according to the SEM data. Seventh, based on the XRD data, AgBr doping contributed to the structural stability of CsPbI₂Br perovskite films. Finally, considering the golden triangle (efficiency-stability-cost) of solar cells, some innovative ideas should be further required to secure the stability of all-inorganic perovskite (CsPbI₂Br) thin film as a next-generation semiconductor for optoelectronics.

Chapter Six

6. Facile Improvements of mixed Cesium lead halide ($\text{CsPbI}_{2.93}\text{Br}_{0.07}$) Perovskite Thin Film, The Effect of Antisolvent Treatment on Photo physical Property

Abstract: All-inorganic CsPbI_3 perovskite films have just gotten pronounced attention having to their skyrocketed photosensitive properties, and higher chemical stability. The cubic phase creation with high temperature and phase shift to orthorhombic phase in ambient conditions, all inorganic Cesium lead triiodide (CsPbI_3) lags far from the organic and organic-inorganic photovoltaic application by its performance and device stability. Also, the poor phase stability and degradable surface morphology are observed defects of the CsPbI_3 perovskite film. Among the mechanisms to improve Cesium lead triiodide perovskite thin films, composition engineering is the first method due to its simple mechanisms and between halogen participations. In this demonstration, we examined the mixed precursor of the perovskite with a small concentration ratio of CsBr to CsI (CsBr: CsI, 5%: 95%) and treated it with mixed antisolvents (mixture of Toluene and ethyl acetate, & Chlorobenzene and ethyl acetate). The result showed that 5% CsBr mixed CsPbI_2 perovskite film treated with mixed antisolvents toluene& and ethyl acetate (TEA) had good absorbance spectra, high photoluminescence intensity, great thermal stability, large crystal sizes, and smooth surface morphology, pinhole-free and minimized voids when compared to control film treated with mixed antisolvent toluene& and ethyl acetate (TEA). The result indicated that the halide perovskite film treated with mixed antisolvent was a good active layer for photovoltaic devices.

6.1 Introduction

6.1.1 Background of the Study

The growth of cesium lead halide perovskite photovoltaics is a major focus of the energy conservation community today. The cubic phase formation requires high annealing temperature and phase change to optically inactive phase in ambient condition, all inorganic cesium lead triiodide (CsPbI_3) lags behind organic and organic-inorganic light absorbing materials due to air instability. Various approaches to overcome air instability issues of the Cesium lead triiodide perovskite layer, such as metal ion doping with lead ion, antisolvent dripping, additive engineering, and halide exchange and sharing [252-255]. Among halide-

sharing mechanisms, mixing a small amount of cesium bromide with cesium iodide in CsPbI₃ films of perovskite films of precursor was the best technique to improve the enactment of the perovskite film by developing the morphology of the film. Only iodine-doped CsPbI₃ perovskite is used to reduce the energy band gap [256-257] which helped the film to non-radiative recombination centres. In contrast, bromine-doped perovskite is used to enhance stability, and maintain consistent performance [258-259], and requires less annealing temperature for better film formation compared to only iodine-doped. Also, fractional replacement of I with Br ion can stabilize the a-phase of perovskite films [260].

The mixture of CsBr & CsI with PbI₂ makes the CsPbI₂Br perovskite layer have a band gap of 1.93 eV [261-262] and extraordinary potential used to improve power conversion efficiency enhancement, resist moisture, requires less amount of temperature to film formation, improve the quality of the crystal,[21,41] to form cubic phase at low annealing temperature, to produce micro-strain in perovskite phase, to minimize tramp density[263-267] improve the surface of the film harmonize the small scale structural and photosensitive possessions of the mixed perovskite film. Mixed halides make perovskites with high compositional elasticity and photosensitive performance, and also improve perovskite solar cell stability. CsI and CsBr have formed negative energy because they are thermodynamically stable [268-272]. In this work, we mixed 5% of CsBr in the CsPbI_{2.93} precursor of the perovskite film with a small concentration in the following expression.

$CsBr_{0.07} + CsPbI_{2.93} \leftrightarrow CsPbI_{2.93}Br_{0.07}$. Nevertheless, the mixing of Br increased a bandgap to large (1.93–2.03 eV) compared to 1.73 eV that of CsPbI₃ [82,273]. Therefore after mixing with 5% of CsBr, we treated with two mixed antisolvents such that 50% each toluene& ethyl acetate (TEA), and Chlorobenzene & ethyl acetate (CBEA) to produce a good bandgap active layer for photovoltaics [274].

Antisolvent increases the number of nuclei during film formation, which consequences in a more uniform and voidless perovskite film. This in turn, leads to improved photovoltaic performance, lower hostesses, and greater stability [273]. The combination of anti-solvents has a critical effect on the formation of perovskite for light absorption uses. To governor the perovskite nucleation and particle growing rate for realizing excellent performances perovskite film, an solvent stabilizer is typically hosted into the single-step process [275] Compared with the single antisolvent treatment, the mixed antisolvent is that they combine the advantages of two solvents and a better extraction effect can be reached by regulating the

mixing ratio of different antisolvent [276]. The thermal stability of mixed antisolvent (For example the mixture of toluene and Ethyl acetate) is better than that of single antisolvent (Ethyl acetate). The amount of antisolvent dissolved in the mixed solution is less than the sum of the amounts for the individual solvents. In this case, ethyl acetate has higher polarity and higher dipole moment mixed with Toluene and CB; therefore green antisolvent minimized the toxicity of other antisolvents [277]. The green antisolvents afford smooth, compact, low-defect, and full-coverage perovskite films, comparable to the typical halogenated antisolvent-processed perovskite films. The green antisolvent also demonstrated promising PCEs of 13.46%, CsPbI₂Br, based PSCs [278].

This work demonstrates the high importance of green antisolvents as a universal method to obtaining good performance perovskite films for fabricating high-efficiency PSCs. The mixed antisolvents dripping technique in CsPbI₃ perovskite film is one of the greatest ways for solvent industries to progress the superficial of light-absorbing layer of film and to enhance the enactment of the solar cell [279]. The investigated mixed antisolvents with equal ratios of concentration to improve stability and PCE of perovskite photovoltaics shown from different scholars work such that mixture of toluene and diethyl ether (T&DEE), methyl acetate, and chloroform [280-281]. The mixture of toluene and chlorobenzene (T & CB), chlorobenzene and diethyl ether (CB & DEE) are some of the investigated mixed antisolvents aimed at improving the stability and performance of photovoltaic nanotechnology [282-283]. The antisolvent treatment methods distended perovskite particle sizes and passivized particle restrictions [284].

The solubility of the inorganic halides in the antisolvent and the miscibility of the solvent stabilizer with the dimethyl formamide (DMF)/ dimethyl sulfoxide (DMSO) in the precursor of perovskite are the main two categories points of antisolvents [285]. The configuration of the perovskite precursor, the property of antisolvents, and the dripped time and the annealing temperature of spin coating of antisolvents are the main factors when the perovskite film is treated by antisolvent engineering [234]. The different experimental results showed that the spectral absorption, the photoluminescence intensity, the energy band gap, the crystal size, and the surface morphology of CsBr mixed perovskite film were improved compared with the controlled film.

6.2. Materials and Methods

6.2.1 Materials

Materials and chemicals used for this experimental work are Cesium iodide (CsI, 99.99%, Sigma-Aldrich, Darmstadt, Germany), Cesium bromide (CsBr, 99.9%, Sigma-Aldrich, Darmstadt, Germany), Lead iodide (PbI₂, 99.99%, Sigma-Aldrich, Darmstadt, Germany), Dimethyl formamide (DMF, 99.5%, AR chemicals, Delhi, India), Dimethyl sulfoxide (DMSO, 99%, Sigma-Aldrich), ITO glass, Toluene (≥99.5%, AR chemicals, Delhi, India), Chlorobenzene (CB, ≥99.5%, AR chemicals, Delhi, India), and Ethyl acetate (99%, grade LR, model SYMAX). The purchased chemicals and solvents were used without further purification.

6.2.2 Methods

0.4mmol CsI and 0.4mmol PbI₂ were added to the mixture of 1.6 mL dimethyl formamide (DMF) and 0.4 mL dimethyl sulfoxide (DMSO) with a fraction of (4:1) in line with and then stirred for 3hr at room temperature and cooled at room temperature [287]. For the mixed halide case 0.4mmol PbI₂, 0.3998 mmol CsI, and 0.0002 mmol CsBr (95%: 5%) were added to the mixture of 1.6 mL DMF and 0.4 mL DMSO with a ratio of (4:1) in line with and then stirred for 3hr at room temperature and cooled at room temperature. Then, the solution was filtered by a polytetrafluoroethylene (PTFE) syringe filter with 0.22 μm pore size and 80 μl of precursor solutions drop on indium thin oxide glass substrate while spin coating by single-step spin coating method with a rotation speed of 4000 RPM for 40 seconds. At the end of the 35th second, about 250 μl equal ratios of antisolvents are proud of using a 1000 μl pipette. The ratios of antisolvents to precursor solutions are about 3:1. The ratio of mixed antisolvents was taken as 50% each, toluene and Ethyl acetate (T: EA, 1:1), and chlorobenzene and ethyl acetate (CB: EA, 1:1)). After spin coating, the film sample was annealed on a hotplate 120°C for 10 minutes in a dark area and characterization conducted in air condition. For the geometry optimization, the energy, maximum force, maximum displacement, and maximum stress were 5×10^{-5} eV/atom, 0.01 eV/Å, 5×10^{-4} Å, and 0.02 GPa, respectively.

6.2.3 Characterization

The particle size and arrangement of the CsPbI₃ and CsBr mixed with different concentrations of CsPbI₃ film were performed by X-ray diffraction (XRD) (model: the Drawell XRD-700 diffract meter, Tokyo, Japan) with Cu Kα (3KW) X-ray radiations ($\lambda = 1.5406$ Å) having a source potential of 40 kV and source current of 15 mA in the diffraction angle range between $2\theta = 10^\circ - 80^\circ$. The microstructure image of the CsPbI₃ and CsPbI₃

mixed with different concentrations of CsBr was investigated by Field emission scanning electron microscopy (FE-SEM, Carl ZEISS microscopy, MAIA3 XMH (model 2016) 119-0025, Germany), High-resolution transmission electron microscopy (HRTEM, Model: JEOL, JEM-2100). Also, the film's surface morphology with/without CsBr was studied by AFM atomic force microscope (AFM, model Park NX10). The engagement spectra of the film were investigated by ultraviolet-visible spectroscopy (PerkinElmer Lambda 25, Kyoto, Japan) in the wavelength range of 300-800 nm. The FTIR measurements were performed with a PerkinElmer spectrum two FTIR spectrometer in transmittance mode from 400 to 4000 cm^{-1} with a resolution of 4 cm^{-1} . All demonstrations were taken at room temperature in air condition.

6.3. Results and Discussion

6.3.1 The structures and properties of solvent and antisolvents

Figure 6.1 shows the chemical structure of antisolvents, (a) Toluene, (b) chlorobenzene, and (c) Ethyl acetate. Here from Table 6.1, we understand that Toluene and chlorobenzene are structured without oxygen while green antisolvent ethyl acetate contains oxygen in its structure. Ethyl acetate has a higher polarity index and dipole moment than toluene (polar) and chlorobenzene (non-polar). Figure 6.1 shows the combination of having less polarity indexed and less dipole moment antisolvents (Toluene and chlorobenzene) with having higher polarity and higher dipole moment antisolvent, Ethyl acetate. Toluene and chlorobenzene are immiscible and miscible anti-solvents with host solvents respectively.

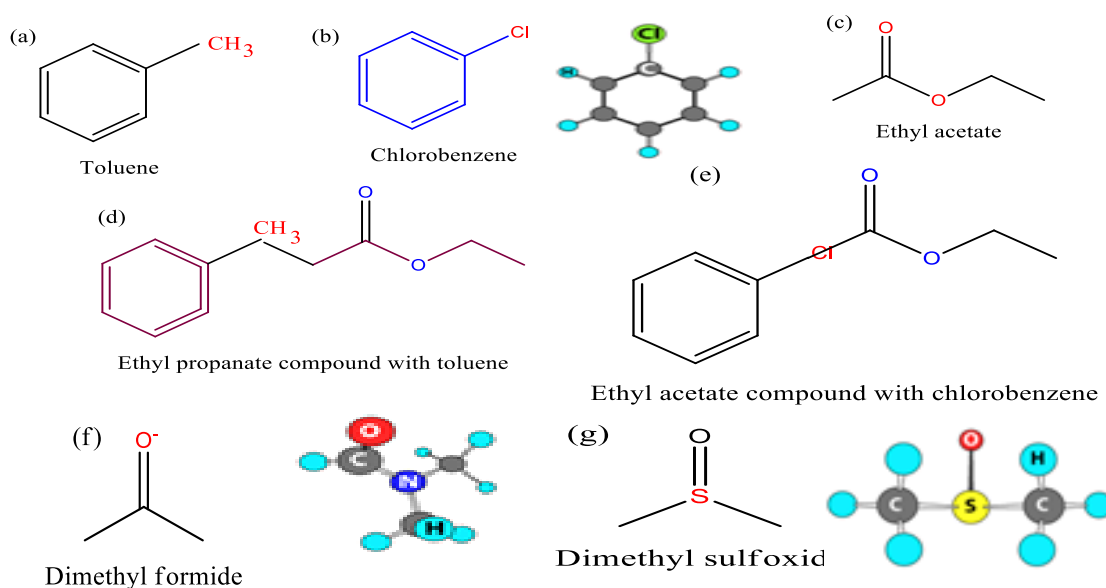


Figure 6.1 The chemical structure of antisolvents and solvents. (a) Toluene, (b) Chlorobenzene, and (c) Ethyl acetate (d) mixed antisolvents Toluene & Ethyl acetate (TEA) (e) mixed antisolvents Chlorobenzene & Ethyl acetate (f) DMF (g) DMSO.

From the previous work we showed that the Guttmann's Donor number of DMF, DMSO & CB are 26.8, 29.6 and 3.3 Kcal/mole respectively [274].

Table 6.1 Polarity index and boiling point of antisolvents

Antisolvents	Polarity index	Boiling point (°C)	Dipole moment	Chemical Formula
Toluene	2.4	110.6	0.36 D	C ₆ H ₅ CH ₃
Chlorobenzene	2.7	132.0	1.50 D	C ₆ H ₅ Cl
Ethyl acetate	4.4	77.1	1.88 D	C ₄ H ₈ O ₂

6.3.2 Optical Result and Discussion

Figure 6.3 presents several scientific findings regarding the analysis of controlled (CsPbI₃) and 5% CsBr mixed with CsPbI₃ perovskite films. Subfigure (a) illustrates the Uv-vis absorbance spectra, where it is observed that the CsPbI₃ film treated with TEA experienced an increase in absorbance, while treatment with CBEA resulted in a slight decrease. This suggests that TEA is a more effective antisolvent than CBEA. Additionally, the controlled film and the film mixed with 5% CsBr exhibit similar absorption edges, indicating that an insignificant quantity of bromine to iodide does not suggestively impact the absorption stuff of the perovskite films. The absorption range for pure CsPbI₃ mixed with 5% CsBr and treated with antisolvents TEA& CBEA was observed to be 300-800 nm, and the absorption structure within this range remained similar. Moving to subfigure (b), the Tauc plot of the energy bandgap calculated $(\partial hv)^2$ vs. hv [288] is depicted. The controlled film demonstrated an energy bandgap of 1.67 eV, while the controlled film treated with TEA exhibited a slightly higher energy bandgap of 1.68 eV. However, when the CsPbI₃ was treated with TEA and CBEA and mixed with 5% CsBr, the energy band gaps increased further to 1.72 eV and 1.76 eV, respectively [289]. The lower energy bandgap observed in the case of mixed CsBr (1.67 eV) compared to CsBr mixed CsPbI₃ (1.76 eV) can be attributed to the perovskites treatment with bromine. Conversely, the increased energy bandgap resulting from the mixed CsBr treated with CBEA indicates that the iodine-containing film has a more significant effect on the bandgap than the presence of the bromine. Additionally, the treatment capability of CBEA was found to be inferior to that of TEA in the perovskite films [292]. In subfigure (c), the results of photoluminescence (PL) intensity are presented. The intensity of the films

increased in the following order: controlled film, controlled film treated with CBEA, controlled film treated with TEA, and 5% CsBr mixed controlled film treated with CBEA and TEA. Interestingly, the intensity of the film further increased when 5% CsBr was mixed in the precursor of the controlled perovskite films and stabilized with TEA, aligning with similar investigated by Johnston et al. and Olalerus et al. [291-292]. Moreover, it was observed that both the controlled film and controlled film treated with CBEA exhibited a peak at 596nm in their PL intensity. In contrast, when the 5% CsBr mixed CsPbI₃ perovskite film was treated with mixed antisolvents, a blue shift occurred at 594 nm. This suggests that bromine-containing perovskite films experience a blue shift in their PL intensity compared to films containing only iodine.

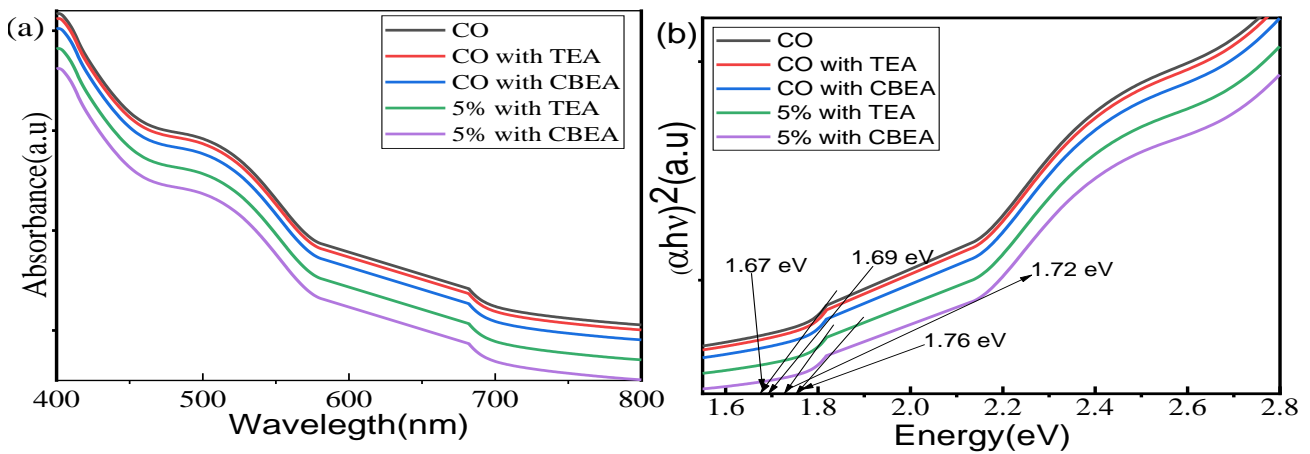


Figure 6. 2 The optical spectra of (a) Uv-Vis absorbance and (b) the Tauc plot of energy band gap perovskite film and 5% CsBr mixed with CsPbI₃ perovskite film

Figure 6.3 shows the effect of annealing temperature and antisolvent dripping time (Figures 6.4a&b) of 5% CsBr mixed with CsPbI₃ precursor and treated with TEA mixed antisolvent perovskite film. In this investigation we examine 5% CsBr mixed CsPbI₃ perovskite film using four different annealing temperature ranges (100°C, 120°C, 140°C, and 160°C) after spinning and four different antisolvent dripping times (last 5 sec, 10 sec, 15 sec, and 20 sec) before ending the spin coating time. The absorption spectra of 5% CsBr mixed CsPbI₃ perovskite film annealing with variable temperature shown (Figure 4a) that the absorption spectra increased with increasing the annealing temperature (100°C < 120°C < 140°C < 160°C) [293]. Figure 6.4b shows the absorption spectra of 5% CsBr mixed with CsPbI₃ perovskite film treated with TEA at different dripping times of antisolvent. Interestingly the absorption spectrum of the film increased with the dripping time of antisolvent before ending the spin coating time to 5sec > 10sec > 15 sec > 20 sec. From the

series of spin coating, the last 5-second antisolvent dripping time perovskite film had a good absorption spectrum. On the other hand with a variation of antisolvent dripping time, the PL intensity of the film fluctuated from red to blue and blue to red shift (Figure 6.4b). Before ending the dripping time of 20 seconds and 10 seconds the PL intensity was observed as a blue shift related to the dripping time of 5 seconds while a redshift showed when 15 second dripping time compared to other dripping times [294], among all antisolvent dripping time, the last 5 seconds had high PL intensive time. From the overall optical analysis of the Uv-Vis absorbance and PL intensity, 160°C and 5 seconds are preferable annealing temperature and dripping time respectively. The result indicates that the mixed CsBr concentration in the precursor of the perovskite creates a microstrain in the lattice of mixed perovskite film [295]. On the other hand, the selected concentration of CsBr (5 % CsBr) mixed CsPbI₃ perovskite treated with two mixed antisolvent(Toluene mixed with ethyl acetate(TEA) and chlorobenzene mixed with ethyl acetate (CBEA)) dripping at 5 seconds before the end of spin coating time and annealing at 160°C was shown in Figure 4(a-d). In both absorbance and PL intensity analysis shown, the perovskite treated with a mixture of Toluene and ethyl acetate (TEA) antisolvent has a good absorbance and higher photoluminescence intensity than the film treated with the mixture of chlorobenzene and ethyl acetate (CBEA).

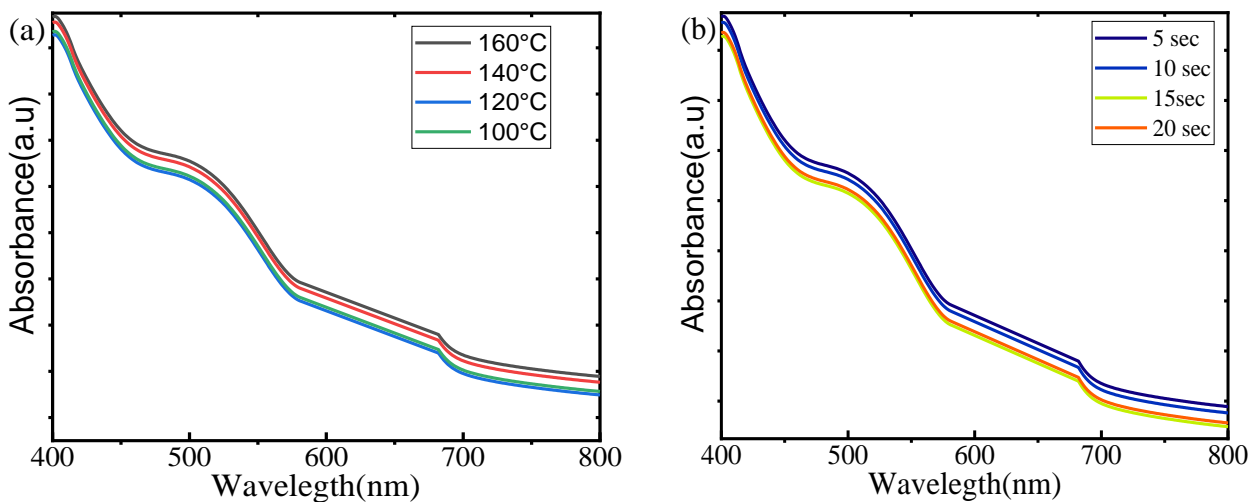


Figure 6. 3 Optical spectra of Pure & mixed halide perovskite with annealing temperature and dripping time

(a) the absorbance intensity of CsBr mixed CsPbI₃ perovskite with different annealing times, (c) the absorbance spectra of CsBr mixed CsPbI₃ perovskite with different antisolvent dripping time

Figure 6.5 shows the Fourier transform infrared spectroscopy (FTIR) figure of CsPbI₃ perovskite film and 5%CsBr mixed CsPbI₃ perovskite film treated with/without mixed

antisolvents. Interestingly there was a structural difference observed with the mixture of CsBr in CsPbI₃ perovskite film resulting from properties of bromine. The perovskite treated with mixed antisolvents had no change, indicating no negative effect on the structural property of the film while controlled and mixing CsBr in the controlled film treated with mixed antisolvents [273]. Strictly speaking, the controlled thin film treated with/without antisolvent has three characteristic similar peaks 876 cm⁻¹, 764 cm⁻¹, and 449 cm⁻¹. But CsPbI₃ perovskite film mixed with 5% CsBr has different characteristic peaks from controlled film and has 9 common characteristic peaks 1682 cm⁻¹, 1499 cm⁻¹, 1387 cm⁻¹, 1270 cm⁻¹, 1086 cm⁻¹, 1052 cm⁻¹, 738 cm⁻¹, 699 cm⁻¹, 660 cm⁻¹. The characteristic peak difference for controlled film and 5% CsBr mixed film indicates the improvement in morphology of the film, and enlargement crystal size.

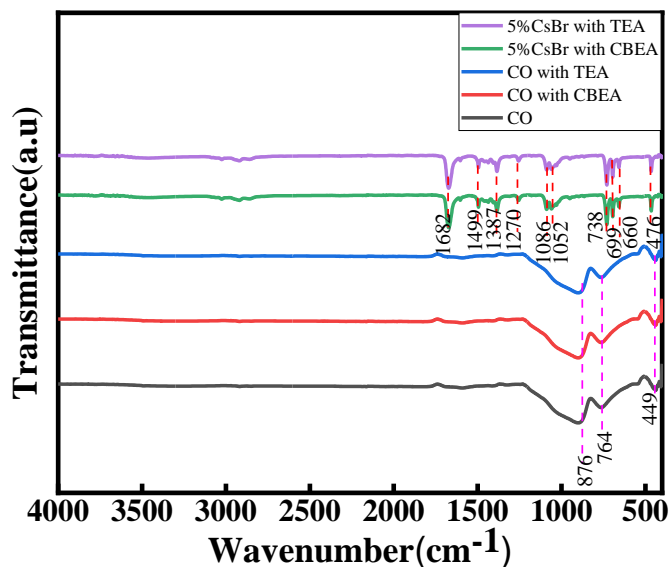


Figure 6. 4 The FTIR spectra of CsPbI₃ perovskite film and different concentrations of CsBr mixed with controlled perovskite film

The XRD configurations of the CsPbI₃ and CsPbI₃ mixed with 5% of CsBr and treated with antisolvent films are presented in Figure 6. The spreading peaks at $2\theta = 27.44^\circ$, 28.54° , 38.8° , 45.6° , and 54.5° can be indexed to the (211), (121), (222), (400), and (332) plans of the CsPbI₃ perovskite level respectively. The lattice parameters of the CsPbI₃ film were calculated to be $a = 6.21 \text{ \AA}$, $b = 6.21 \text{ \AA}$, and $c = 5.82 \text{ \AA}$, which are in good promise with the reported values [80,296]. The phase similarity indicated that the mixed CsBr in the perovskite film had no negative effect, miscible in precursor solution uniformly, and increased the crystalline size. Clearly, the figure shows that in the precursor of the controlled film mixed with 5% CsBr, there was a small approximation ($\sim 0.01^\circ$) shift to the left, which

might be from properties of bromination (bromine as additives). The addition of CsBr to the CsPbI₃ film increased the intensity of diffraction peaks, indicating an increase in the crystallinity of the film. This is likely due to the lattice match between the CsPbI₃ and CsBr phases, which can lead to the removal of defects and dislocation from the film. The intensity of 5% CsBr mixed with controlled film and treated with TEA was the highest, and a single perovskite phase with the P63mc space group. Toluene and ethyl acetate are miscible solvents, meaning that they can be mixed together in any proportion to form a single phase. This is because the two solvents have similar intermolecular forces, which allows them to interact with each other and form a homogeneous solution. The Flory-Huggins interaction parameter for toluene and ethyl acetate is -0.01, which indicates that the two solvents are strongly attracted to each other. This is due to the fact that both solvents are polar, and the dipole-dipole interactions between the molecules of the two solvents are strong enough to overcome the dispersive forces that would otherwise cause them to be immiscible, this indicated that the mixed antisolvents toluene and ethyl acetate (TEA) developed the phase value of the perovskite film. The film prepared with CBEA showed a small amount of impurity peaks, which were attributed to mixture of non-polarity compound Chlorobenzene and a polar compound ethyl acetate. When they are mixed together, the two compounds will form a heterogeneous mixture. This is because the non-polar chlorobenzene will not dissolve in the polar ethyl acetate and form two phases [294].

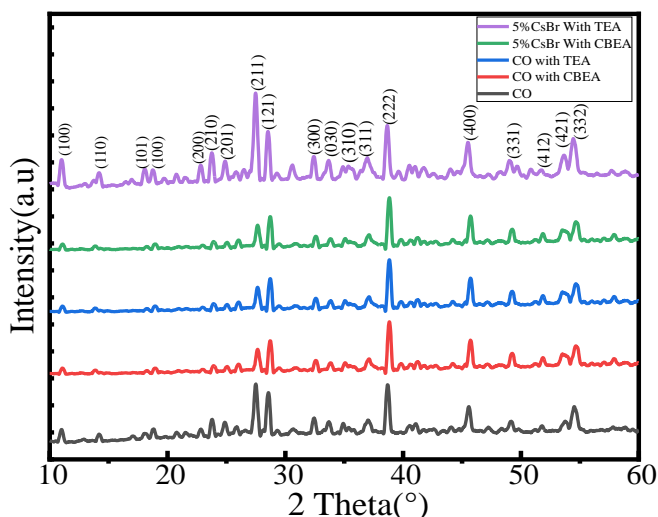


Figure 6. 5 XRD patterns of controlled and 5% CsBr mixed with controlled perovskite film treated with mixed antisolvents

As shown in field emission scanning electron microscope images, Figure 6.7, the morphology of the pristine CsPbI₃ film was much pinhole, even if after treatment with TEA (Figure 7a),

as evidenced by the formation of rod-like structures. The morphology of the 5% CsBr mixed film treated with TEA (Figure 6.7b), was also investigated. The 5% CsBr mixed perovskite film treated with TEA exhibited a denser surface, with fewer pinholes and a more rod-like structured morphology than the controlled film treated with TEA (Figure 6.7b). The result of this study indicates that the surface-morphology of the CsPbI₃ film can be enriched by mixing small concentration CsBr, treated with TEA. This improvement in morphology is likely due to the removal of defects from the films [295], which indicates to an increase in the film's energy harvesting efficiency.

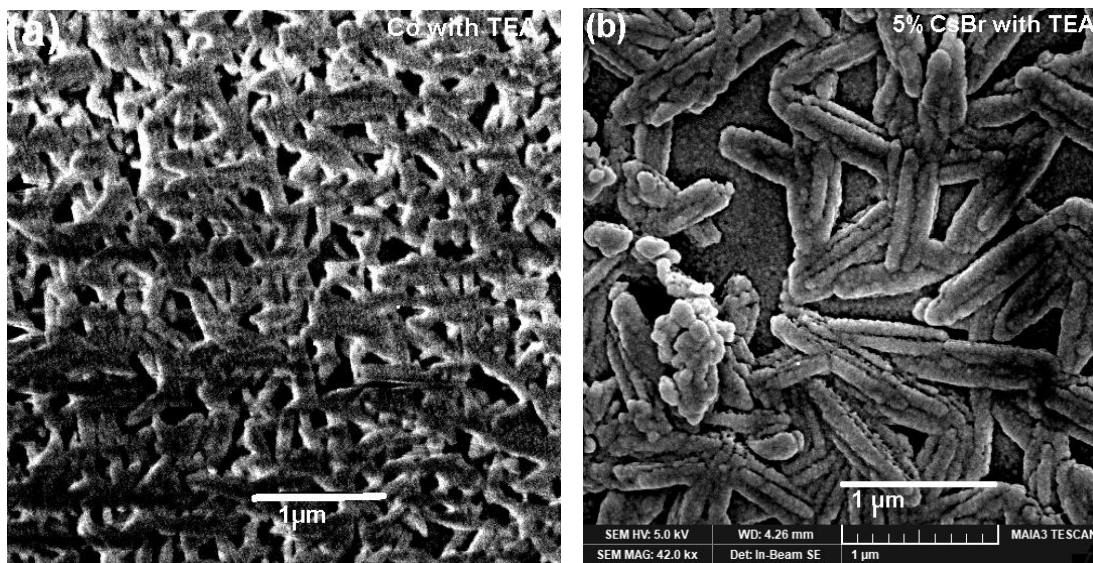


Figure 6. 6 The field emission scanning electron microscope (FE SEM) images of (a) CsPbI₃ perovskite film treated with TEA, (b) 5% CsBr mixed CsPbI₃ perovskite film treated with TEA.

The high-resolution transmittance electron microscope (HR-TEM) image of pure CsPbI₃ and CsBr mixed CsPbI₃ perovskite film treated with TEA is displayed in Figure 8 a & b respectively.

CsBr mixed CsPbI₃ perovskite film treated with TEA shows a well-ordered perovskite structure with a lattice spacing of 3.85 Å, which is a good agreement reported values (3.85 Å) [296]. Before being mixed with CsBr the pure perovskite material showed the Nanocrystals embedded in the crystalline matrix. In contrast, after being mixed with CsBr it showed more clouded and more embedded in the Nano-crystalline matrix, which is revealed in line with Lu et al. and Lv et al. s' work [297]. Before CsBr mixing, the layer of the film was not growing and there were some internal defects in the film. After CsBr was mixed in the precursor of Cesium Lead iodide precursor of the perovskite, the film looked at the shape and quality of

the grain size, and large cloudy grain boundaries were observed, indicating the good performance of the active layer for the film of the perovskite solar cell [298]. The image improvement in line with the image of SEM and XRD crystalline pattern indicates the mixture of a small amount of CsBr in the CsPbI₃ perovskite film.

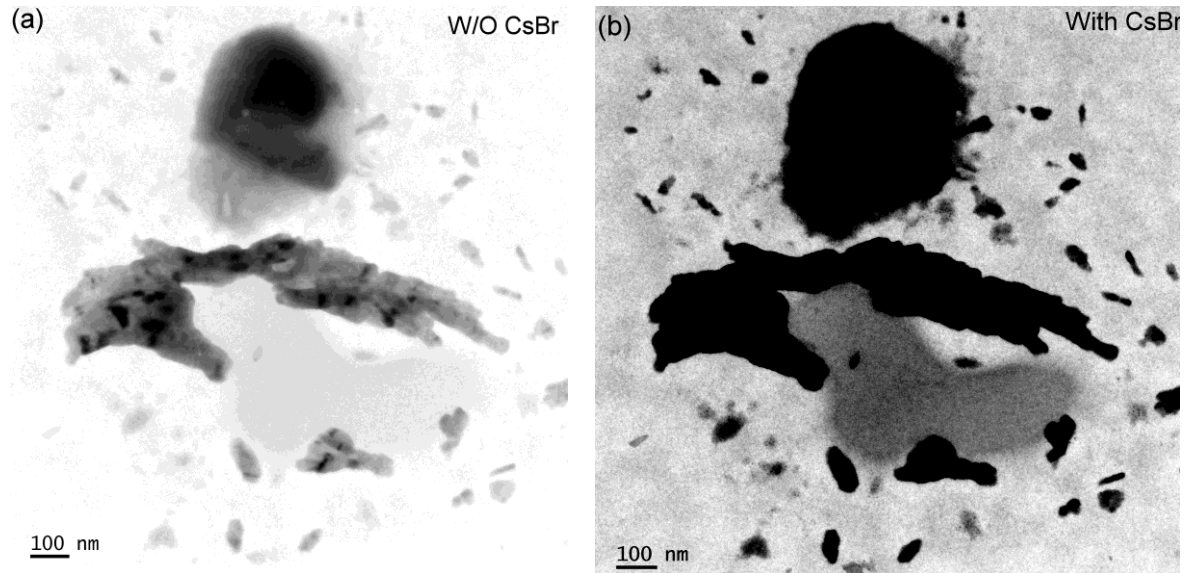


Figure 6. 7 TEM images of CsPbI₃ perovskite film (a) without CsBr mixed (b) With CsBr mixed

To finalize our demonstration we compared both controlled and 5% CsBr mixed cesium lead iodide perovskite films treated with mixed antisolvent toluene & ethyl acetate (TEA) as shown in Figure 6.9 a&b respectively. Before treatment the surface of the film (Figure 6.9a) showed non-uniform and had pinholes. After being mixed with 5% CsBr and treated with 5% TEA-mixed antisolvents (Figure 9b), the morphology of the films was improved due to the minimized number of pinholes, voids, and uniform surface. TEA treated pure perovskites' root-mean-square (RMS) roughness (Sq) value was 12.65 nm. After doping with 5% Br (Figure 6.10b) the surface of the perovskite film showed more likely uniform and the RMS roughness (Sq) value was 11.8 nm. The reduction of root-mean-square roughness showed that 5% CsBr mixed made the perovskite a quality film for light absorption applications. High correspondences were seen between antisolvent dripping time and the resultant film morphology, emphasizing the antisolvent treatment's significance in producing good-performance perovskite films [299]. This suggests that CsBr and the antisolvent TEA treatment can be used as a strategy to improve the performance of cesium lead iodide perovskite film to fabricate highly efficient all-inorganic solar cells.

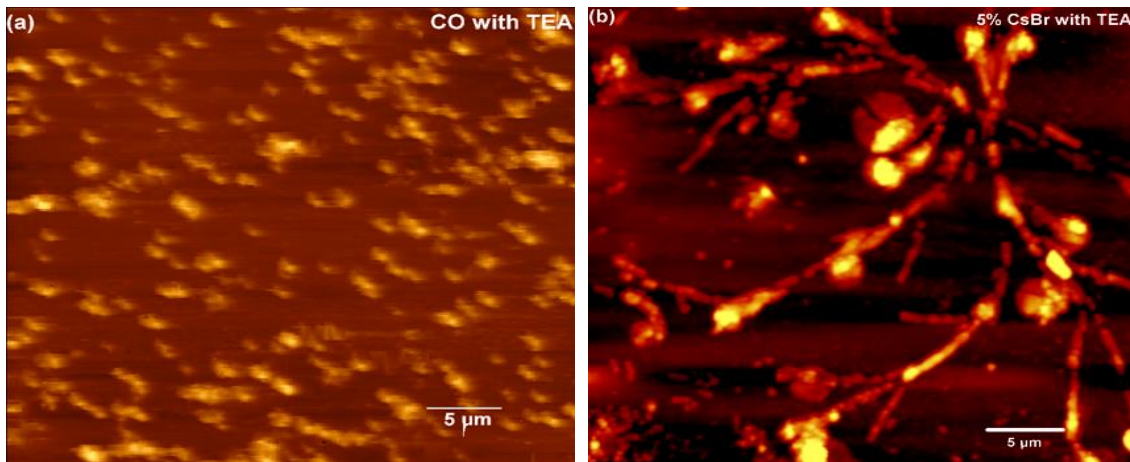


Figure 6. 8 AFM image of (a) control film treated with TEA, (b) 5% CsBr treated with TEA

6.5 Conclusions

The work summarized the improvement of all inorganic CsPbI_3 perovskite films by mixing cesium iodide and cesium bromide in a precursor of perovskite films. The absorbance and photoluminescence spectra results showed that 5% CsBr and 95% CsI mixture in CsPbI_2Br perovskite film had a higher quality spectrum than the controlled films. 5% of CsBr mixed perovskite treated with mixed antisolvent, TEA had a higher energy bandgap of 1.83 eV and had a red shift compared to controlled and treated with CBEA films in this investigation. The XRD and SEM analysis attributed that the grain size was increased after 5% CsBr mixed perovskite treated with mixed Toluene and Ethyl acetate (TEA). The SEM, TEM, and AFM morphological analysis attributed that after 5% CsBr the film's surface was smoothed, the voids were removed from the film's surface and the number of pinholes was minimized. This investigation used an effective way to stabilize the cubic phase of the perovskite film at low temperatures. It resulted in some supportive suggestions for developing high-performance all-inorganic perovskite solar cells. From the optical, crystalline, and morphology properties results, we can conclude that the 5% CsBr mixed with 95% CsPbI_3 concentration is critical to the quality of the resulting perovskite films. This result shows that the addition of CsBr to CsPbI_3 perovskite can improve their optical, crystalline, and morphological properties. This suggests that CsBr and the antisolvent TEA treatment can be used as a strategy to improve the performance of all-inorganic perovskite solar cells.

Chapter Seven

7. Conclusion and Recommendation

7.1 Conclusion

The result founded on overall investigations of this thesis are, interestingly achieved almost all objectives of the project works in this dissertation. The optical property result showed that the absorption spectra and photo luminesces of the all-inorganic perovskite film increased with self-doped cesium lead iodide perovskite film after doped with DIO and CN in the CsPbI₃ perovskite film. The energy bandgap where reduced from yellow phase of 2.84 eV to 1.83eV (self-doped CsPbI₃ perovskite film), 1.78eV (doped with DIO), 1.76 eV (doped with CN), and 2.59 eV (doped with ODT). Among this, after self-doped perovskite doping with CN and ODT are the appropriate bandgap for CsPbI₃ perovskite materials. From structural crystallographic XRD result, after self-doped and self-doped CsPbI₃ perovskite doped with additives (CN, DIO and ODT), the phase change occurs from yellow δ -phase to orthorhombic γ -phase. The FTIR result showed that there were no structural changes in IR spectra when additives including in the precursor solution of self-doped perovskite film. The results indicated that the miscibility of binary solvents (DMSO and DMF miscible with solvent additives (DIO &CN). Except ODT additive treated film the morphology of the perovskite film treated with DIO &CN were pinhole free, smooth and relatively flat surfaces compared with yellow phase.

The optical property result showed that the absorption spectra and photo luminesces life time of the all-inorganic CsPbI₂Br perovskite film increased after AgBr doped with CsPbI₂Br perovskite film. The energy bandgap of CsPbI₂Br perovskite film resulting bandgap increased slightly from 1.84 eV undoped to 1.87 eV (at 1 % AgBr), 1.95 eV (at 2% AgBr) and 1.96 eV (at 3% AgBr) due to redshift of the addition of bromine. The lifetime of the perovskite film increased from 0.99 ns of undoped film to 1.187 ns indicating that increasing the concentration of AgBr on perovskite film extended the lifetime of the film. Due to the crystallization kinetics being changed when AbBr was introduced into the perovskite precursor solutions, the crystallographic ordering decreases with increased lifetime AbBr concentrations. The SEM and TEM analysis results showed that up to 1% AgBr the film morphology was relatively smoother than the more concentration AgBr doping.

The optical property improved, and the energy bandgap of the perovskite film was increased when CsPbI_{2.93} perovskite film mixed with Br_{0.07} followed by treated with mixed antisolvents TEA.

The structural analysis result showed that increments in crystal size, grain size, high peak intensity, and peak purity were observed when CsPbI_{2.93}Br_{0.07} perovskite film treated with mixed antisolvents toluene and Ethyl acetate (TEA). With 5% CsBr mixed halide and treated with TEA, and CBTA in all inorganic perovskite, the FTIR result showed that there were structural changes in IR spectra due to bromine properties. The morphology analysis of the perovskite film image of SEM, and TEM, showed that before treatment the surface of the film was uniform, evidentially having road like structure on the surface of the film while, the film became smooth, pinhole-free and denser surface after thin film treated with mixed halide combine with mixed antisolvents respectively.

7.2 Recommendation

In thesis works we demonstrated all inorganic perovskite film in air conditions using the solution processing methods, and one-step spin coating at home room temperature to improve the perovskite film for photovoltaic nanotechnology. We investigated the self-doped cesium lead iodide perovskite treating by solvent additive, cesium lead mixed halide (CsPbI₂Br) doping with silver bromide and treating cesium lead iodide perovskite using both mixed halide and mixed antisolvent methods. Resultantly of the demonstration, the treated film showed improvement in optical, structural, and morphological when compared with the control perovskite film. Amazingly these results help the perovskite film for the active layer of all inorganic photovoltaic devices. Finally,

- we recommended that the result was used to further investigations on the stability issues of all inorganic perovskite optoelectronics.
- Include the tunability of the phase purity for the self-doped CsPbI₃ and self doped with additives CsPbI₃ perovskite film under ambient conditions for the active layer of semiconductors
- Some innovative ideas should be further required to secure the stability of all-inorganic perovskite (CsPbX₃) thin film as a next-generation semiconductor for optoelectronics.
- If the further investigation will be taken , the film will be a good light absorbing active layer for emerging photovoltaic nanotechnology

References

1. Paranthaman, M. P.; Wong-Ng, W.; Bhattacharya, R. N. *Semiconductor Materials for Solar Photovoltaic Cells*; 2015. <https://doi.org/10.1007/978-3-319-20331-7>.
2. Wang, M.; Wang, W.; Ma, B.; Shen, W.; Liu, L.; Cao, K.; Chen, S.; Huang, W. *Lead-Free Perovskite Materials for Solar Cells*; Springer Singapore, 2021; Vol. 13. <https://doi.org/10.1007/s40820-020-00578-z>.
3. Kang, H. Crystalline Silicon vs. Amorphous Silicon: The Significance of Structural Differences in Photovoltaic Applications. *IOP Conf. Ser. Earth Environ. Sci.* 2021, 726 (1). <https://doi.org/10.1088/1755-1315/726/1/012001>.
4. Liu, H.; Du, Y.; Yin, X.; Bai, M.; Liu, W. Micro/Nanostructures for Light Trapping in Monocrystalline Silicon Solar Cells. *J. Nanomater.* 2022, 2022. <https://doi.org/10.1155/2022/8139174>.
5. Shin, D. S.; Kim, T. H.; Rah, J. E.; Kim, D.; Yang, H. J.; Lee, S. B.; Lim, Y. K.; Jeong, J.; Kim, H.; Shin, D.; Son, J. Assessment of a Therapeutic X-Ray Radiation Dose Measurement System Based on a Flexible Copper Indium Gallium Selenide Solar Cell. *Sensors* 2022, 22 (15). <https://doi.org/10.3390/s22155819>.
6. Li, J.; Huang, J.; Cong, J.; Mai, Y.; Su, Z.; Liang, G.; Wang, A.; He, M.; Yuan, X.; Sun, H.; Yan, C.; Sun, K.; Ekins-Daukes, N. J.; Green, M. A.; Hao, X. Large-Grain Spanning Monolayer Cu₂ZnSnSe₄ Thin-Film Solar Cells Grown from Metal Precursor. *Small* 2022, 18 (9). <https://doi.org/10.1002/sml.202105044>.
7. Shen, W.; Zhao, Y.; Liu, F. Highlights of Mainstream Solar Cell Efficiencies in 2021. *Front. Energy* 2022, 16 (1), 1–8. <https://doi.org/10.1007/s11708-022-0816-x>.
8. Ramanujam, J.; Singh, U. P. Copper Indium Gallium Selenide Based Solar Cells - A Review. *Energy Environ. Sci.* 2017, 10 (6), 1306–1319. <https://doi.org/10.1039/c7ee00826k>.
9. Trivedi, S.; Prochowicz, D.; Parikh, N.; Mahapatra, A.; Pandey, M. K.; Kalam, A.; Tavakoli, M. M.; Yadav, P. Recent Progress in Growth of Single-Crystal Perovskites for Photovoltaic Applications. *ACS Omega* 2021, 6 (2), 1030–1042. <https://doi.org/10.1021/acsomega.0c04593>.
10. Jadoun, S.; Riaz, U. Biohybrid Solar Cells. *Fundam. Sol. Cell Des.* 2023, No. March 2022, 117–136. <https://doi.org/10.1002/9781119725022.ch5..>

11. Yao, E.; Chen, C.; Gao, J.; Liu, Y.; Chen, Q.; Cai, M.; Hsu, W.; Hong, Z.; Li, G.; Yang, Y. Solar Energy Materials & Solar Cells The Study of Solvent Additive Effects in Efficient Polymer Photovoltaics via Impedance Spectroscopy. *Sol. Energy Mater. Sol. Cells* 2014, 130, 20–26. <https://doi.org/10.1016/j.solmat.2014.05.049>.
12. Li, D.; Zhang, D.; Lim, K. S.; Hu, Y.; Rong, Y.; Mei, A.; Park, N. G.; Han, H. A Review on Scaling Up Perovskite Solar Cells. *Adv. Funct. Mater.* 2021, 31 (12), 1–27. <https://doi.org/10.1002/adfm.202008621>.
13. Mulder, J. T.; Jazi, M. A.; Manna, L.; Houtepen, A. J. Electrochemical p - Doping of CsPbBr₃ Perovskite Nanocrystals. 2021. <https://doi.org/10.1021/acsenergylett.1c00970>.
14. Siavash Moakhar, R.; Gholipour, S.; Masudy-Panah, S.; Seza, A.; Mehdikhani, A.; Riahi-Noori, N.; Tafazoli, S.; Timasi, N.; Lim, Y. F.; Saliba, M. Recent Advances in Plasmonic Perovskite Solar Cells. *Adv. Sci.* 2020, 7 (13), 1–19. <https://doi.org/10.1002/advs.201902448>.
15. Aghaei, M.; Pelosi, R.; Wong, W. W. H.; Schmidt, T.; Debije, M. G.; Reinders, A. H. M. E. Measured Power Conversion Efficiencies of Bifacial Luminescent Solar Concentrator Photovoltaic Devices of the Mosaic Series. *Prog. Photovoltaics Res. Appl.* 2022, 30 (7), 726–739. <https://doi.org/10.1002/pip.3546>.
16. Lin, C. Stabilizing Organic-Inorganic Lead Halide Perovskite Solar Cells With Efficiency Beyond 20%. *Front. Chem.* 2020, 8 (July), 1–7. <https://doi.org/10.3389/fchem.2020.00592>
17. Chen, Y.; He, M.; Peng, J.; Sun, Y.; Liang, Z. Structure and Growth Control of Organic-Inorganic Halide Perovskites for Optoelectronics : From Polycrystalline Films to Single Crystals. 2016. <https://doi.org/10.1002/advs.201500392>.
18. Zeng, Q.; Zhang, X.; Liu, C.; Feng, T.; Chen, Z.; Zhang, W.; Zheng, W.; Zhang, H.; Yang, B. Inorganic CsPbI₂Br Perovskite Solar Cells: The Progress and Perspective. *Sol. RRL* 2019, 3 (1). <https://doi.org/10.1002/solr.201800239>.
19. Katz, E. A. Perovskite: Name Puzzle and German-Russian Odyssey of Discovery. *Helv. Chim. Acta* 2020, 103 (6). <https://doi.org/10.1002/hlca.202000061>.
20. Jiang, X.; Zang, Z.; Zhou, Y.; Li, H.; Wei, Q.; Ning, Z. Tin Halide Perovskite Solar Cells: An Emerging Thin-Film Photovoltaic Technology. *Accounts Mater. Res.* 2021, 2 (4), 210–219. <https://doi.org/10.1021/accountsmr.0c00111>.

21. Krishna, B. G.; Sundar Ghosh, D.; Tiwari, S. Progress in Ambient Air-Processed Perovskite Solar Cells: Insights into Processing Techniques and Stability Assessment. *Sol. Energy* 2021, 224 (May), 1369–1395. <https://doi.org/10.1016/j.solener.2021.07.002>.
22. Wan, Y.; Li, E.; Yu, Z.; Huang, J. K.; Li, M. Y.; Chou, A. S.; Lee, Y. Te; Lee, C. J.; Hsu, H. C.; Zhan, Q.; Aljarb, A.; Fu, J. H.; Chiu, S. P.; Wang, X.; Lin, J. J.; Chiu, Y. P.; Chang, W. H.; Wang, H.; Shi, Y.; Lin, N.; Cheng, Y.; Tung, V.; Li, L. J. Low-Defect-Density WS₂ by Hydroxide Vapor Phase Deposition. *Nat. Commun.* 2022, 13 (1). <https://doi.org/10.1038/s41467-022-31886-0>.
23. Zheng, J.; Hu, L.; Yun, J. S.; Zhang, M.; Lau, C. F. J.; Bing, J.; Deng, X.; Ma, Q.; Cho, Y.; Fu, W.; Chen, C.; Green, M. A.; Huang, S.; Ho-Baillie, A. W. Y. Solution-Processed, Silver-Doped NiO_x as Hole Transporting Layer for High-Efficiency Inverted Perovskite Solar Cells. *ACS Appl. Energy Mater.* 2018, 1 (2), 561–570. <https://doi.org/10.1021/acsaem.7b00129>.
24. Dong, Y.; Zhao, Y.; Zhang, S.; Dai, Y.; Liu, L.; Li, Y.; Chen, Q. Recent Advances toward Practical Use of Halide Perovskite Nanocrystals. *J. Mater. Chem. A* 2018, 6, 21729–21746. <https://doi.org/10.1039/C8TA06376A>.
25. Chen, Z.; Dong, L.; Tang, H.; Yu, Y.; Ye, L.; Zang, J. Direct Synthesis of Cubic Phase CsPbI₃ Nanowires. *CrystEngComm* 2019, 21 (9), 1389–1396. <https://doi.org/10.1039/c8ce02111b>.
26. Akkerman, Q. A.; Rainò, G.; Kovalenko, M. V.; Manna, L. Genesis, Challenges and Opportunities for Colloidal Lead Halide Perovskite Nanocrystals. *Nat. Mater.* 2018, 17 (5), 394–405. <https://doi.org/10.1038/s41563-018-0018-4>.
27. Jariwala, S.; Burke, S.; Dunfield, S.; Shallock, C.; Taddei, M. Approaching the Limits of Optoelectronic Performance in Mixed Cation Mixed Halide Perovskites by Controlling Surface Recombination. Zhang, F.; Zhu, K. Additive Engineering for Efficient and Stable Perovskite Solar Cells. *Adv. Energy Mater.* 2020, 10 (13). <https://doi.org/10.1002/aenm.201902579>.
28. Liu, L.; Xiao, H.; Jin, K.; Xiao, Z.; Du, X.; Yan, K.; Hao, F.; Bao, Q.; Yi, C.; Liu, F.; Wang, W.; Zuo, C.; Ding, L. 4-Terminal Inorganic Perovskite/Organic Tandem Solar Cells Offer 22% Efficiency. *Nano-Micro Lett.* 2023, 15 (1), 1–10. <https://doi.org/10.1007/s40820-022-00995-2>
29. Zhang, F.; Zhu, K. Additive Engineering for Efficient and Stable Perovskite Solar Cells. *Adv. Energy Mater.* 2020, 10 (13), 1–26.

- <https://doi.org/10.1002/aenm.201902579>.
30. Liu, S.; Guan, Y.; Sheng, Y.; Hu, Y.; Rong, Y.; Mei, A.; Han, H. A Review on Additives for Halide Perovskite Solar Cells. *Adv. Energy Mater.* 2020, 10 (13), 1–28. <https://doi.org/10.1002/aenm.201902492>.
 31. Wu, Y.; Wang, Y.; Duan, J.; Yang, X.; Zhang, J.; Liu, L.; Tang, Q. Cluster Effect of Additives in Precursors for Inorganic Perovskites Solar Cells. *Electrochim. Acta* 2019, 135379. <https://doi.org/10.1016/j.electacta.2019.135379>.
 32. Choi, M. J.; Lee, Y. S.; Cho, I. H.; Kim, S. S.; Kim, D. H.; Kwon, S. N.; Na, S. I. Functional Additives for High-Performance Inverted Planar Perovskite Solar Cells with Exceeding 20% Efficiency: Selective Complexation of Organic Cations in Precursors. *Nano Energy* 2020, 71 (October 2019), 104639. <https://doi.org/10.1016/j.nanoen.2020.104639>.
 33. Aidas K, Angeli C, Bak KL, Bakken V, Bast R, Boman L, Christiansen O, Cimiraglia R, Coriani S, Dahle P, Dalskov EK. The Dalton quantum chemistry program system. *Wiley Interdisciplinary Reviews: Computational Molecular Science*. 2014 May;4(3):269-84.
 34. Grandhi, G. K.; Hardy, D.; Krishnaiah, M.; Vargas, B.; Al-Anesi, B.; Suryawanshi, M. P.; Solis-Ibarra, D.; Gao, F.; Hoye, R. L. Z.; Vivo, P. Wide-Bandgap Perovskite-Inspired Materials: Defect-Driven Challenges for High-Performance Optoelectronics. *Adv. Funct. Mater.* 2023, 2307441. <https://doi.org/10.1002/adfm.202307441>.
 35. Palmstrom, A. F.; Eperon, G. E.; Leijtens, T.; Prasanna, R.; Habisreutinger, S. N.; Nemeth, W.; Gaubing, E. A.; Dunfield, S. P.; Reese, M.; Nanayakkara, S.; Moot, T.; Werner, J.; Liu, J.; To, B.; Christensen, S. T.; McGehee, M. D.; van Hest, M. F. A. M.; Luther, J. M.; Berry, J. J.; Moore, D. T. Enabling Flexible All-Perovskite Tandem Solar Cells. *Joule* 2019, 3 (9), 2193–2204. <https://doi.org/10.1016/j.joule.2019.05.009>.
 36. Xiang, W.; Wang, Z.; Kubicki, D. J.; Tress, W.; Luo, J.; Prochowicz, D.; Akin, S.; Emsley, L.; Zhou, J.; Dietler, G.; Grätzel, M.; Hagfeldt, A. Europium-Doped CsPbI₂Br for Stable and Highly Efficient Inorganic Perovskite Solar Cells. *Joule* 2019, 3 (1), 205–214. <https://doi.org/10.1016/j.joule.2018.10.008>.
 37. Gao, B.; Meng, J.; Lu, J.; Zhao, R. CH₃NH₃PbI₃ Perovskite Solar Cells with Efficiency over 22% Fabricated by Green Antisolvent Method. *Mater. Lett.* 2020, 274, 127995. <https://doi.org/10.1016/j.matlet.2020.127995>.

38. Yang, H.; Wang, H.; Zhang, J.; Chang, J.; Zhang, C. A Facile Way to Improve the Performance of Perovskite Solar Cells by Toluene and Diethyl Ether Mixed Anti-Solvent Engineering. 2019, 3–6.
39. Heo, D. Y.; Han, S. M.; Woo, N. S.; Kim, Y. J.; Kim, T. Y.; Luo, Z.; Kim, S. Y. Role of Additives on the Performance of CsPbI₃ Solar Cells. *J. Phys. Chem. C* 2018, 122 (28), 15903–15910. <https://doi.org/10.1021/acs.jpcc.8b04613>.
40. Bai, D.; Zhang, J.; Jin, Z.; Bian, H.; Wang, K.; Wang, H.; Liang, L.; Wang, Q.; Liu, S. F. Interstitial Mn²⁺-Driven High-Aspect-Ratio Grain Growth for Low-Trap-Density Microcrystalline Films for Record Efficiency CsPbI₂Br Solar Cells. *ACS Energy Lett.* 2018, 3 (4), 970–978. <https://doi.org/10.1021/acsenergylett.8b00270>.
41. He, J.; Su, J.; Lin, Z.; Ma, J.; Zhou, L.; Zhang, S.; Liu, S. Enhanced Efficiency and Stability of All-Inorganic CsPbI₂Br Perovskite Solar Cells by Organic and Ionic Mixed Passivation. 2021, 2101367, 1–9. <https://doi.org/10.1002/advs.202101367>.
42. Chen, S.; Liu, X.; Wang, Z.; Li, W.; Gu, X.; Lin, J.; Yang, T.; Gao, X.; Kyaw, A. K. K. Defect Passivation of CsPbBr₃ with AgBr for High-Performance All-Inorganic Perovskite Solar Cells. *Adv. Energy Sustain. Res.* 2021, 2 (6), 2000099. <https://doi.org/10.1002/aesr.202000099>.
43. Im, J. H.; Lee, C. R.; Lee, J. W.; Park, S. W.; Park, N. G. 6.5% Efficient Perovskite Quantum-Dot-Sensitized Solar Cell. *Nanoscale* 2011, 3 (10), 4088–4093. <https://doi.org/10.1039/c1nr10867k>.
44. Li, D.; Shi, J.; Xu, Y.; Luo, Y.; Wu, H.; Meng, Q. Inorganic-Organic Halide Perovskites for New Photovoltaic Technology. *Natl. Sci. Rev.* 2018, 5 (4), 559–576. <https://doi.org/10.1093/nsr/nwx100>.
45. Liu, D.; Shao, Z.; Li, C.; Pang, S.; Yan, Y.; Cui, G. Structural Properties and Stability of Inorganic CsPbI₃ Perovskites. *Small Struct.* 2021, 2 (3). <https://doi.org/10.1002/sstr.202000089>.
46. Nedelcu, G.; Protesescu, L.; Yakunin, S.; Bodnarchuk, M.I.; Grotevent, M.J.; Kovalenko, M.V. Fast Anion-Exchange in Highly Luminescent Nanocrystals of Cesium Lead Halide Perovskites (CsPbX₃, X = Cl, Br, I). *Nano Lett.* 2015, 15, 5635–5640. <https://doi.org/10.3390/photonics10070802>.
47. Qiu, F.; Li, M.; Qi, J.; Jiang, Y.; Hu, J. Engineering Inorganic Lead Halide Perovskite Deposition toward Solar Cells with Efficiency Approaching 20 %.

- 2021, 66–83. <https://doi.org/10.1002/agt2.19>.
48. Faheem, M. B.; Khan, B.; Hashmi, J. Z.; Baniya, A.; Subhani, W. S.; Bobba, R. S.; Yildiz, A.; Qiao, Q. Insights from Scalable Fabrication to Operational Stability and Industrial Opportunities for Perovskite Solar Cells and Modules. *Cell Reports Physical Science*. Cell Press April 20, 2022. <https://doi.org/10.1016/j.xcrp.2022.100827>.
49. Wang, K.; Jin, Z.; Liang, L.; Bian, H.; Bai, D.; Wang, H.; Zhang, J.; Wang, Q.; Shengzhong, L. All-Inorganic Cesium Lead Iodide Perovskite Solar Cells with Stabilized Efficiency beyond 15%. *Nat. Commun.* 2018, 9 (1), 1–8. <https://doi.org/10.1038/s41467-018-06915-6>.
50. Bello, S.; Urwick, A.; Bastianini, F.; Nedoma, A. J.; Dunbar, A. ScienceDirect An Introduction to Perovskites for Solar Cells and Their Characterisation. *Energy Reports* 2022, 8, 89–106. <https://doi.org/10.1016/j.egyr.2022.08.205>.
51. Yufeng Li, Changyu Yang, Weisi Guo, Tianwei Duan, Z. Z. and Y. Z. All-Inorganic Perovskite Solar Cells Featuring Mixed Group IVA Cations - Nanoscale (RSC Publishing).
52. Pan, J.; Zhang, X.; Zheng, Y.; Xiang, W. Morphology Control of Perovskite Film for Efficient CsPbIBr₂ Based Inorganic Perovskite Solar Cells. *Sol. Energy Mater. Sol. Cells* 2021, 221 (November 2020), 110878. <https://doi.org/10.1016/j.solmat.2020.110878>.
53. Graham, L.; Orenstein, J. M. Processing Tissue and Cells for Transmission Electron Microscopy in Diagnostic Pathology and Research. *Nat. Protoc.* 2007, 2 (10), 2439–2450. <https://doi.org/10.1038/nprot.2007.304>.
54. Ouedraogo, N. A. N.; Chen, Y.; Xiao, Y. Y.; Meng, Q.; Han, C. B.; Yan, H.; Zhang, Y. Stability of All-Inorganic Perovskite Solar Cells. *Nano Energy* 2020, 67, 104249. <https://doi.org/10.1016/j.nanoen.2019.104249>.
55. Nandi, P.; Topwal, D.; Park, N. G.; Shin, H. Organic-Inorganic Hybrid Lead Halides as Absorbers in Perovskite Solar Cells: A Debate on Ferroelectricity. *J. Phys. D. Appl. Phys.* 2020, 53 (49). <https://doi.org/10.1088/1361-6463/abb047>.
56. Chen, W. C.; Hung, C. W.; Chang, C. H.; Liang, F. C.; Benas, J. S.; Yan, Z. L.; Lin, B. H.; Lin, J. H.; Kuo, C. C. Crystal Orientation and Insulating Ligand of Quasi-Two Dimensional Perovskite Optimized through Silver Ion Doping for Realizing Efficient Light Emitting Diodes. *Chem. Eng. J.* 2022, 443 (January),

136496. <https://doi.org/10.1016/j.cej.2022.136496>.
57. Svanström, S.; Jacobsson, T. J.; Boschloo, G.; Johansson, E. M. J.; Rensmo, H.; Cappel, U. B. Degradation Mechanism of Silver Metal Deposited on Lead Halide Perovskites. *ACS Appl. Mater. Interfaces* 2020, 12 (6), 7212–7221. <https://doi.org/10.1021/acsami.9b2031>
58. Maafa, I. M. All-Inorganic Perovskite Solar Cells: Recent Advancements and Challenges. *Nanomaterials*. MDPI May 2, 2022. <https://doi.org/10.3390/nano12101651>.
59. Ye, T.; Jin, S.; Singh, R.; Kumar, M.; Chen, W.; Wang, D.; Zhang, X.; Li, W.; He, D. Effects of Solvent Additives on the Morphology and Transport Property of a Perylene Diimide Dimer Film in Perovskite Solar Cells for Improved Performance. *Sol. Energy* 2020, 201 (October 2019), 927–934. <https://doi.org/10.1016/j.solener.2020.03.062>.
60. McDowell, C.; Abdelsamie, M.; Toney, M. F.; Bazan, G. C. Solvent Additives: Key Morphology-Directing Agents for Solution-Processed Organic Solar Cells. 2018, *1707114*, 1–30. <https://doi.org/10.1002/adma.201707114>.
61. Chen, Y.; Zhang, X.; Zhan, C.; Yao, J. Origin of Effects of Additive Solvent on Film-Morphology in Solution-Processed Nonfullerene Solar Cells. *ACS Appl. Mater. Interfaces* 2015, 7 (12), 6462–6471. <https://doi.org/10.1021/am507581w>.
62. Niu, J.; Yang, D.; Yang, Z.; Wang, D.; Zhu, X.; Zuo, S.; Feng, J.; Liu, S. F. Chelate-Pb Intermediate Engineering for High-Efficiency Perovskite Solar Cells. 2018. <https://doi.org/10.1021/acsami.8b02257>.
63. Zhao, W.; Yao, Z.; Yu, F.; Yang, D.; Liu, S. F. Alkali Metal Doping for Improved CH₃NH₃PbI₃ Perovskite Solar Cells. 2018, *1700131*, 1–7. <https://doi.org/10.1002/advs.201700131>.
64. Lin, D.; Zhan, Z.; Huang, X.; Liu, P.; Xie, W. Advances in Components Engineering in Vapor Deposited Perovskite Thin Film for Photovoltaic Application. *Materials Today Advances*. Elsevier Ltd December 1, 2022. <https://doi.org/10.1016/j.mtadv.2022.100277>.
65. Dai, T.; Li, X.; Zhang, Y.; Xu, D.; Geng, A.; Zhao, J.; Chen, X. Performance Improvement of Polymer Solar Cells with Binary Additives Induced Morphology Optimization and Interfa. *Sol. Energy* 2020, 201 (September 2021), 330–338. <https://doi.org/10.1016/j.solener.2020.03.021>.
66. Li, Q.; Wang, L. M.; Liu, S.; Guo, L.; Dong, S.; Ma, G.; Cao, Z.; Zhan, X.;

- Gu, X.; Zhu, T.; Cai, Y. P.; Huang, F. Vertical Composition Distribution and Crystallinity Regulations Enable High-Performance Polymer Solar Cells with 17% Efficiency. *ACS Energy Lett.* 2020, 5 (11), 3637–3646. <https://doi.org/10.1021/acsenerylett.0c01927>.
67. Liu, Y.; Fan, Q.; Liu, H.; Jalan, I.; Jin, Y.; Stam, J. Van; Moons, E.; Wang, E.; Lu, X.; Inganäs, O.; Zhang, F. In Situ, Optical Spectroscopy Demonstrates the Effect of Solvent Additive in the Formation of All-Polymer Solar Cells. *J. Phys. Chem. Lett.* 2022, 13 (11696–11702). <https://doi.org/10.1021/acs.jpcllett.2c03397>.
68. Wang, D. H.; Pron, A.; Leclerc, M.; Heeger, A. J. Additive-Free Bulk-Heterojunction Solar Cells with Enhanced Power Conversion Efficiency, Comprising a Newly Designed Selenophene-Thienopyrrolodione Copolymer. *Adv. Funct. Mater.* 2013, 23 (10), 1297–1304. <https://doi.org/10.1002/adfm.201202541>.
69. Schmidt, K.; Tassone, C. J.; Niskala, J. R.; Yiu, A. T.; Lee, O. P.; Weiss, T. M.; Wang, C.; Fréchet, J. M. J.; Beaujuge, P. M.; Toney, M. F. A Mechanistic Understanding of Processing Additive-Induced Efficiency Enhancement in Bulk Heterojunction Organic Solar Cells. *Adv. Mater.* 2014, 26 (2), 300–305. <https://doi.org/10.1002/adma.201303622>.
70. Hu, X.; Wang, M.; Huang, F.; Gong, X.; Cao, Y. 23% Enhanced Efficiency of Polymer Solar Cells Processed With 1-Chloronaphthalene As the Solvent Additive. *Synth. Met.* 2013, 164 (1), 1–5. <https://doi.org/10.1016/j.synthmet.2012.12.016>.
71. Richter, L. J.; Delongchamp, D. M.; Bokel, F. A.; Engmann, S.; Chou, K. W.; Amassian, A.; Schaible, E.; Hexemer, A. In Situ Morphology Studies of the Mechanism for Solution Additive Effects on the Formation of Bulk Heterojunction Films. *Adv. Energy Mater.* 2015, 5 (3), 1–11. <https://doi.org/10.1002/aenm.201400975>.
72. Coates, N. E.; Hwang, I. W.; Peet, J.; Bazan, G. C.; Moses, D.; Heeger, A. J. 1,8-Octanedithiol as a Processing Additive for Bulk Heterojunction Materials: Enhanced Photoconductive Response. *Appl. Phys. Lett.* 2008, 93 (7), 6–9. <https://doi.org/10.1063/1.2969405>.
73. Wang, W.; Song, L.; Magerl, D.; Moseguí González, D.; Körstgens, V.; Philipp, M.; Moulin, J. F.; Müller-Buschbaum, P. Influence of Solvent Additive 1,8-Octanedithiol on P3HT:PCBM Solar Cells. *Adv. Funct. Mater.* 2018, 28 (20), 1–9. <https://doi.org/10.1002/adfm.201800209>.

74. Fan, H.; Shang, H.; Li, Y.; Zhan, X. Efficiency Enhancement in Small Molecule Bulk Heterojunction Organic Solar Cells via Additive. *Appl. Phys. Lett.* 2010, *97* (13), 1–4. <https://doi.org/10.1063/1.3491268>.
75. Cho, S.; Lee, J. K.; Moon, J. S.; Yuen, J.; Lee, K.; Heeger, A. J. Bulk Heterojunction Bipolar Field-Effect Transistors Processed with Alkane Dithiol. *Org. Electron.* 2008, *9* (6), 1107–1111. <https://doi.org/10.1016/j.orgel.2008.08.017>.
76. Lau, C. F. J.; Zhang, M.; Deng, X.; Zheng, J.; Bing, J.; Ma, Q.; Kim, J.; Hu, L.; Green, M. A.; Huang, S.; Ho-Baillie, A. Correction to: Strontium-Doped Low-Temperature-Processed CsPbI₂Br Perovskite Solar Cells (ACS Energy Letters (2017) 2:10(2319-2325)). <https://doi.org/10.1021/acsenergylett.9b00937>.
77. Zhou, Y.; Chen, J.; Bakr, O. M.; Sun, H. T. Metal-Doped Lead Halide Perovskites: Synthesis, Properties, and Optoelectronic Applications. *Chem. Mater.* 2018, *30* (19), 6589–6613. <https://doi.org/10.1021/acs.chemmater.8b02989>.
78. Wang, J.; Zhang, J.; Zhou, Y.; Liu, H.; Xue, Q.; Li, X.; Chueh, C. C.; Yip, H. L.; Zhu, Z.; Jen, A. K. Y. Highly Efficient All-Inorganic Perovskite Solar Cells with Suppressed Non-Radiative Recombination by a Lewis Base. *Nat. Commun.* 2020, *11* (1), 1–9. <https://doi.org/10.1038/s41467-019-13909-5>.
79. Abicho, S.; Hailegnaw, B.; Workneh, G. A.; Yohannes, T. Role of Additives and Surface Passivation on the Performance of Perovskite Solar Cells. *Mater. Renew. Sustain. Energy* 2022, *11* (1), 47–70. <https://doi.org/10.1007/s40243-021-00206-9>.
80. Eze, V. O.; Carani, L. B.; Majumder, H.; Uddin, M. J.; Okoli, O. I. Inorganic Cesium Lead Mixed Halide Based Perovskite Solar Materials Modified with Functional Silver Iodide. *Sci. Rep.* 2022, *12* (1), 1–10. <https://doi.org/10.1038/s41598-022-11729-0>.
81. Eze, V. O.; Adams, G. R.; Braga Carani, L.; Simpson, R. J.; Okoli, O. I. Enhanced Inorganic CsPbI₂Br Perovskite Film for a Sensitive and Rapid Response Self-Powered Photodetector. *J. Phys. Chem. C* 2020, *124* (38), 20643–20653. <https://doi.org/10.1021/acs.jpcc.0c04144>.
82. Eze, M. C.; Eze, H. U.; Ugwuanyi, G. N.; Alnajideen, M.; Atia, A.; Olisa, S. C.; Rocha, V. G.; Min, G. Improving the Efficiency and Stability of In-Air Fabricated Perovskite Solar Cells Using the Mixed Antisolvent of Methyl Acetate and Chloroform. *Org. Electron.* 2022, *107* (March), 106552.

- <https://doi.org/10.1016/j.orgel.2022.106552>.
83. Muradov, A.; Frolushkina, D.; Samusenkov, V.; Zhamanbayeva, G.; Kot, S. Methods of Stability Control of Perovskite Solar Cells for High Efficiency. *Energies* 2021, *14* (10). <https://doi.org/10.3390/en14102918>.
 84. Winterton, N. The Green Solvent: A Critical Perspective. *Clean Technol. Environ. Policy* 2021, *23* (9), 2499–2522. <https://doi.org/10.1007/s10098-021-02188-8>.
 85. Vedantam, S.; Ranade, V. V. Crystallization: Key Thermodynamic, Kinetic and Hydrodynamic Aspects. *Sadhana - Acad. Proc. Eng. Sci.* 2013, *38* (6), 1287–1337. <https://doi.org/10.1007/s12046-013-0195-4>.
 86. Psimadas, D.; Georgoulas, P.; Valotassiou, V.; Loudos, G. Molecular Nanomedicine Towards Cancer: *J. Pharm. Sci.* 2012, *101* (7), 2271–2280. <https://doi.org/10.1002/jps>.
 87. Aryanti, P. T. P.; Ariono, D.; Hakim, A. N.; Wenten, I. G. Flory-Huggins Based Model to Determine Thermodynamic Property of Polymeric Membrane Solution. *J. Phys. Conf. Ser.* 2018, *1090* (1). <https://doi.org/10.1088/1742-6596/1090/1/012074>.
 88. Helf, E. Proposed Experiment to Estimate the Mixing Free Energy of Polymers. *Macromolecules* 1978, *11* (4), 682–685. <https://doi.org/10.1021/ma60064a013>.
 89. Wenning, C.; Barbe, S.; Achten, D.; Schmidt, A. M.; Leimenstoll, M. C. Prediction of Initial Miscibility for Ternary Polyurethane Reaction Mixtures on Basis of Solubility Parameters and Flory–Huggins Theory. *Macromol. Chem. Phys.* 2018, *219*(5), 1–8. <https://doi.org/10.1002/macp.201700544>.
 90. Wu, M. C.; Ho, C. M.; Hsiao, K. C.; Chen, S. H.; Chang, Y. H.; Jao, M. H. Antisolvent Engineering to Enhance Photovoltaic Performance of Methylammonium Bismuth Iodide Solar Cells. *Nanomaterials* 2023, *13* (1). <https://doi.org/10.3390/nano13010059>.
 91. Jathar, S. B.; Rondiya, S. R.; Bade, B. R.; Nasane, M. P.; Barma, S. V.; Jadhav, Y. A.; Rokade, A. V.; Kore, K. B.; Nilegave, D. S.; Tandale, P. U.; Jadkar, S. R.; Funde, A. M. Facile Method for Synthesis of CsPbBr₃ Perovskite at Room Temperature for Solar Cell Applications. *ES Mater. Manuf.* 2021, *12*, 72–77. <https://doi.org/10.30919/esmm5f1036>. <https://doi.org/10.1039/c9nr08516e>.

92. Murthy, K. V. R.; Virk, H. S. Luminescence Phenomena: An Introduction. *Defect Diffus. Forum* 2014, 347, 1–34. <https://doi.org/10.4028/www.scientific.net/DDF.347.1>.
93. Park, J.; Kim, Y.; Ham, S.; Woo, J. Y.; Kim, T.; Jeong, S.; Kim, D. A Relationship between the Surface Composition and Spectroscopic Properties of Cesium Lead Bromide (CsPbBr₃) Perovskite Nanocrystals: Focusing on Photoluminescence Efficiency. *Nanoscale* 2020, 12 (3), 1563–1570. <https://doi.org/10.1039/c9nr08516e>.
94. Gidey, A.T.; Kim, J.Y. Tuning the crystallization process of perovskite active layer using a functionalized graphene oxide for enhanced photovoltaic performance. *J. Mater. Sci. Mater. Electron.* 2020, 31, 12257–12268. <https://doi.org/10.1007/s10854-020-03771-3>
95. Gidey, A.T.; Assayehegn, E.; Kim, J.Y. Hydrophilic Surface-Driven Crystalline Grain Growth of Perovskites on Metal Oxides. *ACS Appl. Energy Mater.* 2021, 4, 6923–6932. <https://doi.org/10.1021/acsaem.1c01020>
96. Mączka, M.; Ptak, M.; Gągor, A.; Stefańska, D.; Zaręba, J.K.; Sieradzki, A. Methylhydrazinium Lead Bromide: Noncentrosymmetric Three-Dimensional Perovskite with Exceptionally Large Framework Distortion and Green Photoluminescence. *Chem. Mater.* 2020, 32, 1667–1673. <https://doi.org/10.1021/acs.chemmater.9b05273>
97. Stefańska, D.; Ptak, M.; Mączka, M. Synthesis, Photoluminescence and Vibrational Properties of Aziridinium Lead Halide Perovskites. *Molecules* 2022, 27, 7949. <https://doi.org/10.3390/molecules27227949>
98. Sun, J.; Wu, J.; Tong, X.; Lin, F.; Wang, Y.; Wang, Z.M. Organic/Inorganic Metal Halide Perovskite Optoelectronic Devices beyond Solar Cells. *Adv. Sci.* 2018, 5, 1700780. <https://doi.org/10.1002/advs.201700780>
99. Yang, H.; Wang, H.; Wang, K.; Liu, D.; Zhao, L.; Chen, D.; Zhu, W.; Zhang, J.; Zhang, C. Recent Progress of Film Fabrication Process for Carbon-Based All-Inorganic Perovskite Solar Cells. *Crystals* 2023, 13, 679. <https://doi.org/10.3390/cryst13040679>.
100. Moot, T.; Marshall, A. R.; Wheeler, L. M.; Habisreutinger, S. N.; Tracy, H.; Boyd, C. C.; Dikova, D. R.; Pach, G. F.; Hazarika, A.; McGehee, D.; Snaith, H. J.; Luther, J. M. CsI-Antisolvent Adduct Formation in All-Inorganic Metal Halide

- Perovskites. *Adv. Energy Mater.* 2020, 10, 1903365. <https://doi.org/10.1002/aenm.201903365>.
101. Murugadoss, G.; Thangamuthu, R.; Senthil Kumar, S. M.; Anandhan, N.; Rajesh Kumar, M.; Rathishkumar, A. Synthesis of Ligand-Free, Large Scale with High Quality All-Inorganic CsPbI₃ and CsPb₂Br₅ Nanocrystals and Fabrication of All-Inorganic Perovskite Solar Cells. *J. Alloys Compd.* 2019, 787, 17–26. <https://doi.org/10.1016/j.jallcom.2019.02.018>.
102. Kulbak, M.; Gupta, S.; Kedem, N.; Levine, I.; Bendikov, T.; Hodes, G.; Cahen, D. Cesium Enhances Long-Term Stability of Lead Bromide Perovskite-Based Solar Cells. *J. Phys. Chem. Lett.* 2016, 7, 167–172. <https://doi.org/10.1021/acs.jpcclett.5b02597>
103. Stoumpos, C.C.; Malliakas, C.D.; Kanatzidis, M.G. Semiconducting Tin and Lead Iodide Perovskites with Organic Cations: Phase Transitions, High Mobilities, and Near-Infrared Photoluminescent Properties. *Inorg. Chem.* 2013, 52, 9019–9038. <https://doi.org/10.1021/ic401215x>
104. Eperon, G.E.; Stranks, S.D.; Menelaou, C.; Johnston, M.B.; Herz, L.M.; Snaith, H.J. Formamidinium lead trihalide: a broadly tunable perovskite for efficient planar heterojunction solar cells. *Energy Environ. Sci.* 2014, 7, 982–988. <https://doi.org/10.1039/C3EE43822H>
105. Zeng, L.; Chen, S.; Forberich, K.; Brabec, C. J.; Mai, Y.; Guo, F. Controlling the Crystallization Dynamics of Photovoltaic Perovskite Layers on Larger-Area Coatings. *Energy Environ. Sci.* 2020, 13, 4666–4690. <https://doi.org/10.1039/d0ee02575e>.
106. Ding, N.; Wu, Y.; Xu, W.; Lyu, J.; Wang, Y.; Zi, L.; Shao, L.; Sun, R.; Wang, N.; Liu, S. A novel approach for designing efficient broadband photodetectors expanding from deep ultraviolet to near infrared. *Light Sci. Appl.* 2022, 11, 91. <https://doi.org/10.1038/s41377-022-00777-w>
107. Cao, L.; Liu, X.; Li, Y.; Li, X.; Du, L.; Chen, S.; Zhao, S.; Wang, C. Recent Progress in All-Inorganic Metal Halide Nanostructured Perovskites: Materials Design, Optical Properties, and Application. *Front. Phys.* 2021, 16, 33201. <https://doi.org/10.1007/s11467-020-1026-9>
108. Cheng, J.; Fan, Z.; Dong, J. Research Progress of Green Solvent in CsPbBr₃ Perovskite Solar Cells. *Nanomaterials* 2023, 13, 991. <https://doi.org/10.3390/nano13060991>

109. Zeng, Q.; Zhang, X.; Liu, C.; Feng, T.; Chen, Z.; Zhang, W.; Zheng, W.; Zhang, H.; Yang, B. Inorganic CsPbI₂Br Perovskite Solar Cells: The Progress and Perspective. *Sol. RRL* 2019, 3, 1800239. <https://doi.org/10.1002/solr.201800239>.
110. Dong, Y.; Zhao, Y.; Zhang, S.; Dai, Y.; Liu, L.; Li, Y.; Chen, Q. Recent Advances toward Practical Use of Halide Perovskite Nanocrystals. *J. Mater. Chem. A* 2018, 6, 21729–21746. <https://doi.org/10.1039/C8TA06376A>.
111. Faridi, A. W.; Imran, M.; Tariq, G. H.; Ullah, S.; Noor, S. F.; Ansar, S.; Sher, F. Synthesis and Characterization of High-Efficiency Halide Perovskite Nanomaterials for Light-Absorbing Applications. *Ind. Eng. Chem. Res.* 2023, 62, 4494–4502. <https://doi.org/10.1021/acs.iecr.2c00416>
112. Hasan, M.S.; Alom, J.; Asaduzzaman, M.; Ahmed, M.B.; Hossain, M.D.; Saem, A.; Masud, J.; Thakare, J.; Hossain, M.A. Recent Criterion on Stability Enhancement of Perovskite Solar Cells. *Processes* 2022, 10, 1408. <https://doi.org/10.3390/pr10071408>
113. Ma, J.; Su, J.; Lin, Z.; He, J.; Zhou, L.; Li, T.; Zhang, J.; Liu, S.; Chang, J.; Hao, Y. Double Side Interfacial Optimization for Low-Temperature Stable CsPbI₂Br Perovskite Solar Cells with High Efficiency Beyond 16%. *Energy Environ. Mater.* 2022, 5, 637–644. <https://doi.org/10.1002/eem2.12212>.
114. Kirakosyan, A.; Kim, Y.; Sihn, R.; Jeon, M.; Jeong, J. Solubility-Controlled Room-Temperature Synthesis of Cesium Lead Halide Perovskite Nanocrystals. *ChemNanoMat* 2020, 6, 1–8. <https://doi.org/10.1002/cnma.202000471>
115. Dong, Y.; Qiao, T.; Kim, D.; Parobek, D.; Rossi, D.; Son, D. H. Precise Control of Quantum Confinement in Cesium Lead Halide Perovskite Quantum Dots via Thermodynamic Equilibrium. *Nano Lett.* 2018, 18, 3716–3722. <https://doi.org/10.1021/acs.nanolett.8b00861>.
116. Bioki, H.A.; Moshaii, A.; Zarandi, M.B. Improved Morphology, Structure and Optical Properties of CH₃NH₃PbI₃ Film via HQ Additive in PbI₂ Precursor Solution for Efficient and Stable Mesoporous Perovskite Solar Cells. *Synth. Met.* 2022, 283, 116965. <https://doi.org/10.1016/j.synthmet.2021.116965>.
117. Kumar, A.; Rana, N. K.; Rani, S.; Ghosh, D. S. Toward all-Inorganic Perovskite Solar Cells: Materials, performance, and stability. *Int. J. Energy Res.* 2022, 46, 14659–14695. <https://doi.org/10.1002/er.8240>.
118. Wang, J.; Che, Y.; Duan, Y.; Liu, Z.; Yang, S.; Xu, D.; Fang, Z.; Lei, X.; Li, Y.; Liu, S. 21.15%-Efficiency and Stable γ -CsPbI₃ Perovskite Solar Cells Enabled

- by an Acyloin Ligand. *Adv. Mater.* 2023, 35, 1–10. <https://doi.org/10.1002/adma.202210223>.
119. Park, J.; Kim, J.; Yun, H.-S.; Paik, M.J.; Noh, E.; Mun, H.J.; Kim, M.G.; Shin, T.J.; Seok, S.I. Controlled growth of perovskite layers with volatile alkylammonium chlorides. *Nature* 2023, 616, 724–730. <https://doi.org/10.1038/s41586-023-05825-y>
120. Zhu, X; Ge, L, Wang, Y; Li, M; Zhang, R; Xu, M; Zhao, Z; Lv, W; Chen, R. Recent Advances in Enhancing and Enriching the Optical Properties of Cl-Based CsPbX₃ Nanocrystals. *Adv. Optical Mater.* 2021, 9, 2100058. <https://doi.org/10.1002/adom.202100058>
121. Xiang, W; Liu, S F; Tress, W. A review on the stability of inorganic metal halide perovskites: challenges and opportunities for stable solar cells. *Energy Environ. Sci.* 2021, 14, 2090–2113. <https://doi.org/10.1039/D1EE00157D>
122. Zhao, Y.; Zhu, K. Organic–inorganic hybrid lead halide perovskites for optoelectronic and electronic applications. *Chem. Soc. Rev.* 2016, 45, 655–689. <https://doi.org/10.1039/C4CS00458B>
123. Alaei, A.; Circelli, A.; Yuan, Y.; Yang, Y.; Lee, S. S. Polymorphism in metal halide perovskites. *Mater. Adv.* 2021, 2, 47–63. <https://doi.org/10.1039/D0MA00643B>
124. Wang, B.; Novendra, N.; Navrotsky, A. Energetics, Structures, and Phase Transitions of Cubic and Orthorhombic Cesium Lead Iodide (CsPbI₃) Polymorphs. *J. Am. Chem. Soc.* 2019, 141, 14501–14504. <https://doi.org/10.1021/jacs.9b05924>
125. Sutton, R.J.; Filip, M.R.; Haghighirad, A.A.; Sakai, N.; Wenger, B.; Giustino, F.; Snaith, H.J. Cubic or Orthorhombic? Revealing the Crystal Structure of Metastable Black-Phase CsPbI₃ by Theory and Experiment. *ACS Energy Lett.* 2018, 3, 1787–1794. <https://doi.org/10.1021/acseenergylett.8b00672>
126. Xu, F.; Zhang, M.; Li, Z.; Yang, X.; Zhu, R. Challenges and Perspectives toward Future Wide-Bandgap Mixed-Halide Perovskite Photovoltaics. *Adv. Energy Mater.* 2023, 13, 2203911. <https://doi.org/10.1002/aenm.202203911>
127. Tan, S.; Yu, B.; Cui, Y.; Meng, F.; Huang, C.; Li, Y.; Chen, Z.; Wu, H.; Shi, J.; Luo, Y.; Li, D.; Meng, Q. Temperature-Reliable Low-Dimensional Perovskites Passivated Black-Phase CsPbI₃ toward Stable and Efficient Photovoltaics. *Angew. Chem. Int. Ed.* 2022, 61, e202201300. <https://doi.org/10.1002/anie.202201300>
128. Bian, H.; Wang, Q.; Yang, S.; Yan, C.; Wang, H.; Liang, L.; Jin, Z.; Wang, G.; Liu, S. Nitrogen-Doped Graphene Quantum Dots for 80% Photoluminescence

- Quantum Yield for Inorganic γ -CsPbI₃ Perovskite Solar Cells with Efficiency beyond 16%. *J. Mater. Chem. A* 2019, 7, 5740–5747. <https://doi.org/10.1039/c8ta12519h>.
129. Ahmad, M.; Rehman, G.; Ali, L.; Shafiq, M.; Iqbal, R.; Ahmad, R.; Khan, T.; Jalali-Asadabadi, S.; Maqbool, M.; Ahmad, I. Structural, Electronic and Optical Properties of CsPbX₃(X=Cl, Br, I) for Energy Storage and Hybrid Solar Cell Applications. *J. Alloys Compd.* 2017, 705, 828–839. <https://doi.org/10.1016/j.jallcom.2017.02.147>.
130. Zhang, F.; Zhu, K. Additive Engineering for Efficient and Stable Perovskite Solar Cells. *Adv. Energy Mater.* 2020, 10, 1–68. <https://doi.org/10.1002/aenm.201902579>
131. Zhang, L.; Han, B.; Liu, Z.; Yao, Y.; Xu, L.; Wang, P.; Lin, P.; Wu, X.; Yu, X.; Cui, C. Additive Engineering on Spiro-OMeTAD Hole Transport Material for CsPbI₃ All-Inorganic Perovskite Solar Cells with Improved Performance and Stability. *J. Alloys Compd.* 2022, 911, 164972. <https://doi.org/10.1016/j.jallcom.2022.164972>
132. Khorshidi, E.; Rezaei, B.; Kavousighahfarokhi, A.; Hanisch, J.; Reus, M. A.; Mu, P.; Ameri, T. Antisolvent Additive Engineering for Boosting Performance and Stability of Graded Heterojunction Perovskite Solar Cells Using Amide-Functionalized Graphene Quantum Dots. *ACS Appl. Mater. Interfaces* 2022, 14, 54623–54634. <https://doi.org/10.1021/acsami.2c12944>
133. Zhou, Y.; Chen, J.; Bakr, O. M.; Sun, H. T. Metal-Doped Lead Halide Perovskites: Synthesis, Properties, and Optoelectronic Applications. *Chem. Mater.* 2018, 30 (19), 6589–6613. <https://doi.org/10.1021/acs.chemmater.8b02989>.
134. Tian, J.; Wang, J.; Xue, Q.; Niu, T.; Yan, L.; Zhu, Z.; Li, N.; Brabec, C.J.; Yip, H.-L.; Cao, Y. Composition Engineering of All-Inorganic Perovskite Film for Efficient and Operationally Stable Solar Cells. *Adv. Funct. Mater.* 2020, 30, 2001764. <https://doi.org/10.1002/adfm.202001764>
135. Sun, H.; Zhang, J.; Gan, X.; Yu, L.; Yuan, H.; Shang, M.; Lu, C.; Hou, D.; Hu, Z.; Zhu, Y.; Han, L. Pb-Reduced CsPb_{0.9}Zn_{0.1}I₂Br Thin Films for Efficient Perovskite Solar Cells. *Adv. Energy Mater.* 2019, 9, 1900896. <https://doi.org/10.1002/aenm.201900896>.

136. Liu, B.; Long, M.; Cai, M.-Q.; Yang, J. Interface engineering of CsPbI₃-black phosphorus van der Waals heterostructure. *Appl. Phys. Lett.* 2018, *112*, 043901. <https://doi.org/10.1063/1.5016868>
137. Eperon, G.E.; Paternò, G.M.; Sutton, R.J.; Zampetti, A.; Haghighirad, A.A.; Cacialli, F.; Snaith, H.J. Inorganic caesium lead iodide perovskite solar cells. *J. Mater. Chem. A*, 2015, *3*, 19688-19695. <https://doi.org/10.1039/C5TA06398A>
138. Marronnier, A.; Roma, G.; Boyer-richard, S.; Pedesseau, L.; Jancu, J.; Bonnassieux, Y.; Katan, C.; Stoumpos, C. C.; Kanatzidis, M. G.; Even, J. Anharmonicity and Disorder in the Black Phases of Cesium Lead Iodide Used for Stable Inorganic Perovskite Solar Cells. *ACS Nano* 2018, *12*, 3477–3486. <https://doi.org/10.1021/acsnano.8b00267>.
139. Zhang, Q.; Zhou, Y.; Wei, Y.; Tai, M.; Gu, Y.; Han, J.; Yin, X.; Li, J.; Lin, H. Improved phase stability of γ -CsPbI₃ perovskite nanocrystals using the interface effect using iodine modified graphene oxide. *J. Mater. Chem. C*, 2020, *8*, 2569-2578. <https://doi.org/10.1039/C9TC06465F>
140. Wang, K.; Jin, Z.; Liang, L.; Bian, H.; Wang, H.; Feng, J.; Wang, Q.; Liu, S. Chlorine doping for black γ -CsPbI₃ solar cells with stabilized efficiency beyond 16%. *NanoEnergy* 2019, *58*, 175-182. <https://doi.org/10.1016/j.nanoen.2019.01.034>
141. Huang, L.; Xu, P.; Yu, F.; Liu, J.; Shirai, Y.; Zhang, X.-P.; Li, C.-H.; Song, Y. A stabilized γ -CsPbI₃ by poly(allylamine hydrochloride) for wide-band gap perovskites solar cells with enhanced performance. *J. Solid State Chem.* 2023, *324*, 124087. <https://doi.org/10.1016/j.jssc.2023.124087>
142. Zhang, Z.; Ji, R.; Kroll, M.; Hofstetter, Y. J.; Jia, X.; Becker-Koch, D.; Paulus, F.; Löffler, M.; Nehm, F.; Leo, K.; Vaynzof, Y. Efficient Thermally Evaporated γ -CsPbI₃ Perovskite Solar Cells. *Adv. Energy Mater.* 2021, *11* (29), 1–10. <https://doi.org/10.1002/aenm.202100299>.
143. Qiu, Z.; Wang, F.; Wang, C.; Zhu, C.; Wang, H.; Chen, Q.; Chen, Y.; Zhang, Y.; Guo, Z.; Li, N.; Zai, H.; Vicent-Luna, J. M.; Tao, S.; Zhou, H. Phase Transformation Barrier Modulation of CsPbI₃ Films via PbI₃- Complex for Efficient All-Inorganic Perovskite Photovoltaics. *Nano Energy* 2022, *99*, 2211-2255. <https://doi.org/10.1016/j.nanoen.2022.107388>.
144. Zhu, K.; Zhao, Y. Organic–inorganic hybrid lead halide perovskites for optoelectronic and electronic applications. *Chem. Soc. Rev.* 2016, *45*, 655-689. <https://doi.org/10.1039/C4CS00458B>

145. Mahapatra, A.; Prochowicz, D.; Tavakoli, M.M.; Trivedi, S.; Kumara, P.; Yadav, P. A review of aspects of additive engineering in perovskite solar cells. *J. Mater. Chem. A*, 2020, 8, 27-54. <https://doi.org/10.1039/C9TA07657C>
146. Mikhnenko, O.V.; Blom, P.W.M.; Nguyen, T.-Q. Exciton diffusion in organic semiconductors. *Energy Environ. Sci.* 2015, 8, 1867–1888. <https://doi.org/10.1039/C5EE00925A>
147. Tamai, Y.; Ohkita, H.; Benten, H.; Ito, S. Exciton Diffusion in Conjugated Polymers: From Fundamental Understanding to Improvement in Photovoltaic Conversion Efficiency. *J. Phys. Chem. Lett.* 2015, 6, 3417–3428. <https://doi.org/10.1021/acs.jpcclett.5b01147>
148. Firdaus, Y.; Le Corre, V.M.; Karuthedath, S.; Liu, W.; Markina, A.; Huang, W.; Chattopadhyay, S.; Nahid, M.M.; Nugraha, M.I.; Lin, Y.; et al. Long-range exciton diffusion in molecular non-fullerene acceptors. *Nat. Commun.* 2020, 11, 5220. <https://doi.org/10.1038/s41467-020-19029-9>
149. Xiang, W.; Zhang, J.; Liu, S.; Albrecht, S.; Hagfeldt, A.; Wang, Z. Intermediate phase engineering of halide perovskites for photovoltaics. *Joule* 2022, 6, 315-339. <https://doi.org/10.1016/j.joule.2021.11.013>
150. Jung, M.; Ji, S.-G.; Kim, G.; Seok, S.I. Perovskite precursor solution chemistry: from fundamentals to photovoltaic applications. *Chem. Soc. Rev.* 2019, 48, 2011-2038. <https://doi.org/10.1039/C8CS00656C>
151. Liu, Y.; Fan, Q.; Liu, H.; Jalan, I.; Jin, Y.; Stam, J.V.; Moons, E.; Wang, E.; Lu, X.; Inganäs, O.; Zhang, F. In Situ Optical Spectroscopy Demonstrates the Effect of Solvent Additive in the Formation of All-Polymer Solar Cells. *J. Phys. Chem. Lett.* 2022, 13, 11696–11702. <https://doi.org/10.1021/acs.jpcclett.2c03397>
152. Bao, S.; Yang, H.; Fan, H.; Zhang, J.; Wei, Z.; Cui, C.; Li, Y. Volatilizable Solid Additive-Assisted Treatment Enables Organic Solar Cells with Efficiency over 18.8% and Fill Factor Exceeding 80%. *Adv. Mater.* 2021, 33, 2105301. <https://doi.org/10.1002/adma.202105301>
153. Li, Q.; Wang, L.-M.; Liu, S.; Guo, L.; Dong, S.; Ma, G.; Cao, Z.; Zhan, X.; Gu, X.; Zhu, T.; Cai, Y.-P.; Huang, F. Vertical Composition Distribution and Crystallinity Regulations Enable High-Performance Polymer Solar Cells with >17% Efficiency. *ACS Energy Lett.* 2020, 5, 3637–3646. <https://doi.org/10.1021/acsenerylett.0c01927>

154. Wang, W.; Song, L.; Magerl, D.; González, D.M.; Körstgens, V.; Philipp, M.; Moulin, J.-F.; Müller-Buschbaum, P. Influence of Solvent Additive 1,8-Octanedithiol on P3HT:PCBM Solar Cells. *Adv. Funct. Mater.* 2018, 28, 1800209. <https://doi.org/10.1002/adfm.201800209>
155. McDowell, C.; Abdelsamie, M.; Toney, M.F.; Bazan, G.C. Solvent Additives: Key Morphology-Directing Agents for Solution-Processed Organic Solar Cells. *Adv. Mater.* 2018, 30, 1707114. <https://doi.org/10.1002/adma.201707114>
156. Peet, J.; Kim, J.Y.; Coates, N.E.; Ma, W.L.; Moses, D.; Heeger, A.J.; Bazan, G.C. Efficiency enhancement in low-bandgap polymer solar cells by processing with alkane dithiols. *Nature Mater.* 2007, 6, 497–500. <https://doi.org/10.1038/nmat1928>
157. Lee, J.K.; Ma, W.L.; Brabec, C.J.; Yuen, J.; Moon, J.S.; Kim, J.Y.; Lee, K.; Bazan, G.C.; Heeger, A.J. Processing Additives for Improved Efficiency from Bulk Heterojunction Solar Cells. *J. Am. Chem. Soc.* 2008, 130, 3619–3623. <https://doi.org/10.1021/ja710079w>
158. Chen, Y.; Zhang, X.; Zhan, C.; Yao, J. Origin of Effects of Additive Solvent on Film-Morphology in Solution-Processed Nonfullerene Solar Cells. *ACS Appl. Mater. Interfaces* 2015, 7, 6462–6471. <https://doi.org/10.1021/am507581w>
159. Liang, P.-W.; Liao, C.-Y.; Chueh, C.-C.; Zuo, F.; Williams, S.T.; Xin, X.-K.; Lin, J.; Jen, A.K.-Y. Additive Enhanced Crystallization of Solution-Processed Perovskite for Highly Efficient Planar-Heterojunction Solar Cells. *Adv. Mater.* 2014, 26, 3748–3754. <https://doi.org/10.1002/adma.201400231>
160. Song, X.; Wang, W.; Sun, P.; Ma, W.; Chen, Z.-K. Additive to regulate the perovskite crystal film growth in planar heterojunction solar cells. *Appl. Phys. Lett.* 2015, 106, 033901. <https://doi.org/10.1063/1.4906073>
161. Peng, L.; Xie, W.; Yang, C. Study of the effect of DIO additive on charge extraction and recombination in organic–inorganic hybrid MAPbI₃–xCl_x perovskite solar cell. *RSC Adv.* 2018, 8, 40298–40307. <https://doi.org/10.1039/C8RA08563C>
162. Tsai, C.-H.; Lin, C.-M.; Kuei, C.-H. Improving the performance of perovskite solar cells by adding 1,8-diiodooctane in the CH₃NH₃PbI₃ perovskite layer. *Solar Energy* 2018, 176, 178–185. <https://doi.org/10.1016/j.solener.2018.10.037>
163. Ghorai, A.; Mahato, S.; Singh, S.; Bose, S.; Roy, B.; Jeong, U.; Ray, S. K. Ligand-Mediated Revival of Degraded α -CsPbI₃ to Stable Highly Luminescent

- Perovskite. *Angew. Chem. Int. Ed.* 2023, 62, e202302852.
<https://doi.org/10.1002/anie.202302852>
164. Welyab, G.; Abebe, M.; Mani, D.; Thankappan, A.; Thomas, S.; Aga, F.G.; Kim, J.Y. All-Inorganic CsPbBr₃ Perovskite Nanocrystals Synthesized with Olive Oil and Oleylamine at Room Temperature. *Micromachines* 2023, 14, 1332.
<https://doi.org/10.3390/mi14071332>
165. Gutmann, V. Solvent effects on the reactivities of organometallic compounds. *Coord. Chem. Rev.* 1976, 18, 225-255. [https://doi.org/10.1016/S0010-8545\(00\)82045-7](https://doi.org/10.1016/S0010-8545(00)82045-7)
166. Belmares, M.; Blanco, M.; Goddard III, W.A.; Ross, R.B.; Caldwell, G.; Chou, S.-H.; Pham, J.; Olofson, P.M.; Thomas, C. Hildebrand and Hansen solubility parameters from molecular dynamics with applications to electronic nose polymer sensors. *J. Comput. Chem.* 2004, 25, 1814-1826.
<https://doi.org/10.1002/jcc.20098>
167. Krevelen, D.W.V.; Nijenhuis, K.T. *Properties of Polymers*, 4th ed.; Elsevier Science Ltd, Amsterdam, Netherlands, 2009.
168. Yao, K.; Xu, Y.-X.; Wang, X.; Li, F.; Yuan, J. The critical role of additives in binary halogen-free solvent systems for the general processing of highly efficient organic solar cells. *RSC Adv.* 2015, 5, 93689-93696.
<https://doi.org/10.1039/C5RA19850J>
169. Salim, T.; Wong, L.H.; Bräuer, B.; Kukreja, R.; Foo, Y.L.; Bao, Z.; Lam, Y.M. Solvent additives and their effects on blend morphologies of bulk heterojunctions. *J. Mater. Chem.* 2011, 21, 242-250.
<https://doi.org/10.1039/C0JM01976C>
170. Zhang, S.; Wu, S.; Chen, W.; Zhu, H.; Xiong, Z.; Yang, Z.; Chen, C.; Chen, R.; Han, L.; Chen, W. Solvent engineering for efficient inverted perovskite solar cells based on inorganic CsPbI₂Br light absorber. *Mater. Today Energy* 2018, 8, 125-133. <https://doi.org/10.1016/j.mtener.2018.03.006>
171. Flory, P.J. *Principles of Polymer Chemistry*; Cornell University Press: Ithaca, NY, USA, 1953.
172. Kim, J.Y. Phase Diagrams of Ternary π -Conjugated Polymer Solutions for Organic Photovoltaics. *Polymers* 2021, 13, 983.
<https://doi.org/10.3390/polym13060983>

173. Kim, J.Y. Phase Diagrams of Binary Low Bandgap Conjugated Polymer Solutions and Blends. *Macromolecules* 2019, 52, 4317–4328. <https://doi.org/10.1021/acs.macromol.9b00477>
174. Awol, N.; Amente, C.; Verma, G.; Kim, J.Y. A versatile lead iodide particle synthesis and film surface analysis for optoelectronics. *J. Alloys Compd.* 2020, 829, 154486. <https://doi.org/10.1016/j.jallcom.2020.154486>
175. Yan, K.; Long, M.; Zhang, T.; Wei, Z.; Chen, H.; Yang, S.; Xu, J. Hybrid Halide Perovskite Solar Cell Precursors: Colloidal Chemistry and Coordination Engineering behind Device Processing for High Efficiency. *J. Am. Chem. Soc.* 2015, 137, 13, 4460–4468. <https://doi.org/10.1021/jacs.5b00321>
176. Petrov, A.A.; Ordinartsev, A.A.; Fateev, S.A.; Goodilin, E.A.; Tarasov, A.B. Solubility of Hybrid Halide Perovskites in DMF and DMSO. *Molecules* 2021, 26, 7541. <https://doi.org/10.3390/molecules26247541>
177. Satta, J.; Casu, A.; Chiriu, D.; Carbonaro, C.M.; Stagi, L.; Ricci, P.C. Formation Mechanisms and Phase Stability of Solid-State Grown CsPbI₃ Perovskites. *Nanomaterials* 2021, 11, 1823. <https://doi.org/10.3390/nano11071823>
178. Kim, J.Y.; Nagamani, S.; Liu, L.; Elghazaly, A.H.; Solin, N.; Inganäs, O. A DNA and Self-Doped Conjugated Polyelectrolyte Assembled for Organic Optoelectronics and Bioelectronics. *Biomacromolecules* 2020, 21, 1214–1221. <https://doi.org/10.1021/acs.biomac.9b01667>
179. Straus, D.B.; Guo, S.; Cava, R.J. Kinetically Stable Single Crystals of Perovskite-Phase CsPbI₃. *J. Am. Chem. Soc.* 2019, 141, 29, 11435–11439. <https://doi.org/10.1021/jacs.9b06055>
180. Bhaumik, S.; Bruno, A.; Mhaisalkar, S. Broadband emission from zero-dimensional Cs₄PbI₆ perovskite nanocrystals. *RSC Adv.* 2020, 10, 13431–13436. <https://doi.org/10.1039/D0RA00467G>
181. Satta, J.; Casu, A.; Chiriu, D.; Carbonaro, C.M.; Stagi, L.; Ricci, P.C. Formation Mechanisms and Phase Stability of Solid-State Grown CsPbI₃ Perovskites. *Nanomaterials* 2021, 11, 1823. <https://doi.org/10.3390/nano11071823>
182. Leung, T.L.; Ahmad, I.; Syed, A.A.; Ng, A.M.C.; Popović, J.; Djurišić, A.V. Stability of 2D and quasi-2D perovskite materials and devices. *Commun. Mater.* 2022, 3, 63. <https://doi.org/10.1038/s43246-022-00285-9>

183. Wang, Y.; Zhang, T.; Kan, M.; Li, Y.; Wang, T.; Zhao, Y. Efficient a-CsPbI₃ Photovoltaics with Surface Terminated Organic Cations. *Joule* 2018, 2, 2065-2075. <https://doi.org/10.1016/j.joule.2018.06.013>
184. Yousaf, T.; Shahzad, N.; Sattar, A.; Tariq, M.A.; Hussain, N.; Khan, Z.S.; Javed, S.; Shahzad, M.I.; Pugliese, D. Performance of Cs-Doped Carbon-Based Perovskite Solar Cells in Ambient Environment. *Energies* 2023, 16(12), 4748.
185. Doumon, N.Y.; Wang, G.; Qiu, X.; Minnaard, A.J.; Chiechi, R.C.; Anton, L.J. 1,8-diiodooctane acts as a photo-acid in organic solar cells. *Sci. Rep.* 2019, 9, 4350. <https://doi.org/10.1038/s41598-019-40948-1>
186. Wu, Y.; Wang, Y.; Duan, J.; Yang, X.; Zhang, J.; Liu, L.; Tang, Q. Cluster effect of additives in precursors for inorganic perovskites solar cells. *Electrochim. Acta*, 2019, 331, 135379. <https://doi.org/10.1016/j.electacta.2019.135379>
187. Li, B.; Zhang, Y.; Fu, L.; Yu, T.; Zhou, S.; Zhang, L.; Yin, L. Surface passivation engineering strategy to fully-inorganic cubic CsPbI₃ perovskites for high-performance solar cells. *Nat. Commun.* 2018, 9, 1076. <https://doi.org/10.1038/s41467-018-03169-0>
188. Cavallini, M.; Bracali, M.; Aloisi, G.; Guidelli, R. Electrochemical STM Investigation of 1,8-Octanedithiol Self-Assembled Monolayers on Ag(111) in Aqueous Solution. *Langmuir* 1999, 15, 3003–3006. <https://doi.org/10.1021/la9815392>
189. Kim, Y.G.; Kim, T.-Y.; Oh, J.H.; Choi, K.S.; Kim, Y.-J.; Kim, S.Y. Cesium lead iodide solar cells controlled by annealing temperature. *Phys. Chem. Chem. Phys.* 2017, 19, 6257-6263. <https://doi.org/10.1039/C6CP08177K>
190. Tauc, J. Optical properties and electronic structure of amorphous Ge and Si. *Mater. Res. Bull.* 1968, 3, 37–46. [https://doi.org/10.1016/0025-5408\(68\)90023-8](https://doi.org/10.1016/0025-5408(68)90023-8)
191. Zhang, L.; Sun, C.; He, T.; Jiang, Y.; Wei, J.; Huang, Y.; Yuan, M. High-performance quasi-2D perovskite light-emitting diodes: from materials to devices. *Light Sci. Appl.* 2021, 10, 61. <https://doi.org/10.1038/s41377-021-00501-0>
192. Leung, T.L.; Ahmad, I.; Syed, A.A.; Ng, A.M.C.; Popović, J.; Djurišić, A.V. Stability of 2D and quasi-2D perovskite materials and devices. *Commun. Mater.* 2022, 3, 63. <https://doi.org/10.1038/s43246-022-00285-9>
193. Sheng, X.; Li, Y.; Xia, M.; Shi, E. Quasi-2D halide perovskite crystals and their optoelectronic applications. *J. Mater. Chem. A*, 2022, 10, 19169-19183. <https://doi.org/10.1039/D2TA02219B>

194. Kim, J.Y.; Yoo, Y.; Kim, J.; Park, H.J.; Cho, W.; Lee, S.; Sung, Y.-E.; Bae, B. Phase Behavior of Quasi-2D Hybrid Lead Bromide Perovskite Precursor Solutions. *ACS Appl. Opt. Mater.* 2024, 2, 108–117.
195. Zhou, S.; Zhou, G.; Li, Y.; Xu, X.; Hsu, Y.J.; Xu, J.; Zhao, N.; Lu, X. Understanding Charge Transport in All-Inorganic Halide Perovskite Nanocrystal Thin-Film Field Effect Transistors. *ACS Energy Lett.* 2020, 5, 2614–2623.
196. Ahmadi, M.; Wu, T.; Hu, B. A Review on Organic–Inorganic Halide Perovskite Photodetectors: Device Engineering and Fundamental Physics. *Adv. Mater.* 2017, 29, 1605242.
197. Ai, B.; Fan, Z.; Wong, Z.J. Plasmonic–perovskite solar cells, light emitters, and sensors. *Microsyst. Nanoeng.* 2022, 8, 5.
198. Kojima, A.; Teshima, K.; Shirai, Y.; Miyasaka, T. Organometal halide perovskites as visible-light sensitizers for photovoltaic cells. *J. Am. Chem. Soc.* 2009, 131, 6050–6051.
199. Lee, M.M.; Teuscher, J.; Miyasaka, T.; Murakami, T.N.; Snaith, H.J. Efficient hybrid solar cells based on meso-superstructured organometal halide perovskites. *Science* 2012, 338, 643–647.
200. Chen, W.; Wu, Y.; Yue, Y.; Liu, J.; Zhng, W.; Yang, X.; Chen, H.; Bi, E.; Ashraful, I.; Grätzel, M.; Han, L. Efficient and stable large-area perovskite solar cells with inorganic charge extraction layers. *Science* 2015, 350, 944–948.
201. Park, J.; Kim, J.; Yun, H.-S.; Paik, M.J.; Noh, E.; Mun, H.J.; Kim, M.G.; Shin, T.J.; Seok, S.I. Controlled growth of perovskite layers with volatile alkylammonium chlorides. *Nature* 2023, 616, 724–730.
202. Tan, Q.; Li, Z.; Luo, G.; Zhang, X.; Che, B.; Chen, G.; Gao, H.; He, D.; Ma, G.; Wang, J.; Xiu, J.; Yi, H.; Chen, T.; He, Z. Inverted perovskite solar cells using dimethylacridine-based dopants. *Nature* 2023, 620, 545–551.
203. Duan, L.; Walter, D.; Chang, N.; Bullock, J.; Kang, D.; Phang, S.P.; Weber, K.; White, T.; Macdonald, D.; Catchpole, K.; Shen, H. Stability challenges for the commercialization of perovskite–silicon tandem solar cells. *Nat. Rev. Mater.* 2023, 8, 261–281.
204. Kulbak, M.; Cahen, D.; Hodes, G. How Important Is the Organic Part of Lead Halide Perovskite Photovoltaic Cells? Efficient CsPbBr₃ Cells. *J. Phys. Chem. Lett.* 2015, 6, 2452–2456.

205. Eperon, G.E.; Paterno, G.M.; Sutton, R.J.; Zampetti, A.; Haghighirad, A.A.; Cacialli, F.; Snaith, H.J. Inorganic caesium lead iodide perovskite solar cells. *J. Mater. Chem. A* 2015, *3*, 19688-19695.
206. Alaei, A.; Circelli, A.; Yuan, Y.; Yang, Y.; Lee, S.S. Polymorphism in metal halide perovskites. *Mater. Adv.* 2021, *2*, 47-63.
207. Liu, X.; Li, J.; Cui, X.; Wang, X.; Yang, D. The progress and efficiency of CsPbI₂Br perovskite solar cells. *J. Mater. Chem. C* 2023, *11*, 426-455.
208. Lim, E.L.; Yang, J.; Wei, Z. Inorganic CsPbI₂Br halide perovskites: from fundamentals to solar cell optimizations. *Energy Environ. Sci.* 2023, *16*, 862-888.
209. Huang, J.; Zhou, D.; Yan, H.; Meng, C.; Yang, Y.; Liu, J.; Wang, M.; Xu, P.; Peng, Z.; Chen, J.; Li, G. A multiple-coordination framework for CsPbI₂Br perovskite solar cells. *J. Mater. Chem. C* 2024, *12*, 4112-4122.
210. Jeong, M.J.; Jeon, S.W.; Kim, S.Y.; Noh, J.H. High Fill Factor CsPbI₂Br Perovskite Solar Cells Via Crystallization Management. *Adv. Energy Mater.* 2023, *13*, 2300698.
211. Ding, Y.; Guo, Q.; Geng, Y.; Dai, Z.; Wang, Z.; Chen, Z.; Guo, Q.; Zheng, Z.; Li, Y.; Zhou, E. A low-cost hole transport layer enables CsPbI₂Br single-junction and tandem perovskite solar cells with record efficiencies of 17.8 % and 21.4 %. *Nano Today* 2022, *46*, 101586.
212. Zhu, M.; Qin, L.; Xia, Y.; Liang, J.; Wang, Y.; Hong, D.; Tian, Y.; Tie, Z.; Jin, Z. Antimony doped CsPbI₂Br for high-stability all-inorganic perovskite solar cells. *Nano Res.* 2024, *17*, 1508–1515.
213. Ma, P.; Bie, T.; Liu, Y.; Yang, L.; Bi, S.; Wang, Z.; Shao, M. Zirconium Doping to Enable High-Efficiency and Stable CsPbI₂Br All-Inorganic Perovskite Solar Cells. *ACS Appl. Mater. Interfaces* 2024, *16*, 1217–1224.
214. Han, Y.; Zhao, H.; Duan, C.; Yang, S.; Yang, Z.; Liu, Z.; Liu, S. F. Controlled n-Doping in Air-Stable CsPbI₂Br Perovskite Solar Cells with a Record Efficiency of 16.79% . *Adv. Funct. Mater.* 2020, *30*, 1909972.
215. Zhang, W.; Xiong, J.; Li, J.; Daoud, W.A. Guanidinium Passivation for Air-Stable Rubidium- Incorporated Cs(1-x)RbxPbI₂Br Inorganic Perovskite Solar Cells. *Sol. RRL* 2020, *4*, 2000112.
216. Guo, Z.; Zhao, S.; Liu, A.; Kamata, Y.; Teo, S.; Yang, S.; Xu, Z.; Hayase, S.; Ma, T. Niobium Incorporation into CsPbI₂Br for Stable and Efficient All-

- Inorganic Perovskite Solar Cells. *ACS Appl. Mater. Interfaces* 2019, 11, 19994–20003.
217. Yang, F.; Hirotsu, D.; Kapil, G.; Kamarudin, M.A.; Ng, C.H.; Zhang, Y.; Shen, Q.; Hayase, S. All-Inorganic CsPb_{1-x}GexI₂Br Perovskite with Enhanced Phase Stability and Photovoltaic Performance. *Angew. Chem. Int. Ed.* 2018, 57, 12745-12749.
 218. Liu, C.; Li, W.; Li, H.; Wang, H.; Zhang, C.; Yang, Y.; Gao, X.; Xue, Q.; Yip, H.-Y.; Fan, J.; Schropp, R.E.I.; Mai, Y. Structurally Reconstructed CsPbI₂Br Perovskite for Highly Stable and Square-Centimeter All-Inorganic Perovskite Solar Cells. *Adv. Energy Mater.* 2019, 9, 1803572.
 219. Duan, J.; Zhao, Y.; Yang, X.; Wang, Y.; He, B.; Tang, Q. Lanthanide Ions Doped CsPbBr₃ Halides for HTM-Free 10.14%-Efficiency Inorganic Perovskite Solar Cell with an Ultrahigh Open-Circuit Voltage of 1.594 V. *Adv. Energy Mater.* 2018, 8, 1802346.
 220. Lau, C.F.J.; Zhang, M.; Deng, X.; Zheng, J.; Bing, J.; Ma, Q.; Kim, J.; Hu, L.; Green, M.A.; Huang, S.; Ho-Baillie, A. Strontium-Doped Low-Temperature-Processed CsPbI₂Br Perovskite Solar Cells. *ACS Energy Lett.* 2017, 2, 2319–2325.
 221. Swarnkar, A.; Mir, W.J.; Nag, A. Can B-Site Doping or Alloying Improve Thermal- and Phase-Stability of All-Inorganic CsPbX₃ (X = Cl, Br, I) Perovskites? *ACS Energy Lett.* 2018, 3, 286–289.
 222. Chen, S.; Liu, X.; Wang, Z.; Li, W.; Gu, X.; Lin, J.; Yang, T.; Gao, X.; Kyaw, A.K.K. Defect Passivation of CsPbBr₃ with AgBr for High-Performance All-Inorganic Perovskite Solar Cells. *Advanced Energy & Sustainability Research* 2021, 2, 2000099.
 223. Gutmann, V. Solvent effects on the reactivities of organometallic compounds. *Coord. Chem. Rev.* 1976, 18, 225–255.
 224. Petrov, A.A.; Ordinartsev, A.A.; Fateev, S.A.; Goodilin, E.A.; Tarasov, A.B. Solubility of Hybrid Halide Perovskites in DMF and DMSO. *Molecules* 2021, 26, 7541.
 225. Jeon, N.J.; Noh, J.H.; Kim, Y.C.; Yang, W.S.; Ryu, S.; Seok, S.I. Solvent engineering for high-performance inorganic–organic hybrid perovskite solar cells. *Nature Mater.* 2014, 13, 897–903.
 226. Hansen, C.M. *Hansen Solubility Parameters – A User’s Handbook*; CRC Press: Boca Raton, FL, 2000.

227. Hansen, C.M. 50 Years with solubility parameters—past and future. *Prog. Org. Coat.* 2004, *51*, 77-84.
228. G. Kresse, G.; Furthmüller, J. Efficient iterative schemes for ab initio total-energy calculations using a plane-wave basis set. *Phys. Rev. B* 1996, *54*, 11169-11186.
229. Perdew, J.P.; Burke, K.; Ernzerhof, M. Generalized Gradient Approximation Made Simple. *Phys. Rev. Lett.* 1997, *77*, 3865–3868.
230. Chen, Y.; Shi, T.; Liu, P.; Xie, W.; Chen, K.; Xu, X.; Shui, L.; Shang, C.; Chen, Z.; Yip, H.-L.; Zhou, G.; Wang, X. The distinctive phase stability and defect physics in CsPbI₂Br perovskite. *J. Mater. Chem. A* 2019, *7*, 20201-20207.
231. Shannon, R.D. Revised Effective Ionic Radii and Systematic Studies of Interatomic Distances in Halides and Chalcogenides. *Acta Cryst.* 1976, *A32*, 751-767.
232. Wang, B.; Novendra, N.; Navrotsky, A. Energetics, Structures, and Phase Transitions of Cubic and Orthorhombic Cesium Lead Iodide (CsPbI₃) Polymorphs. *J. Am. Chem. Soc.* 2019, *141*, 14501–14504.
233. Li, Z.; Yang, M.; Park, J.-S.; Wei, S.-W.; Berry, J.J.; Zhu, K. Stabilizing Perovskite Structures by Tuning Tolerance Factor: Formation of Formamidinium and Cesium Lead Iodide Solid-State Alloys. *Chem. Mater.* 2016, *28*, 1, 284–292
234. Kebede, T.; Abebe, M.; Mani, D.; Paduvilan, J.K.; Thottathi, L.; Thankappan, A.; Thomas, S.; Kamangar, S.; Shaik, A.S.; Badruddin, I.A.; et al. Phase Behavior and Role of Organic Additives for Self-Doped CsPbI₃ Perovskite Semiconductor Thin Films. *Micromachines* 2023, *14*, 1601.
235. Idosa, D.A.; Abebe, M.; Mani, D.; Thankappan, A.; Thomas, S.; Aga, F.G.; Kim, J.Y. A Blue-Light-Emitting 3 nm-Sized CsPbBr₃ Perovskite Quantum Dot with ZnBr₂ Synthesized by Room-Temperature Supersaturated Recrystallization. *Photonics* 2023, *10*, 802.
236. Xu, W.; He, F.; Zhang, M.; Nie, P.; Zhang, S.; Zhao, C.; Luo, R.; Li, J.; Zhang, X.; Zhao, S.; Li, W.-D.; Kang, F.; Nan, C.-W.; Wei, G. Minimizing Voltage Loss in Efficient All-Inorganic CsPbI₂Br Perovskite Solar Cells through Energy Level Alignment. *ACS Energy Lett.* 2019, *4*, 2491–2499.
237. Lu, J.; Chen, S.C.; Zheng, Q. Defect passivation of CsPbI₂Br perovskites through Zn(II) doping: toward efficient and stable solar cells. *Sci. China Chem.* 2019, *62*, 1044–1050.

238. Zeng, Z.; Zhang, J.; Gan, X.; Sun, H.; Shang, M.; Hou, D.; Lu, C.; Chen, R.; Zhu, Y.; Han, L. In Situ Grain Boundary Functionalization for Stable and Efficient Inorganic CsPbI₂Br Perovskite Solar Cells. *Adv. Energy Mater.* 2018, 8, 1801050.
239. Yan, D.; Shi, T.; Zang, Z.; Zhou, T.; Liu, Z.; Zhang, Z.; Du, J.; Leng, Y.; Tang, X. *Small* 2019, 15, 1901173.
240. Zhang, Y.; Li G.; She, C.; Liu, S.; Yue, F.; Jing, C.; Cheng, Y.; Chu, J. *Nano Res.* 2021, 14, 2770–2775.
241. Shockley, W.; Queisser H.J. *J. Appl. Phys.* 1961, 32, 510-519.
242. Ravi, V.K.; Markad, G.B.; Nag, A. Band Edge Energies and Excitonic Transition Probabilities of Colloidal CsPbX₃ (X = Cl, Br, I) Perovskite Nanocrystals. *ACS Energy Lett.* 2016, 1, 665–671.
243. Schrader, B. *Infrared and Raman Spectroscopy: Methods and Applications*; VCH: Weinheim, Germany, 1995.
244. Awol, N.; Amente, C.; Verma, G.; Kim, J.Y. Morphology and surface analyses for CH₃NH₃PbI₃ perovskite thin films treated with versatile solvent–antisolvent vapors. *RSC Adv.* 2021, 11, 17789.
245. Chen, Q.; Lin, L.; Wang, Y.; Gao, Z.; Fu, Y.; Liu, Q.; Li, J.; He, D. Enhancement of photoelectric performance for CsPbI₂Br solar cells by the synergistic effect of binary additives. *J. Materiomics* 2023, 9, 27-34.
246. Li, D.; Neumann, A. W. A Reformulation of the Equation of State for Interfacial Tensions. *J. Colloid Interface Sci.* 1990, 137, 304-307.
247. Nilsson, S.; Bernasik, A.; Budkowski, A.; Moons, E. Morphology and Phase Separation of Spin-Coated Films of Polyfluorene/PCBM Blends. *Macromolecules* 2007, 40, 8291-8301.
248. Kim, J.Y. Order–Disorder Phase Equilibria of Regioregular Poly(3-hexylthiophene-2,5-diyl) Solution. *Macromolecules* 2018, 51, 9026–9034.
249. Kim, J.Y. Phase Diagrams of Binary Low Bandgap Conjugated Polymer Solutions and Blends. *Macromolecules* 2019, 52, 4317–4328.
250. Kleiman, M.; Ryu, K.A.; Esser-Kahn, A.P. Determination of Factors Influencing the Wet Etching of Polydimethylsiloxane Using Tetra-n-butylammonium Fluoride. *Macromol. Chem. Phys.* 2016, 217, 284-291.
251. Atourki, L.; Bernabe, M.; Makha, M.; Bouabid, K.; Regragui, M.; Ihlal, A.; Abd-lefdil, M.; Mollar, M. Effect of doping on the phase stability and

- photophysical properties of CsPbI₂Br perovskite thin films. *RSC Adv.* 2021, *11*, 1440-1449.
252. Zhou, Y.; Chen, J.; Bakr, O. M.; Sun, H. T. Metal-Doped Lead Halide Perovskites: Synthesis, Properties, and Optoelectronic Applications. *Chem. Mater.* 2018, *30* (19), 6589–6613. <https://doi.org/10.1021/acs.chemmater.8b02989>.
253. Samadpour, M.; Golchini, A.; Abdizadeh, K.; Heydari, M.; Forouzandeh, M.; Saki, Z.; Taghavinia, N. Modified Antisolvent Method for Improving the Performance and Stability of Triple-Cation Perovskite Solar Cells. *ACS Omega* 2021, *6* (1), 172–179. <https://doi.org/10.1021/acsomega.0c04058>.
254. Choi, M. J.; Lee, Y. S.; Cho, I. H.; Kim, S. S.; Kim, D. H.; Kwon, S. N.; Na, S. I. Functional Additives for High-Performance Inverted Planar Perovskite Solar Cells with Exceeding 20% Efficiency: Selective Complexation of Organic Cations in Precursors. *Nano Energy* 2020, *71* (October 2019), 104639. <https://doi.org/10.1016/j.nanoen.2020.104639>.
255. Shi, M.; Li, R.; Li, C. Halide Perovskites for Light Emission and Artificial Photosynthesis: Opportunities, Challenges, and Perspectives. *EcoMat* 2021, *3* (1), 1–26. <https://doi.org/10.1002/eom2.12074>.
256. Koech, R. K.; Ichwani, R.; Martin, J. L.; Oyewole, D. O.; Oyelade, O. V.; Olanrewaju, Y. A.; Sanni, D. M.; Adeniji, S. A.; Grimm, R. L.; Bello, A.; Oyewole, O. K.; Ntsoenzok, E.; Soboyejo, W. O. A Study of the Effects of a Thermally Evaporated Nanoscale CsBr Layer on the Optoelectronic Properties and Stability of Formamidinium-Rich Perovskite Solar Cells. *AIP Adv.* 2021, *11* (9), 11ENG. <https://doi.org/10.1063/5.0064398>.
257. Qiao, H. W.; Chen, M.; Zhou, Z.; Cheng, Q.; Hou, Y.; Yang, H. G. Improved Photovoltaic Performance of CsPbI₂Br Perovskite Films via Bivalent Metal Chloride Doping. *Front. Energy Res.* 2021, *9*. <https://doi.org/10.3389/fenrg.2021.692059>.
258. Zhu, W.; Zhang, Q.; Chen, D.; Zhang, Z.; Lin, Z.; Chang, J.; Zhang, J.; Zhang, C.; Hao, Y. Intermolecular Exchange Boosts Efficiency of Air-Stable, Carbon-Based All-Inorganic Planar CsPbI₂Br Perovskite Solar Cells to Over 9%. *Adv. Energy Mater.* 2018, *8* (30), 1–11. <https://doi.org/10.1002/aenm.201802080>.
259. He, J.; Su, J.; Di, J.; Lin, Z.; Zhang, S.; Ma, J.; Zhang, J.; Liu, S.; Chang, J.; Hao, Y. Surface Reconstruction Strategy Improves the All-Inorganic CsPbI₂Br

- Based Perovskite Solar Cells and Photodetectors Performance. *Nano Energy* 2022, 94. <https://doi.org/10.1016/j.nanoen.2022.106960>.
260. Ma, T.; Wang, S.; Zhang, Y.; Zhang, K.; Yi, L. The Development of All-Inorganic CsPbX₃ Perovskite Solar Cells. *J. Mater. Sci.* 2020, 55 (2), 464–479. <https://doi.org/10.1007/s10853-019-03974-y>.
261. Wen, Q.; Duan, C.; Zou, F.; Luo, D.; Li, J.; Liu, Z.; Wang, J.; Yan, K. All-Inorganic CsPb_{1-x}Sn_xI₂Br Perovskites Mediated by Dicyandiamide Additive for Efficient 4-Terminal Tandem Solar Cell. *Chem. Eng. J.* 2023, 452 (P4), 139697. <https://doi.org/10.1016/j.cej.2022.139697>.
262. Peng, K.; Yang, S.; Wu, Z.; Hsu, H. Synthesis of Red Cesium Lead Bromiodide Nanocrystals Chelating Phenylated Phosphine Ligands with Enhanced Stability. 2021. <https://doi.org/10.1021/acsomega.1c00910>
263. Montecucco, R.; Quadri, E.; Po, R.; Grancini, G. All-Inorganic Cesium-Based Hybrid Perovskites for Efficient and Stable Solar Cells and Modules. 2021, 2100672. <https://doi.org/10.1002/aenm.202100672>.
264. Li, L.; Wei, W.; Wang, J.; Peng, Y.; Zhu, X.; Zhao, X.; Su, M.; Wang, Y.; Sun, W. H. Lead Iodide and Cesium Lead Halide Perovskite Highly Oriented Films Deposited by Spin Coating. *AIP Adv.* 2020, 10 (10). <https://doi.org/10.1063/5.0011318>.
265. Parida, B.; Yoon, S.; Jeong, S. M.; Cho, J. S.; Kim, J. K.; Kang, D. W. Recent Progress on Cesium Lead/Tin Halide-Based Inorganic Perovskites for Stable and Efficient Solar Cells: A Review. *Sol. Energy Mater. Sol. Cells* 2020, 204 (September 2019), 110212. <https://doi.org/10.1016/j.solmat.2019.110212>.
266. Li, H.; Wang, Z.; Wang, L.; Chang, B.; Liu, Z.; Pan, L.; Wu, Y.; Yin, L. Dual-Passivation Strategy on CsPbI₂Br Perovskite Solar Cells for Reduced Voltage Deficit and Enhanced Stability. *Nano Energy* 2022, 103 (PA), 107792. <https://doi.org/10.1016/j.nanoen.2022.107792>.
267. Chen, S.; Liu, X.; Wang, Z.; Li, W.; Gu, X.; Lin, J.; Yang, T.; Gao, X.; Kyaw, A. K. K. Defect Passivation of CsPbBr₃ with AgBr for High-Performance All-Inorganic Perovskite Solar Cells. *Adv. Energy Sustain. Res.* 2021, 2(6), 2000099. <https://doi.org/10.1002/aesr.202000099>.
268. Rong, S. S.; Faheem, M. B.; Li, Y. B. Perovskite Single Crystals: Synthesis, Properties, and applications. *J. Electron. Sci. Technol.* 2021, 19(2), 1–18. <https://doi.org/10.1016/J.JNLEST.2021.100081>.

269. Chen, S.; Liu, X.; Wang, Z.; Li, W.; Gu, X.; Lin, J.; Yang, T.; Gao, X.; Kyaw, A. K. K. Defect Passivation of CsPbBr₃ with AgBr for High-Performance All-Inorganic Perovskite Solar Cells. *Adv. Energy Sustain. Res.* 2021, 2 (6), 2000099. <https://doi.org/10.1002/aesr.202000099>
270. Access, O. First-Principle Study of CsPbBr₃ and CsPbI₃ Perovskite Solar Cells. <https://doi.org/10.1149/2162-8777/ac5eb6>.
271. Li, Z.; Xu, J.; Zhou, S.; Zhang, B.; Liu, X.; Dai, S.; Yao, J.; Utilization, C.; Power, E. Perovskite Films at Low Temperature for Highly Efficient Planar Heterojunction Solar Cells. *ACS Appl. Mater. Interfaces* 2018, 3–7.
272. Yu, B.; Zhang, H.; Wu, J.; Li, Y.; Li, H.; Li, Y.; Shi, J.; Wu, H.; Li, D.; Luo, Y.; Meng, Q. Solvent-Engineering toward CsPb(IxBr1-x)₃ Films for High-Performance Inorganic Perovskite Solar Cells. *J. Mater. Chem. A* 2018, 6 (40), 19810–19816. <https://doi.org/10.1039/c8ta07968d>.
273. Gao, B.; Meng, J.; Lu, J.; Zhao, R. CH₃NH₃PbI₃ Perovskite Solar Cells with Efficiency over 22% Fabricated by Green Antisolvent Method. *Mater. Lett.* 2020, 274, 127995. <https://doi.org/10.1016/j.matlet.2020.127995>.
274. Samadpour, M.; Golchini, A.; Abdizadeh, K.; Heydari, M.; Forouzandeh, M.; Saki, Z.; Taghavinia, N. Modified Antisolvent Method for Improving the Performance and Stability of Triple-Cation Perovskite Solar Cells. *ACS Omega* 2021, 6 (1), 172–179. <https://doi.org/10.1021/acsomega.0c04058>.
275. Liu, J.; Li, N.; Jia, J.; Dong, J.; Qiu, Z.; Iqbal, S.; Cao, B. Perovskite Films Grown with Green Mixed Anti-Solvent for Highly Efficient Solar Cells with Enhanced Stability. *Sol. Energy* 2019, 181 (November 2018), 285–292. <https://doi.org/10.1016/j.solener.2019.02.020>.
276. Yang, H.; Wang, H.; Wang, K.; Liu, D.; Zhao, L.; Chen, D.; Zhu, W.; Zhang, J.; Zhang, C. Recent Progress of Film Fabrication Process for Carbon-Based All-Inorganic Perovskite Solar Cells. *Crystals* 2023, 13 (4). <https://doi.org/10.3390/cryst13040679>.
277. Yang, H.; Wang, H.; Zhang, J.; Chang, J.; Zhang, C. A Facile Way to Improve the Performance of Perovskite Solar Cells by Toluene and Diethyl Ether Mixed Anti-Solvent Engineering. 2019, 3–6.
278. Ghosh, S.; Mishra, S.; Singh, T. Antisolvents in Perovskite Solar Cells: Importance, Issues, and Alternatives. *Adv. Mater. Interfaces* 2020, 7 (18), 1–24. <https://doi.org/10.1002/admi.202000950>.

279. Eze, M. C.; Eze, H. U.; Ugwuanyi, G. N.; Alnajideen, M.; Atia, A.; Olisa, S. C.; Rocha, V. G.; Min, G. Improving the Efficiency and Stability of In-Air Fabricated Perovskite Solar Cells Using the Mixed Antisolvent of Methyl Acetate and Chloroform. *Org. Electron.* 2022, 107 (March), 106552. <https://doi.org/10.1016/j.orgel.2022.106552>.
280. Zhang, Z.; Wu, C.; Wang, D.; Liu, G.; Zhang, Q.; Luo, W.; Qi, X.; Guo, X.; Zhang, Y.; Lao, Y.; Qu, B.; Xiao, L.; Chen, Z. Improvement of Cs₂AgBiBr₆ Double Perovskite Solar Cell by Rubidium Doping. *Org. Electron.* 2019, 74, 204–210. <https://doi.org/10.1016/j.orgel.2019.06.037>.
281. Taylor, A. D.; Sun, Q.; Goetz, K. P.; An, Q.; Schramm, T.; Hofstetter, Y.; Litterst, M.; Paulus, F.; Vaynzof, Y. A General Approach to High-Efficiency Perovskite Solar Cells by Any Antisolvent. *Nat. Commun.* 2021, 12 (1), 1–11. <https://doi.org/10.1038/s41467-021-22049-8>.
282. Moot, T.; Marshall, A. R.; Wheeler, L. M.; Habisreutinger, S. N.; Schloemer, T. H.; Boyd, C. C.; Dikova, D. R.; Pach, G. F.; Hazarika, A.; McGehee, M. D.; Snaith, H. J.; Luther, J. M. CsI-Antisolvent Adduct Formation in All-Inorganic Metal Halide Perovskites. *Adv. Energy Mater.* 2020, 10 (9). <https://doi.org/10.1002/aenm.201903365>.
283. Zhang, L.; Hu, T.; Li, J.; Zhang, L.; Li, H.; Lu, Z.; Wang, G. All-Inorganic Perovskite Solar Cells With Both High Open-Circuit Voltage and Stability. *Front. Mater.* 2020, 6 (January), 1–8. <https://doi.org/10.3389/fmats.2019.00330>.
284. Choi, H.; Ke, C.; Skalsky, S.; Flavell, W. R.; Parkinson, P. Spatially and Temporally Resolved Degradation in Antisolvent Treated Perovskite Films; 2020; p 27. <https://doi.org/10.1117/12.2553682>.
285. Deng, W.; Li, F.; Li, J.; Wang, M.; Hu, Y.; Liu, M. Anti-Solvent Free Fabrication of FA-Based Perovskite at Low Temperature Towards to High-Performance Flexible Perovskite Solar Cells. *Nano Energy* 2020, 70 (October 2019), 104505. <https://doi.org/10.1016/j.nanoen.2020.104505>.
286. Ng, C. H.; Ripolles, T. S.; Hamada, K.; Teo, S. H.; Lim, H. N.; Bisquert, J.; Hayase, S. Tunable Open Circuit Voltage by Engineering Inorganic Cesium Lead Bromide/Iodide Perovskite Solar Cells. *Sci. Rep.* 2018, 8 (1), 1–9. <https://doi.org/10.1038/s41598-018-20228-0>.
287. Ho-Baillie, A.; Zhang, M.; Lau, C. F. J.; Ma, F. J.; Huang, S. Untapped Potentials of Inorganic Metal Halide Perovskite Solar Cells. *Joule*. Cell Press April

- 17, 2019, pp 938–955. <https://doi.org/10.1016/j.joule.2019.02.002>.
288. Johnston, A.; Walters, G.; Saidaminov, M. I.; Huang, Z.; Bertens, K.; Jalarvo, N.; Sargent, E. H. Bromine Incorporation and Suppressed Cation Rotation in Mixed-Halide Perovskites. *ACS Nano* 2020, *14* (11), 15107–15118. <https://doi.org/10.1021/acsnano.0c05179>.
289. Olaleru, S. A.; Kirui, J. K.; Wamwangi, D.; Jhamba, L.; Erasmus, R.; Mwakikunga, B.; Roro, K. Enhanced Optical Properties of Perovskite Thin Film through Material Optimization for Photovoltaic Application. *E3S Web Conf.* 2021, *239*, 1–15. <https://doi.org/10.1051/e3sconf/202123900020>.
290. Muradov, A.; Frolushkina, D.; Samusenkov, V.; Zhamanbayeva, G.; Kot, S. Methods of Stability Control of Perovskite Solar Cells for High Efficiency. *Energies* 2021, *14* (10). <https://doi.org/10.3390/en14102918>.
291. Eduard Aleksanyan, Ani Aprahamian, Alexander S. Mukasyan, Vachagan Harutyunyan¹, K. V. M. Mechanisms of Mechanochemical Synthesis of Cesium Lead Halides: Pathways toward Stabilization of α -CsPbI₃ Eduard. 1–26.
292. Faheem, M. B.; Khan, B.; Feng, C.; Farooq, M. U.; Raziq, F.; Xiao, Y.; Li, Y. All-Inorganic Perovskite Solar Cells: Energetics, Key Challenges, and Strategies toward Commercialization. *ACS Energy Lett.* 2020, *5* (1), 290–320. <https://doi.org/10.1021/acsenerylett.9b02338>.
293. Chen, Y.; Shi, T.; Liu, P.; Xie, W.; Chen, K.; Xu, X.; Shui, L.; Shang, C.; Chen, Z.; Yip, H. L.; Zhou, G.; Wang, X. The Distinctive Phase Stability and Defect Physics in CsPbI₂Br Perovskite. *J. Mater. Chem. A* 2019, *7* (35), 20201–20207. <https://doi.org/10.1039/c9ta04839a>.
294. Kumar, M.; Pawar, V.; Jha, P. K.; Jha, P. A.; Singh, P. Compositional Degradation with Br Content in Cesium Lead Halide CsPbBr_xI_{3-x}. *J. Solid State Chem.* 2022, *308* (January), 122893. <https://doi.org/10.1016/j.jssc.2022.122893>.
295. Rigter, S. A.; Quinn, X. L.; Kumar, R. E.; Fenning, D. P.; Massonnet, P.; Ellis, S. R.; Heeren, R. M. A.; Svane, K. L.; Walsh, A.; Garnett, E. C. Passivation Properties and Formation Mechanism of Amorphous Halide Perovskite Thin Films. *Adv. Funct. Mater.* 2021, *31* (15). <https://doi.org/10.1002/adfm.202010330>.
296. Lu, P.; Lu, M.; Wang, H.; Sui, N.; Shi, Z.; Yu, W. W.; Zhang, Y. Metal Halide Perovskite Nanocrystals and Their Applications in Optoelectronic Devices. *InfoMat* 2019, *1* (4), 430–459. <https://doi.org/10.1002/inf2.12031>.
297. Lv, L.; Xu, Y.; Fang, H.; Luo, W.; Xu, F.; Liu, L.; Wang, B.; Zhang, X.;

- Yang, D.; Hu, W.; Dong, A. Generalized Colloidal Synthesis of High-Quality, Two-Dimensional Cesium Lead Halide Perovskite Nanosheets and Their Applications in Photodetectors. *Nanoscale* 2016, 8 (28), 13589–13596. <https://doi.org/10.1039/c6nr03428d>.
298. Li, J.; Duan, J.; Yang, X.; Duan, Y.; Yang, P.; Tang, Q. Review on Recent Progress of Lead-Free Halide Perovskites in Optoelectronic Applications. *Nano Energy* 2021, 80, 105526. <https://doi.org/10.1016/j.nanoen.2020.105526>.
299. Yang, H.; Wang, H.; Wang, K.; Liu, D.; Zhao, L.; Chen, D.; Zhu, W.; Zhang, J.; Zhang, C. Recent Progress of Film Fabrication Process for Carbon-Based All-Inorganic Perovskite Solar Cells. *Crystals* 2023, 13, 679. <https://doi.org/10.3390/cryst13040679>.

Appendix

Supplementary Materials

Phase behaviour and Role of Organic Additives for Self-Doped CsPbI₃ Perovskite Semiconductor Thin Films

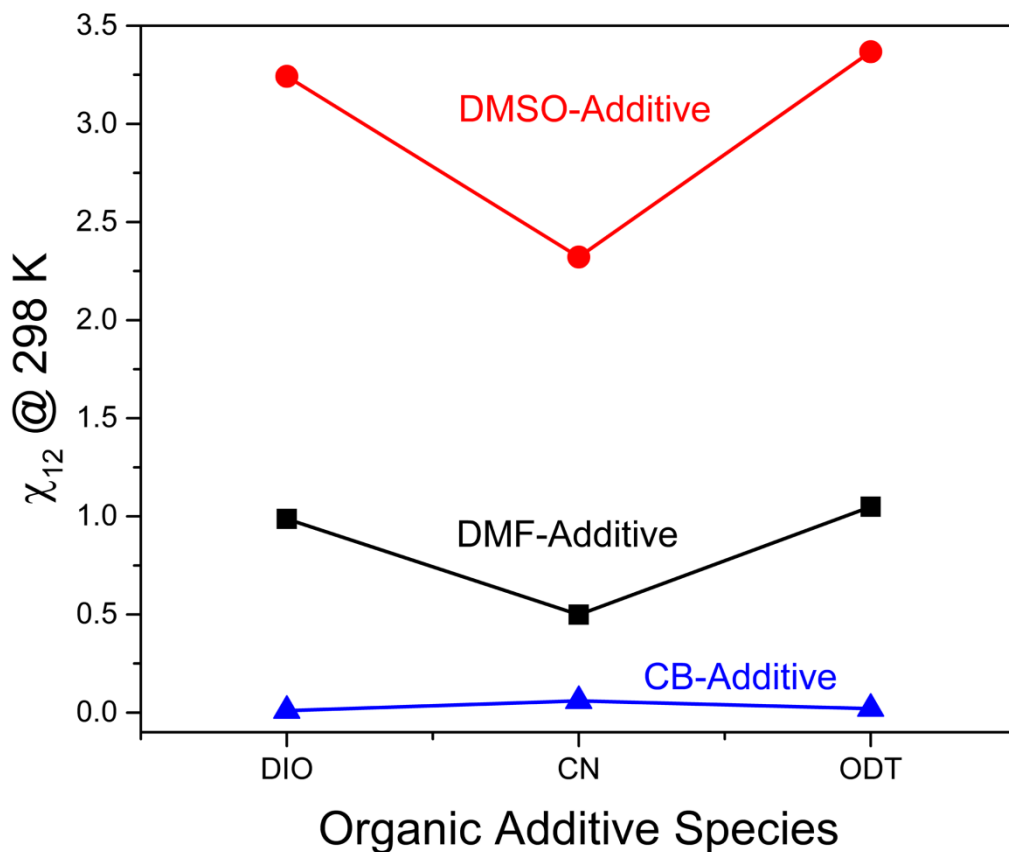


Figure S4.1. Flory-Huggins interaction parameter at 298 K as a function of organic additive species.

Table S4.1. Flory-Huggins χ_{12} interaction parameter at 298 K as a function of organic additive species.

	Binary additive-solvent system								
	DMF			DMSO			CB*		
	DIO	CN	ODT	DIO	CN	ODT	DIO	CN	ODT
χ_{12}	0.987	0.499	1.049	3.242	2.321	3.368	0.01	0.06	0.02

* Chlorobenzene (CB) is used as an antisolvent in this study.

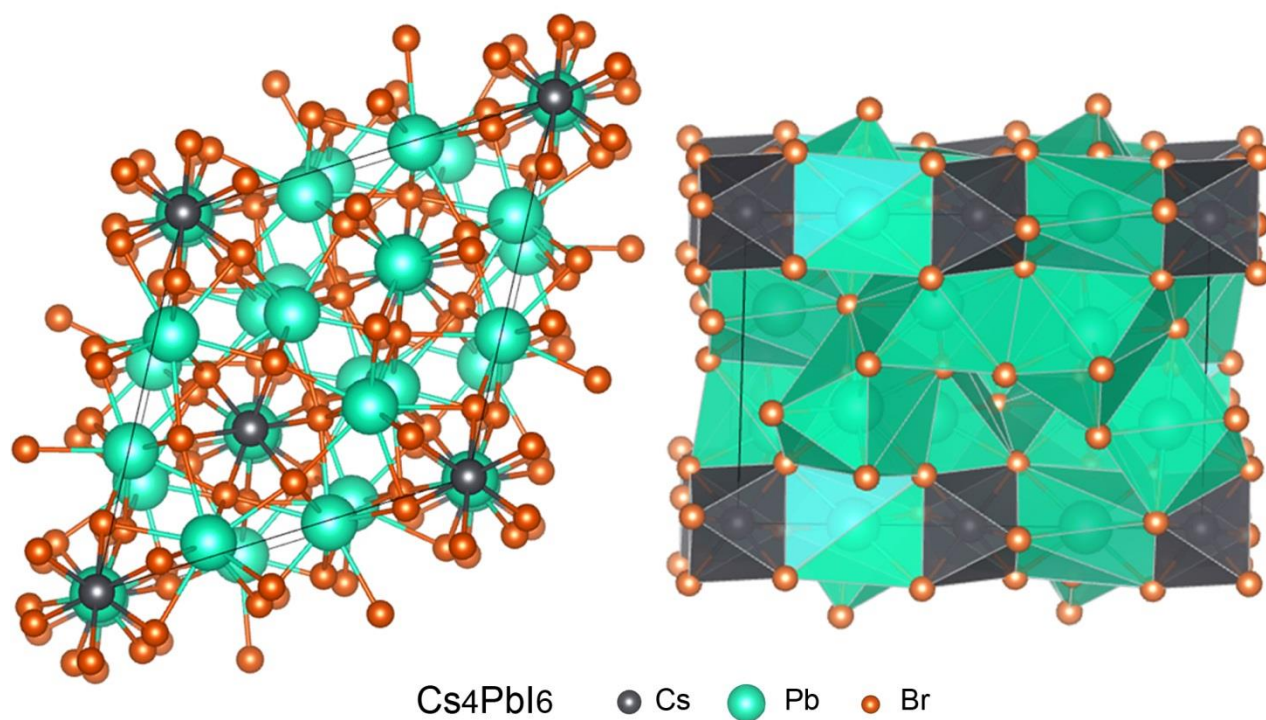


Figure S4.2. Crystal structure of trigonal Cs₄PbI₆ with space group R-3c.

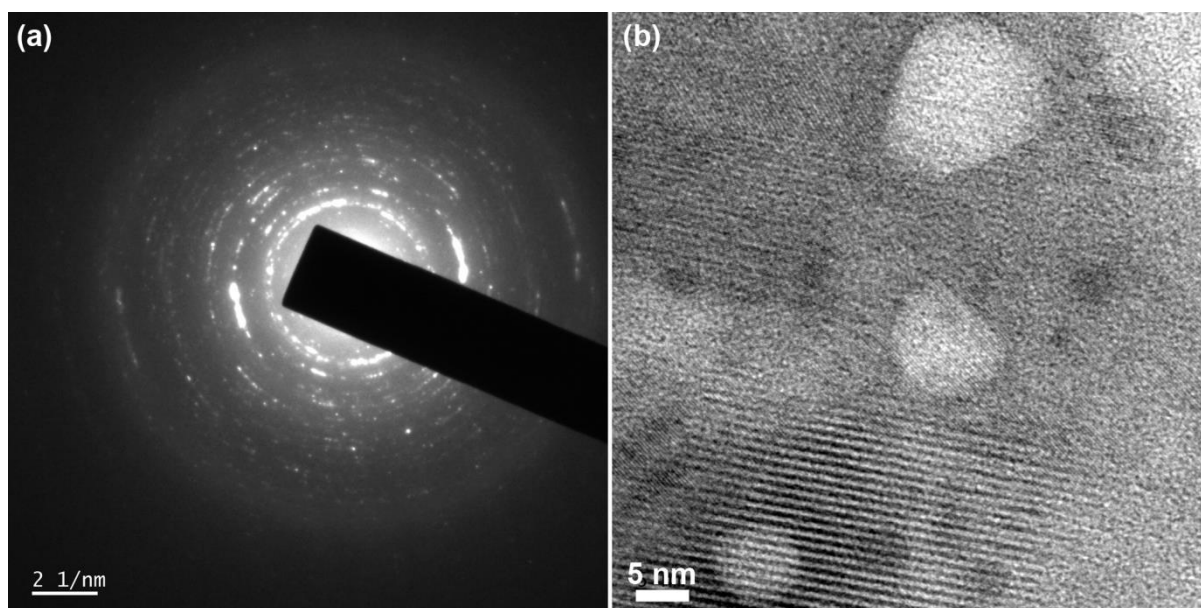


Figure S4.3. (a) Selected area diffraction pattern and (b) high-resolution TEM images of self-doped CsPbI₃ with the organic additive ODT.

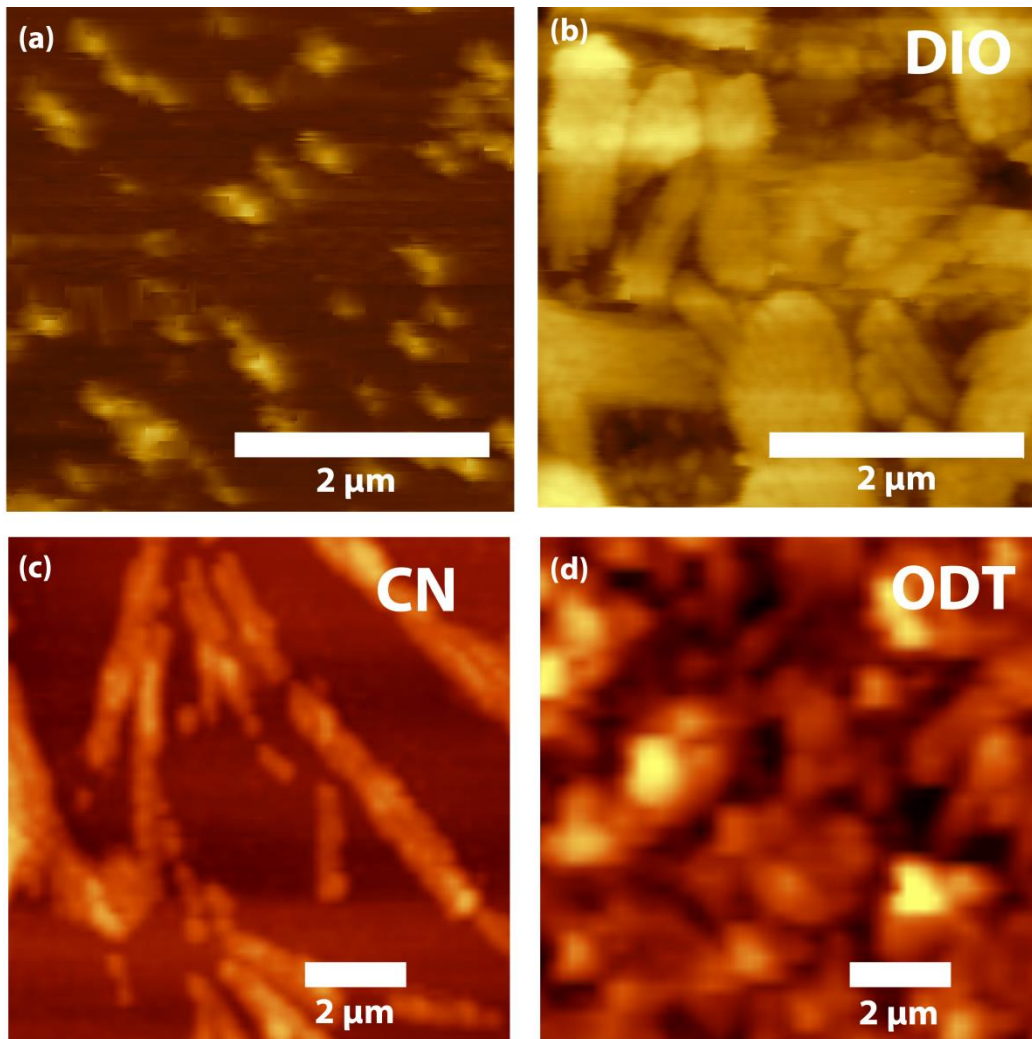


Figure S4.4. AFM tapping-mode height image. (a) Self-doped CsPbI₃ without any additive, (b) self-doped CsPbI₃ with DIO, (c) self-doped CsPbI₃ with CN, and (d) self-doped CsPbI₃ with ODT.

Annexes

CV

Name: Tamiru Kebede Shicho

Sex: Male Age: 37 Religious: Protestant

Educational background

Teaching Physics (12+2) Diploma in 2007 G.C (Hawasa TTC)

Bachelor of Education Degree in physics (12+4) in 2011 G.C (Jimma University)

MSC in LASER physics (LASER Spectroscopy) 2016 G.C(Dilla University)

Work Experience: 17 years (6 years at Saylem High School, 3 years MSC attending, 2 years as Lecturer at Mizan-Tepi University, 6 years as Lecturer at Bonga University)

Current responsibilities: Lecturer at Bonga University & PhD. Candidates at Jimma University

Publications :




Publication (1)

<https://doi.org/10.3390/mi14081601>



Article

Phase Behavior and Role of Organic Additives for Self-Doped CsPbI₃ Perovskite Semiconductor Thin Films

Tamiru Kebede ^{1,2}, Muluaem Abebe ¹, Dhakshnamoorthy Mani ¹, Jibin Keloth Paduvilan ³, Lishin Thottathi ⁴, Aparna Thankappan ⁵, Sabu Thomas ⁶, Sarfaraz Kamangar ⁷ , Abdul Saddique Shaik ⁷, Irfan Anjum Badruddin ⁷ , Fekadu Gochole Aga ^{8,9} and Jung Yong Kim ^{8,9,*} 

¹ Faculty of Materials Science and Engineering, Jimma Institute of Technology, Jimma University, Jimma P.O. Box 378, Ethiopia; tamiruks@gmail.com (T.K.); muluaem.mekonnen@ju.edu.et (M.A.); dhakshnamoorthy.mani@ju.edu.et (D.M.)

² Department of Physics, College of Natural and Computational Science, Bonga University, Bonga P.O. Box 334, Ethiopia

³ School of Chemical Sciences, Mahatma Gandhi University, Kottayam 686560, India; jibinkp999@gmail.com

⁴ Department of Physics and Mathematics, Università Cattolica del Sacro Cuore, Via della Garzetta, 48, 25133 Brescia, BS, Italy; lishint123@gmail.com

⁵ Department of Physics, Baselius College, Kottayam 686001, India; aparnathankappan@baselius.ac.in

⁶ School of Energy Materials, Mahatma Gandhi University, Kottayam 686560, India; sabuthomas@mgu.ac.in

⁷ Mechanical Engineering Department, College of Engineering, King Khalid University, Abha 61421, Saudi Arabia; sarfaraz.kamangar@gmail.com (S.K.); abdul.siddique1976@gmail.com (A.S.S.); magami.irfan@gmail.com (I.A.B.)

⁸ Department of Materials Science and Engineering, Adama Science and Technology University, Adama P.O. Box 1888, Ethiopia; fekadu.gochole@astu.edu.et

⁹ Center of Advanced Materials Science and Engineering, Adama Science and Technology University, Adama P.O. Box 1888, Ethiopia

* Correspondence: jungyong.kim@astu.edu.et




Citation: Kebede, T.; Abebe, M.;

Publication (2)

<https://doi.org/10.3390/electronicmat5020005>

Article

Silver-Doped CsPbI₂Br Perovskite Semiconductor Thin Films

Tamiru Kebede ^{1,2}, Muluaem Abebe ¹, Dhakshnamoorthy Mani ¹, Aparna Thankappan ³, Sabu Thomas ⁴ and Jung Yong Kim ^{5,6,*} 

¹ Faculty of Materials Science and Engineering, Jimma Institute of Technology, Jimma University, Jimma P.O. Box 378, Ethiopia; tamiruks@gmail.com (T.K.); muluaem.mekonnen@ju.edu.et (M.A.)

² Department of Physics, College of Natural and Computational Science, Bonga University, Bonga P.O. Box 334, Ethiopia

³ Department of Physics, Baselius College, Kottayam 686001, India; aparnathankappan@baselius.ac.in

⁴ School of Energy Materials, Mahatma Gandhi University, Kottayam 686560, India; sabuthomas@mgu.ac.in

⁵ Department of Materials Science and Engineering, Adama Science and Technology University, Adama P.O. Box 1888, Ethiopia

⁶ Center of Advanced Materials Science and Engineering, Adama Science and Technology University, Adama P.O. Box 1888, Ethiopia

* Correspondence: jungyong.kim@astu.edu.et

Presentations

1. 'Phase Behavior and Role of Organic Additives for Self-Doped CsPbI₃ Perovskite Semiconductor Thin Films' has made an International architectural sciences and applications symposium at Naples, Italy
2. 'The influence of organic additives on the morphology improvement of all inorganic perovskite' has made 3rd annual research at Bonga University .

